Hydrodynamics of bubble column reactors in floating conditions

Mémoire

Nasim Heydari

Maîtrise en génie chimique - avec mémoire
Maître ès sciences (M. Sc.)

Québec, Canada

Hydrodynamics of bubble column reactors in floating conditions

Mémoire

Nasim Heydari

Sous la direction de :

Faical Larachi, directeur de recherche
Seyed Mohammad Taghavi, codirecteur de recherche
François Bertrand, codirecteur de recherche

Résumé

Les réacteurs à colonne à bulles gaz-liquide ainsi que gaz-liquide-solide sont largement utilisés dans les raffineries de pétrole et les usines de traitement de gaz. Ils sont notamment utilisés dans les procédés chimiques mettant en jeu des réactions. Ces dernières années, l'industrie pétrolière et gazière offshore s'est de plus en plus intéressée à l'extension de l'application des réacteurs pour les plates-formes flottantes telles que les unités flottantes de stockage et de déchargement de production (FPSO). Cependant, les enjeux des courants marins et des vagues influencent les performances des réacteurs installés à bord des unités marines. Pour maintenir la capacité et les spécifications de produit dans de tels réacteurs, la prédiction de leurs écarts de performance par rapport à ceux statiques est essentielle. En particulier, l'étude du comportement d'un écoulement à bulle unique dans une colonne en mouvement fournira une base pour comprendre le comportement plus complexe d'un écoulement à bulles multiples dans un réacteur à colonne à bulles fonctionnant dans des conditions flottantes.

Afin de mieux comprendre les effets de la houle marine sur les performances des réacteurs à colonnes à bulles, cette recherche vise à étudier l'hydrodynamique de la remontée d'une seule bulle dans une colonne inclinée. Comme l'interaction bulle-paroi a un impact majeur sur l'hydrodynamique du réacteur à colonne à bulles dans des conditions flottantes, les modifications de la trajectoire de la bulle, de la vitesse et du rapport d'aspect imposées par les interactions bulle-paroi sont étudiées.

Abstract

Gas-liquid as well as gas-liquid-solid bubble column reactors are extensively used in oil refineries and gas treatment plants. They are used especially in chemical processes involving reactions. In recent years, offshore oil and gas industry has been increasingly interested in extending application of reactors for floating platforms such as floating production storage and offloading (FPSO) units. However, the challenges of marine currents and waves influence performance of reactors installed onboard marine units. To maintain the capacity and product specifications in such reactors, prediction of their performance deviations with respect to the static ones is essential. Particularly, investigation on single bubble flow behavior in a moving column will provide a basis to understand the more complex behavior in multi-bubble flow in a bubble column reactor operating in floating conditions.

To provide more detailed understanding into the effects of marine swells on the performance of bubble column reactors, this research aims at studying the hydrodynamics of single bubble rising in an inclined column. As the bubble-wall interaction has a major impact on the hydrodynamics of bubble column reactor under floating conditions, the modifications in bubble trajectory, velocity, and aspect ratio imposed by the bubble-wall interactions are studied.

This master thesis consists of two chapters. The first chapter contains a general introduction on the challenges brought by the need to extend the application of hydrocarbon treating facilities onboard marine units. Important information about hydrodynamics of bubble column reactors and single bubble rising in liquid are provided. Additionally, the most important issues in selection of the solver and the simulation methods are discussed. In the second chapter, the dynamics of a single ellipsoidal air bubble rising in an inclined cylindrical vessel is experimentally investigated. At the end, a general conclusion on the work performed and recommendations for future works is presented.

Contents

List of Tables

List of Figures

Acknowledgements

This research was supported by the Natural Sciences and Engineering research Council of Canada through Discovery Grants and a Grant from the Collaborative Research and Training Experience (CREATE-481695-2016) program in Simulation-based Engineering Science.

Forward

This master thesis including one article. The second chapter was published as a journal paper:

Nasim Heydari, Faical Larachi, Seyed Mohammad Taghavi, Francois Bertrand, Three-dimensional analysis of the rising dynamics of individual ellipsoidal bubbles in an inclined column, Chemical Engineering Science, v258 (20220831), 2022.

Authorship contribution is as follows:

Nasim Heydari: Conceptualization, Methodology, Formal analysis, Investigation, Writing, Visualization, Code Development. Faïçal Larachi: Supervision, Funding acquisition, Project administration. Seyed Mohammad Taghavi: Supervision. François Bertrand: Supervision, Funding acquisition.

The revisions have been made in the submitted manuscript to be published are:

1- A section added for describing experimental uncertainty

2- The result and discussion section was revised to improve the clarity of the discussion

3- Conclusion was revised to be structured to focus on the results and to discuss and evaluate them in more detail.

Introduction

After the emergence of fixed offshore platforms, recently, there is an increasing interest in developing floating platforms as possible solutions for economic development of remote offshore resources [1, 2]. Two types of floating platforms that are designed for hydrocarbon treating and refinement in the location of extraction are floating production storage and offloading (FPSO), and floating liquefied natural gas (FLNG). Process equipment for oil and gas treatment such as separators, distillation columns, and reactors are installed onboard of these floating units [2]. Hence, the need for transportation of the hydrocarbon to onshore refineries is diminished and the treated hydrocarbon is traded directly from the ship [3]. A sketch of integration of different extraction, production, storage and treating facilities on FPSO units, is shown in Figure a.

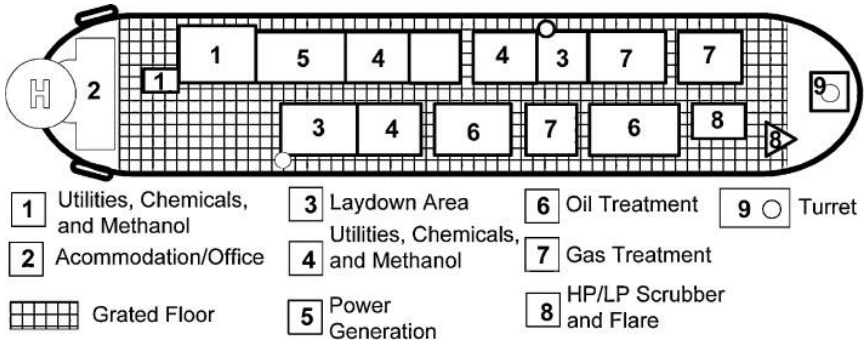

Figure a. A sketch of floating production storage and offloading unit [3]

The technical challenges stemming from motion inherent in barge operation, cause performance deviations in process and storage facilities installed on mobile platforms [1]. Figure b shows the different motions that may be imposed by sea swells on a floating vessel [3]. Six degrees of freedom of motions including translational (surge, sway, and heave) and rotational (roll, pitch, and yaw) motions are shown schematically.

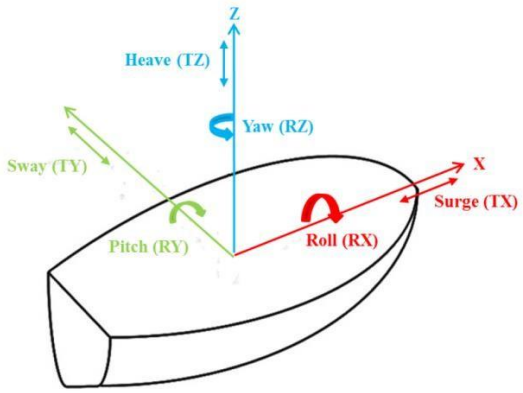

Figure b. Six degrees of freedom motions of a floating vessel [3]

Recently, there is a great interest in predicting the effect of different environmental conditions on the performance of onboard facilities and solving the resulting fluid maldistribution [3]. One of the recent advances was the design of a distributor tray for efficient contact of gas and liquid in distillation columns or dehydration units developed by Institut Francais du Petrole (IFP). It was designed to increase liquid circulation within perforations during rolling conditions [4]. Also, Sulzer Company designed a cross- corrugated packing to achieve an even wetting in the packing and reducing the phase maldistribution in the moving columns [5].

Bubble column reactors as multiphase reactors have a wide application in chemical, petrochemical, biochemical and metallurgical industries. Their popularity is especially due to lack of moving parts, and consequently little maintenance, and low operating costs [6]. They are widely used in various processes such as hydrogenation, hydrotreating, Fischer–Tropsch synthesis, wastewater treatment [7], and are perceived to be particularly useful in fuel processing and gas treatment applications in FPSO units [7]. However, as pointed above, ship motions caused by sea swells may have significant impacts on their performance, working capacity and product specifications.

This review aims to discuss flow fundamentals in bubble column reactors installed onboard floating units and to address the present industrial and academic developments in oil and gas offshore processing. Despite the intensive theoretical research performed on the description of flow structure in bubble columns, the impact of marine currents and waves on reactor performance is not investigated.

1. Chapter 1: Background

1.1. Abstract

This chapter is structured as follows: first, general information and important parameters effective in design and performance of bubble column reactors are briefly reviewed. As the rise of single air bubble in liquid is an important fundamental phenomenon that contributes significantly to the hydrodynamics in gas−liquid reactors, the most important aspects in single bubble rising hydrodynamics are discussed in Section 1.3. Section 1.4 reviews previous studies on bubble rising characteristics in different static and dynamic geometries. The Section 1.5 reviews the simulation methods of bubble column reactors.

1.2. Bubble column reactors

Bubble column reactors are in the category of multiphase reactors, in which the gas phase is dispersed into a liquid phase [8]. A simple bubble column consists of a vertical cylinder in which the gas enters at the bottom of the column through a gas sparger and the liquid phase may be supplied in either batch mode or flows co-currently or counter-currently to the gas stream [9]. Despite the simple configuration, their correct design needs precise knowledge of fluid dynamic phenomena on different scales.

Single bubble characteristics and gas-liquid interfacial dynamics at the microscale influence the more complex mesoscale hydrodynamics involving bubble-bubble interactions and bubble swarm dynamics. The mesoscale hydrodynamics also determines the flow structure and flow regime at the macroscale or reactor scale [10]. Flow pattern, mean residence time of the dispersed phase and liquid recirculation are mainly studied at the macroscale.

Gas flow rate is the main parameter in characterizing flow regime and hydrodynamics of bubble column reactors [11]. Based on superficial gas velocity, flow regimes in bubble columns are categorized into two homogenous and heterogeneous regimes. The homogenous regime which is known as the bubbly flow regime can be recognized in the range of superficial gas velocities less than 5 m/s [12]. In a homogenous bubbly flow regime, bubbles are roughly in uniform size while in the heterogeneous regime, small and large bubbles coexist [13].

Another important design parameter in bubble columns is the gas holdup, which is related to bubble size distribution and depends on the gas and liquid velocities, reactor operating conditions, dimensions of the column, and liquid phase properties [11]. The overall mass transfer

rate in a bubble column, which is the product of liquid-side mass transfer coefficient and interfacial area, is dependent on the gas holdup [11].

1.3. Single bubble hydrodynamics

To elucidate fundamental parameters that affect the behavior of gas-liquid two-phase flow such as gas holdup, gas residence time and gas-liquid interface transferring properties, a clear understanding of bubble rising hydrodynamics is essential [14]. Hence, in following, different parameters involved in bubble rising dynamics, in terms of drag force, rise velocity, lift force, bubble shape, trajectory, aspect ratio and the forces act on bubble are discussed.

1.3.1. Drag force

Physics of flow around a bubble differs in three ways from that around a solid particle. First, due to very low density of bubbles compared to that of the liquid, the inertia-induced hydrodynamic forces are very important in predicting the bubble motion. Second, bubble deformation is possible due to local hydrodynamic forces [15, 16]. Third, in contrast to the flow past rigid bodies, when the liquid is pure enough it slips along the surface of the bubble [15].

The zero-shear-stress boundary condition imposed on the bubble surface has two important consequences:

1- As the liquid can slip along the bubble surface, flow is unseparated in conditions where flow around a solid body would be separated.

2- It affects the vorticity production on the bubble surface and its evolution with Reynolds number.

Drag coefficient of a spherical or nearly spherical bubble is much smaller than drag coefficient of a solid sphere with the same diameter due to the difference in the boundary condition [15].

Theoretical works on the motion of particles in fluid continua derived analytically the well-known Stokes law:

$$C_D = \frac{24}{Re} \tag{1.1}$$

Which is valid at low Reynolds numbers [15, 17].

Levich [18] first obtained the drag coefficient for a spherical bubble in a uniform flow at high

Reynolds number, via a dissipation method assuming that the flow does not separate on a clean spherical bubble:

$$C_D = \frac{48}{Re} \tag{1.2}$$

This was also achieved later by direct integration of the normal stresses over the bubble surface by Kang and Leal [19].

Moore [20] calculated the drag coefficient by integrating an approximation to the normal stresses over the bubble surface. He included the normal viscous stresses and the inviscid pressure field obtained via Bernoulli's theorem:

$$C_D = \frac{32}{Re} \tag{1.3}$$

It was suggested by Batchelor, that the discrepancy between equations (1.2) and (1.3) was due to the neglect of pressure forces in the boundary layer by Moore [21]. Later it was shown by Kang and Leal that one third of the total drag in equation 1.2 corresponds to the pressure variation over the bubble surface [19].

Moore [21] corrected the Levich's equation accounting for the existence of a thin boundary layer and a narrow wake around bubble. The effect of vorticity in the boundary layer is to reduce the local strain rate by reducing the tangential velocity.

$$C_D = \frac{48}{Re}\left(1 - \frac{2.21}{Re^{1/2}}\right) + O(Re^{-\frac{5}{6}}) \tag{1.4}$$

Using the same method, Moore [22] evaluated the motion of deformed bubbles and obtained the following equation for the drag coefficient:

$$C_D = \frac{48}{Re}\, G(x) \tag{1.5}$$

$$G(x) = \frac{1}{3}\, x^{4/3}(x^2 - 1)\frac{(x^2-1)^{1/2} - (2-x^2)sec^{-1}x}{x^2 sec^{-1}x - (x^2-1)^{1/2}} \tag{1.6}$$

In this equation, bubble deformation, *x*, is defined as the ratio of the major axis to the minor axis of the sectional ellipse.

Duinveld et al. [23] performed a complete study on Moore's equation for ellipsoidal bubbles with aspect ratios ranging from 1.0 to 2.0 and Reynolds numbers varying from 90 to 700. Good agreement was observed with Moore's drag equation, for bubble radius less than 0.6 mm and

$Re = 360$. However, for larger Re, measured rise velocities were larger than predictions by Moore (1965) because theoretical analysis over predicts the bubble aspect ratio since it implies fore-aft symmetric shapes. Despite the satisfactory predictions of drag coefficient by equations (1.4) and (1.5), small amounts of impurity are sufficient for large deviations comparing experimental observations. Maxworthy et al. [24] reported higher drag coefficient by nearly 30% than those predicted by Moore's equation for ellipsoidal bubbles rising in a mixture of glycerin and distilled water over the Reynolds numbers ranging from 100 to 200, because of the liquid contamination.

The drag coefficient for a bubble rising in still liquid can be obtained from a steady-state force balance in vertical direction [25]. When bubble rises in a rectilinear path, after a short initial acceleration, the velocity becomes steady. So, the drag coefficient can be determined by equating buoyancy with drag.

$$0 = \rho_c V \mathrm{g} - C_D A \frac{\rho_c}{2} v_\infty^2 \tag{1.7}$$

$$C_D = \frac{4 g d_e}{3 v_\infty^2} \tag{1.8}$$

If bubble rises in a helical path, velocity of the bubble is in e_θ, e_z plane (Figure 1.1). Drag force is in the same plane but in the opposite direction of velocity. So, the drag coefficient in z-direction is:

$$C_{D_z} = \frac{4 g d_e}{3 {v_z}^2} \tag{1.9}$$

However, the magnitude of the force in e_θ, e_z plane is different because of the slope of helix trajectory (φ).

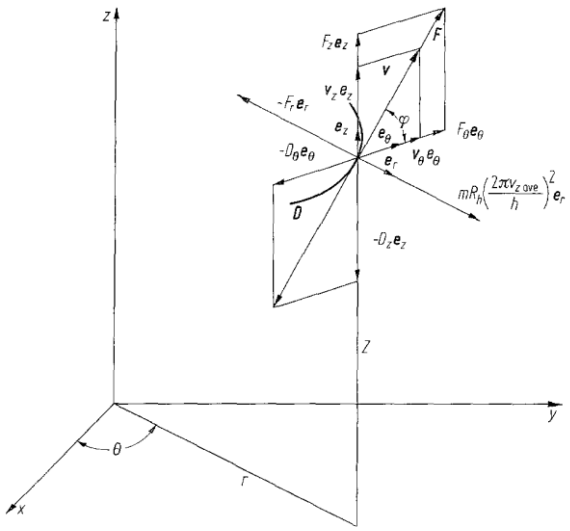

Figure 1.1. Forces acting on a bubble rising in helical path [17]

The coefficient of the total drags in the e_θ, e_z plane is:

$$C_D = \frac{4gd_e}{3{v_z}^2}\sin\varphi = C_{D_z} sin\varphi \tag{1.10}$$

As far as the bubble moves in a rectilinear path, no boundary layer separation occurs on its surface. Therefore, drag is mainly the friction drag. Separation of the boundary layer for a bubble which rises in a non-rectilinear path results in formation of the form drag. This increases the total drag acting on the bubble.

Variation of drag coefficient with Reynolds and Weber numbers has been the subject of many experimental works. Drag coefficient diagrams have a minimum, then increase with Reynolds number, due to bubble deformations and finally become greater than the drag of rigid spheres of the same size (Figure 1.2) [17].

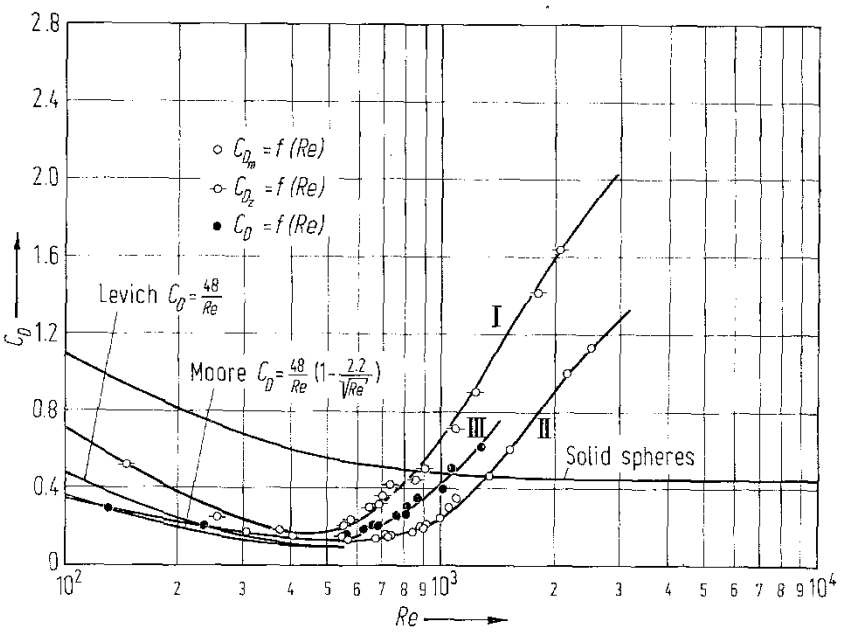

Figure 1.2. Variation of drag coefficient with *Re* number [17]

The sharp minimum present in drag coefficient curves (Figure 1.3) of liquids with low Morton numbers is known as the cause of the maximum point presents in velocity-diameter plots. There is a critical region in which drag coefficient increases rapidly, bubble surface ceases to be steady and the bubble trajectory deviates from rectilinear. Hartunian & Sears (1957) [26] suggested that the bubble surface instability is responsible for the effects [22].

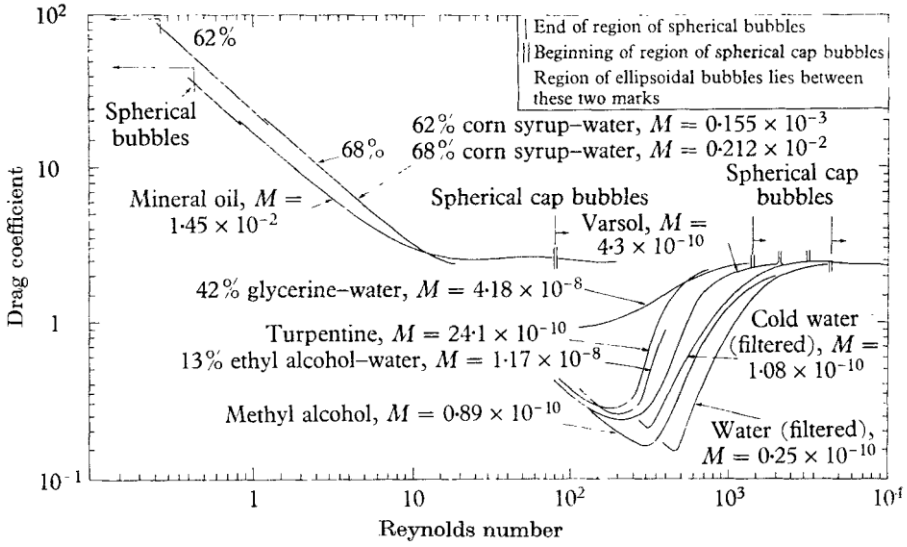

Figure 1.3. C_D vs. *Re* for different liquids Haberman & Morton (1953) [27]

Dijkhuizen et al. [25] obtained the instantaneous drag coefficient and aspect ratio for a 6 mm air bubble while rising in water using Front Tracking simulation (Figure 1.4). After the bubble gets its approximate shape and drag, it starts wobbling, then, it reaches its steady state motion. The gradual decrease of drag coefficient and increase of aspect ratio are the results of gradual volume defect of the bubble.

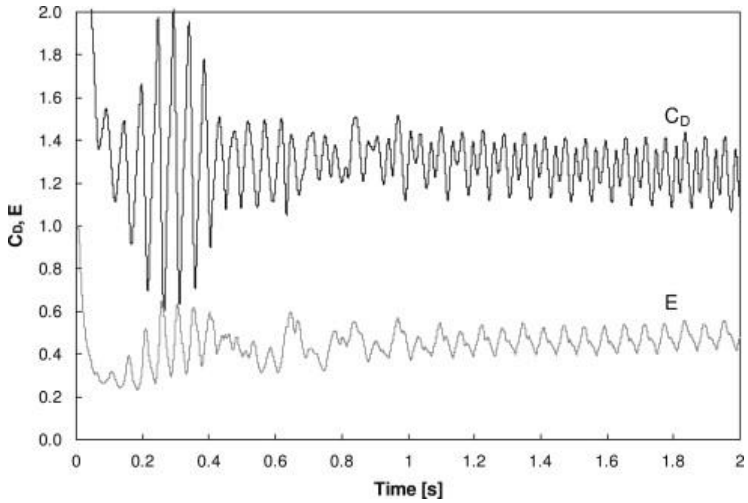

Figure 1.4. Drag coefficient and bubble aspect ratio for a 6 mm air bubble in water [25]

1.3.2. Velocity

Experimental works mainly aimed at measuring bubble terminal velocity and its variation with the equivalent bubble diameter. Profiles of the instantaneous bubble velocities during rising are shown in Figure 1.5, for two bubble diameters, i.e., 2.01 mm and 7.33 mm.

When bubble detaches from nozzle, the instantaneous velocity increases quickly, then, approaches the terminal velocity and remains constant. However, for bubbles with equivalent diameter less than 3mm, the instantaneous velocity achieves stability without experiencing a maximum value [14, 27].

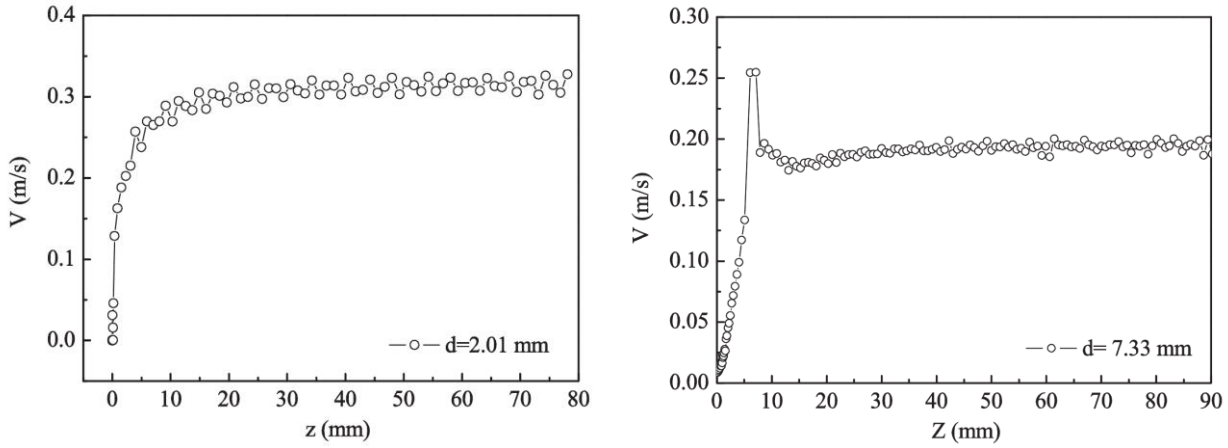

Figure 1.5. Instantaneous bubble rising velocity [14]

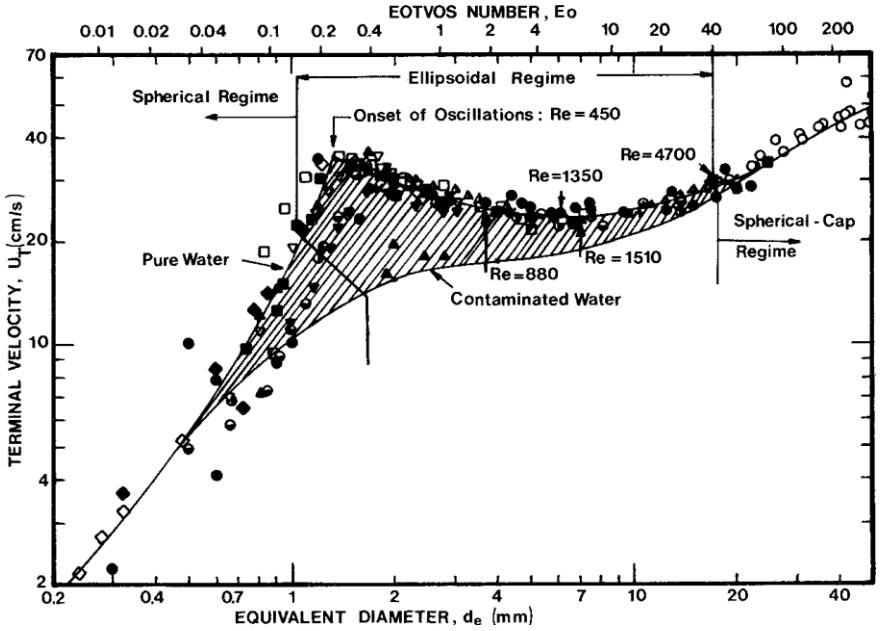

Figure 1.6. Terminal velocity versus equivalent bubble diameter [29]

As mentioned above, the minimum in the drag coefficient curves shown in Figure 1.3 is responsible for the maximum in the velocity-diameter diagram, in which, the trajectory becomes helical or sinusoidal, and the terminal velocity decreases with bubble diameter due to the added drag for the unsteady motion [28].

Extensive research has been conducted to establish a reliable model for bubble terminal velocity. Theoretical models are only available for two cases, i.e., small spherical bubbles and large

spherical-cap bubbles. When a bubble is small enough to be spherical and the bubble Reynolds number is less than unity, terminal velocity can be evaluated using the Hadamard–Rybczynski [29] equation:

$$v_\infty = \frac{2}{3}\frac{r^2 g(\rho_l - \rho_g)}{\mu_l}\frac{\mu_l + \mu_g}{2\mu_l + 3\mu_g} \tag{1.11}$$

However, if surfactants are accumulated on bubble surface, the interface becomes immobile due to the so-called Marangoni effects, and the bubble behaves as a rigid sphere. In this case, the Stokes drag model can be used for the evaluation of terminal velocity. For a bubble of intermediate size, no theoretical model for terminal velocity have been proposed.

Three regimes can be identified in the plot of bubble velocities versus diameter: spherical, ellipsoidal and spherical-cap (Figure 1.6). Air bubbles that rise in water with the sphere-volume equivalent diameter ranging from 1.3 to about 6 mm are in surface tension force dominant regime, in which terminal velocity gradually decreases with increasing diameter. In the surface tension dominant regime, which is shown in the shaded area in Figure 1.6, the bubble rise velocity is not only a function of the bubble diameter. Many researchers have pointed out different terminal velocities for bubbles with similar diameters [30].

Different terminal velocities have been attributed to different surfactant concentrations in liquid phase. When a bubble moves through the liquid phase, surfactants accumulate at the interface. The liquid then tends to sweep the adsorbed surfactant to the rear of the bubble. The concentration gradient of surfactant gives rise to a tangential force in the opposite direction of the flow. The interface acts like a solid body surface, which decreases the internal circulation and thereby increases the drag on the fluid particle. Additionally, more vorticity is generated on the immobilized surface comparing a clean interface, which promotes separation around the fluid particle and increases the wakes behind. Hence, the form drag increases. In contrast, Aybers and Tapucu [17] measured rising velocities of single air bubbles in stagnant water and concluded that the effect of surfactants on the rising velocity is very small for bubbles larger than 1.3 mm. The authors suggested that the bubble shape oscillation has an important effect on the rising velocity. Zhang and Finch [31] found out that terminal velocity is independent of surfactant concentration for bubbles with diameters of 0.8 and 1.4 mm bubbles.

Tomiyama et al. [30] showed that the primal cause of widely scattered terminal velocities in

surface tension dominant regime is the initial shape deformation of the bubble after release from nozzle. When a bubble releases with large initial shape deformation, it's shape is stretched, and the bubble starts its motion with a surface free energy larger than that of a bubble with small initial shape deformation. Hence, when a bubble releases from a nozzle with large initial shape deformation, axial velocity is high [27, 30], the motion is helical, and the aspect ratio is low. In contrast, when initial shape deformation is small the rising velocity is low, the motion is zigzag, and the aspect ratio keeps a high value. Therefore, even in the pure water, terminal velocity widely scattered in the surface tension force dominant regime as shown in Figure 1.6. For air bubbles rising in contaminated water, the rise velocity is independent of the initial perturbations, which is attributed to the rapid damping of perturbations in the presence of contaminants.

Tomiyama et al. [30] proposed a correlation for bubble rising velocity as a function of bubble aspect ratio:

$$v_\infty = \frac{sin^{-1}\sqrt{1-E^2}-E\sqrt{1-E^2}}{1-E^2}\sqrt{\frac{8\sigma}{\rho_l d}E^{4/3}+\frac{\Delta\rho g d}{2\rho_l}\frac{E^{2/3}}{1-E^2}} \tag{1.12}$$

Parameters that need to be considered during measurement of bubble terminal velocity, are the liquid pollution degree, bubble size and shape, injection method, rising path, and fluid physical properties [27]. Celata et al. [32] used two methods for bubble injection, controlled and direct method. In the direct injection method, bubble diameter is greater than nozzle diameter in the controlled method, nozzle diameter is larger than bubble diameter.

1.3.3. Lift force

There are several causes for lateral lift forces acting on bubbles, i.e. wake phenomenon, shear of the fluid, fluid particle deformation and presence of surfactants in the continuous phase.

Wake Phenomenon: during vortex shedding, liquid moves towards the space behind the body more slowly than the rotational velocity of the vortex [33]. Hence, the velocity significantly reduces in this region. According to the Bernoulli equation, this decrease in the velocity of fluid generates an increase in pressure, thus a transient lateral force on the body [34].

Shear of the fluid: a lateral force can be induced by shear in the continuous phase, which generates vorticity at the rear of the bubble. The lift force which governs the direction of

transverse migration of a bubble in a shear field, depends on bubble size. In co-current pipe flow, small bubbles ($1mm < d < 5mm$) tend to migrate toward the pipe wall, whereas large bubbles ($d > 5mm$) tend to migrate toward the pipe center [15, 34].

The lift force, acting on a sphere moving steadily in a weak shear is:

$$\vec{F}_L = \rho C_L V(\vec{v} - \vec{v}_p) \times \vec{\omega} \tag{1.13}$$

Where $\vec{\omega} = \nabla \times \vec{v}$ is the vorticity upstream of the body and $\vec{v}$ is the fluid velocity [15].

This quasi-steady force is of lower magnitude than the instantaneous lift force, which is dominated by the inherent vortex shedding of the bubble wake [14].

Deformation: deformed bubbles migrate in the direction opposite to that followed by spherical bubbles. They act like an airfoil-shaped object and experience a lateral force towards the lower velocity side [34].

Surfactants: surfactants accumulate on bubble surface and cause interfacial shear stresses, thus increase the drag force. Additionally, the increased amount of vorticity influences the lift force. [34].

1.3.4. Bubble shape

Variations of hydrostatic and dynamic pressure over the bubble surface increase with bubble rise velocity and size [15]. Hence, large bubbles deform into oblate spheroids [15, 22]. Lindt [35] introduced a well-defined classification on bubble shape and trajectory based on equivalent bubble radius and Reynolds number (Table 1.1). Shapes of bubbles while rising freely in liquid media under the influence of gravity can be spherical, ellipsoidal and spherical-cap or ellipsoidal-cap [35, 36]. Bubbles with small diameters (<1.3 mm) remain spherical and rise in a rectilinear path. As the bubble diameter increases, it deforms to ellipsoidal, oblate ellipsoidal, or cap shape, with interface wobbling, and rises in a zigzagging or helical motion [17].

Table 1.1. Classification of bubble shape & trajectory based on equivalent radius/Reynolds number [37]

class	equivalent radius	Reynolds number	description
1	$r_e < 0.04$ cm	Re < 70	spherical bubbles, rectilinear path, C_D as for rigid spheres
2	$0.04 < r_e < 0.062$ cm	70 < Re < 400	sphere, rectilinear path, C_D less than solid spheres
3	$0.062 < r_e < 0.077$ cm	400 < Re < 500	oblate spheroid, rectilinear motion
4	$0.077 < r_e < 0.24$ cm	500 < Re < 1100	oblate spheroid, helical motion
5	$0.24 < r_e < 0.35$ cm	1100 < Re < 1600	irregular oblate spheroid, almost rectilinear motion
6	$0.35 < r_e < 0.88$ cm	1600 < Re < 5000	transition from oblate spheroid to spherical cap, almost rectilinear motion
7	$r_e > 0.88$ cm	Re > 5000	spherical cap, rectilinear motion

Bubble rising characteristics in terms of bubble shape, trajectory, and rising velocity can be well defined by the Reynolds, Eötvös, and Morton numbers, which are defined as:

$$Eo = \frac{g\Delta\rho d_e^2}{\sigma} \tag{1.14}$$

$$Mo = \frac{g\Delta\rho\mu_l^4}{\sigma^3\rho_l^2} \tag{1.15}$$

$$Re = \frac{\rho_l d_e v}{\mu_l} \tag{1.16}$$

$$We = \frac{\rho_l d_e v^2}{\sigma} \tag{1.17}$$

Where $\Delta\rho$ is density difference between the gas and liquid phases [36, 37]. Liquid properties are defined by Morton number, while Weber number describes the bubble deformation, and Reynolds number is based on the bubble diameter and its rising velocity [38].

Clift et al. [36] reported a generalized plot, shown in figure 1.7, for various bubble shape categories and different Reynolds and Eötvös numbers. Bubbles are approximately spherical if interfacial tension and viscous forces are much more dominant than the inertia forces [36]. It is well known that in low Eötvös numbers (< 0.25), bubbles are spherical due to high surface tension forces. This spherical shape prevails up to the Reynolds numbers around 500. In higher Eötvös number (0.25 - 0.4), deformation occurs and ellipsoidal shape bubbles form [39]. In the

case of water, the bubble shape is mainly dominated by inertial forces and surface tension, while the effect of viscosity is negligible. However, in a glycerol aqueous solution (63-622 mPa.s), the viscous force is the dominant force [27].

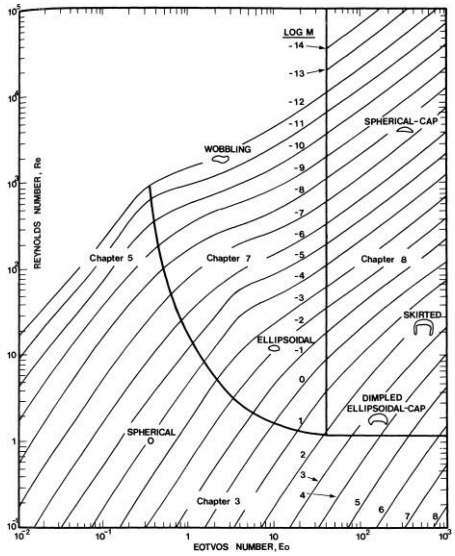

Figure 1.7. Regime map for various bubble shapes: Effect of bubble shape on bubble rising trajectory and velocity (After Clift et al.) [29]

Several researchers have analyzed regions of different bubble shapes in the Eötvös-Reynolds number plot, by numerical modeling and CFD simulations. Using the Gerris solver, Thripati et al. [40] studied on bubble rising dynamics with different diameters and developed a plot in the Galileo-Eötvös plane showing various regions of bubble shape with sharply defined boundaries.

Shape oscillation is mainly known as the effect of path instability rather than being the cause [41, 42]. This has also been supported by Direct Numerical Simulation performed by Mougin et al. [43], who have studied the zigzagging trajectory of a fixed shape ellipsoidal bubble [41, 43].

1.3.5. Rising trajectory and wake

It is well known that no boundary layer separation occurs and consequently no wake forms in the spherical regime of bubbles. The slip boundary condition around bubbles forms low surface vorticity in comparison with the solid object movement in liquid. However, for systems with high Eötvös numbers (> 0.25) flow separation forms eddies and wake while the flow is passing through the ellipsoidal bubbles [37]. Several studies have been performed to clarify the wake

structure and its' effects on the other hydrodynamic characteristics of the bubble [32, 44, 45]. Veldhuis et al. [46] and de Veris et al. [47] developed experimental investigations on the generated wake behind rising and falling spheres. They captured wake details at high Reynolds numbers using Schlieren optics technique. It was illustrated that the wake structure has two threads and the two threads come together while the bubble is crossing the center of the zigzag trajectory.

Mougin & Magnaudet [48] reported that the rectilinear path changes to the zigzag path when two counter-rotating trailing vortices appear behind the bubble. They showed that the primary cause of path instability is wake instability and reject other possible causes, such as shape oscillations or contamination by surfactants. The vorticity at the bubble surface (which causes fore-and-aft asymmetry of the bubble) and the standing eddies at the rear of the ellipsoidal-shape bubbles give rise to bubbles' nonlinear trajectory [41].

Cano-Lozano et al. [49] used Gerris solver to analyze the bubble rising path transition from straight to zigzag in a stagnant liquid. The authors developed a Galileo-Bond number plot (Figure 1.8) to show the onset of standing eddy formation behind the bubble.

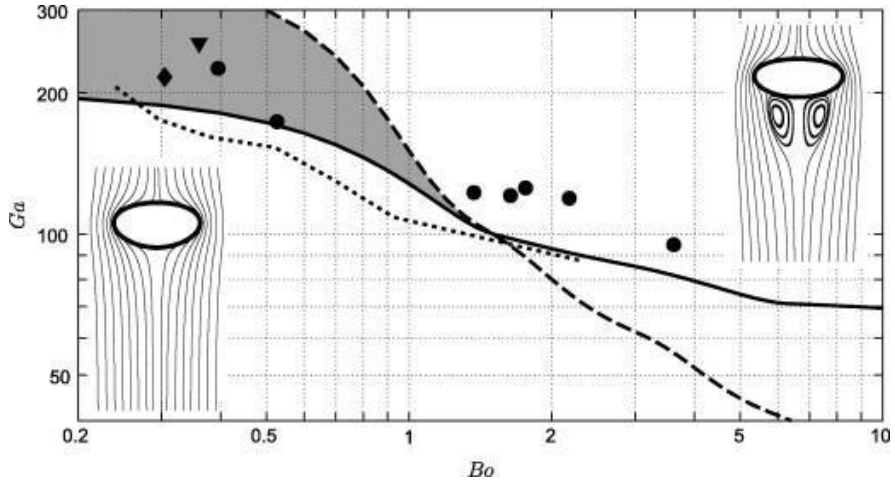

Figure 1.8. Continuous line: transition curve for the onset to zigzagging motion; Dashed line: transition curve for the presence of standing eddy [49]

An extensive number of experimental studies on the bubble rising path in different liquids have been performed [50]. Aybers et al. [17] investigated trajectories of air bubbles while rising in still water and observed five types of bubbles' motion that are listed in Table 1.2.

Table 1.2. Classification of bubble trajectory based on equivalent diameter/Reynolds number [17]

Equivalent diameter	Reynolds number	Path
$d_e < 1.3$ mm	$Re < 565$	Rectilinear
$1.3 < d_e < 2$ mm	$565 < Re < 880$	Helical
$2 < d_e < 3.6$ mm	$880 < Re < 1350$	Plane then helical
$3.6 < d_e < 4.2$ mm	$1350 < Re < 1510$	Plane
$4.2 < d_e < 17$ mm	$1510 < Re < 4700$	Rectilinear with rocking motion

Different types of bubble motion mainly depend on the bubble diameter. However, they also depend on other mechanisms, i.e. the presence of contaminants in liquid phase, coupling between the path and shape oscillations, initial conditions of bubble release and the presence of perturbations [30, 51]. Small initial shape deformation delays the transition from the primary to secondary unstable mode, i.e. from zigzag to helical motion. However, large initial shape deformation increases the growth rate of the secondary unstable mode [51]. Thus it was suggested by Tomiyama et al. [30] that the motion regime proposed by Aybers and Tapucu [17], shown in Table 1.2, is mainly the outcome of the bubble injection method they followed.

Mikaelian et al. [52], analyzed the dynamics of a single ellipsoidal bubble rising freely in water-glycerol mixture. The Eötvös number was in the range of 0.8-8, and Morton number was between 10^{-11} and 10^{-7}. The morphology of a single bubble rising trajectory in terms of frequencies and amplitudes of zigzag and helical motions was captured using two cameras. The authors proposed new correlations for scaled amplitude and frequency of the helical path. In the study of single bubble rising behavior in Newtonian and non-Newtonian fluids, Xu et al. [38] evaluated the effects of liquid properties, i.e. surface tension and viscosity on bubble rising dynamics in terms of rising trajectory, velocity, shape deformation, and equivalent bubble diameter. The authors analyzed the rising path transition from rectilinear to other forms, i.e., zigzag or spiral. Brucker et al. [42] performed experiments for Reynolds numbers between 1000 and 1500 and observed that an air bubble rises in a zigzag path at Reynolds numbers around 1320. During each period of zigzag movement two counter-rotating vortex form, diminish and become reversed in direction twice. Unlike the vortex shedding occurrence during a zigzag

motion, during a spiral movement, vortices remain attached asymmetrically at the rear of the bubble.

1.3.6. Aspect ratio

The bubble shape can be characterized using bubble aspect ratio, defined as:

$$E = \frac{d_v}{d_h} \tag{1.18}$$

After bubble release from nozzle, vertical velocity of bubble begins to rise rapidly while the aspect ratio decreases (Figure 1.9).

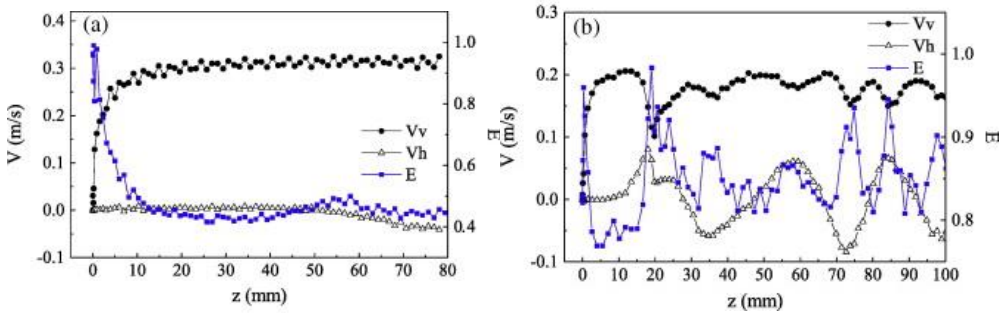

Figure 1.9. Bubble vertical velocity, horizontal velocity, and aspect ratio as a function of distance above the nozzle (a) bubble rises with rectilinear path (b) bubble rises with zigzag path [28]

For the bubble that follows a rectilinear path, the vertical velocity reaches terminal velocity, and the aspect ratio reduces, then both maintain a relatively stable state, in which the oscillation amplitude is very small. For a bubble that rises through a zigzagging path, the bubble vertical velocity rises rapidly, and horizontal velocity remains zero while the aspect ratio decreases. A periodic oscillation appears in vertical velocity, horizontal velocity, and aspect ratio. Within every oscillation, when the vertical velocity rises, the aspect ratio and horizontal velocity decrease. The oscillation frequency of vertical velocity is double the aspect ratio and transverse velocity [27].

Tomiyama et al. [30] showed that bubble terminal velocity depends on the aspect ratio as well as the bubble diameter, both experimentally and theoretically. The model (equation 1.13) proposed by the authors well predicted the effect of bubble size and aspect ratio on terminal velocity.

In the viscous force dominant regime (where $d < 0.83$ mm and the bubble trajectory is

rectilinear) bubble terminal velocity increases while aspect ratio decreases almost linearly with bubble diameter. In the surface tension force dominant regime (where $0.83 < d < 6$ mm) both terminal velocity and aspect ratio begin to scatter. For bubbles with helical trajectories, the terminal velocity is higher while aspect ratio is lower compared to bubbles with zigzag trajectories in this regime. This indicates that a bubble with a low aspect ratio is more likely to result in a high terminal velocity and a helical rising path. In the inertial force dominant regime (where $d > 6$ mm), terminal velocity increases and aspect ratio decrease gradually while both are less scattered.

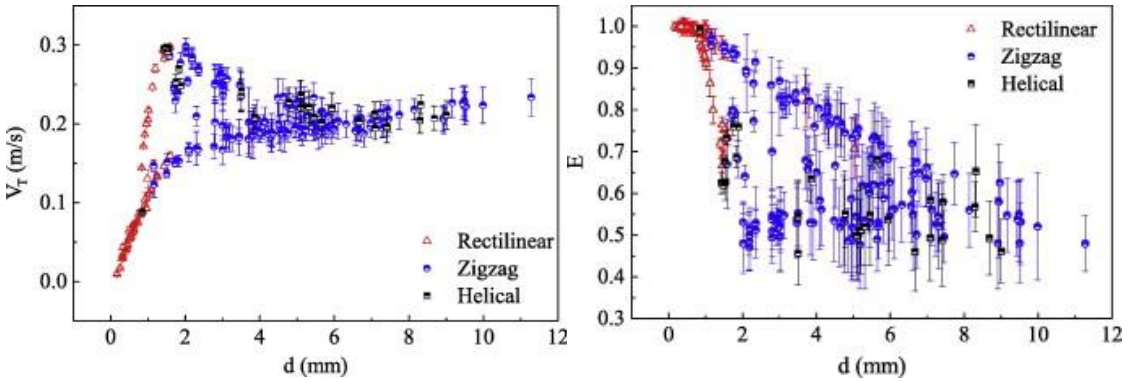

Figure 1.10. (Left) bubble terminal velocity versus bubble diameter in water (Right) bubble aspect ratio versus bubble diameter in water [28]

Using numerical simulations, Dijkhuizen et al. [25] showed that bubbles become more deformed at smaller bubble diameters when viscosity of the liquid phase decreases (going from liquids I to VIII in Figure 1.11).

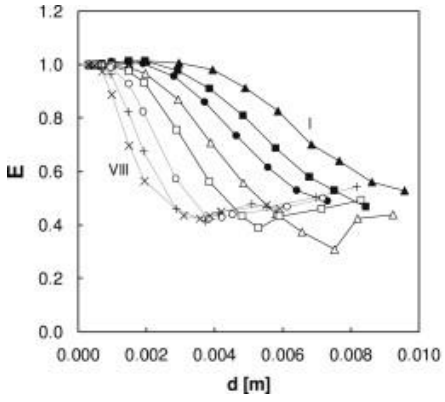

Figure 1.11. Aspect ratio versus bubble diameter [25]

Many correlations have been proposed for the aspect ratio defined as a function of dimensionless numbers. Wellek et al. [53] proposed a correlation for non-oscillating fluid particles in contaminated liquids (not ultra-purified liquids):

$$E = \frac{1}{1+0.163Eo^{0.757}} \tag{1.19}$$

When bubble diameter is large, the effect of inertial force on bubble shape must be considered. Eötvös number represents the ratio of gravity and surface tension, without relating to the influence of inertia force, therefore Eötvös number is not the appropriate parameter to group bubble shape data. For water with low viscosity, Weber number is more suitable to correlate the bubble shape than Eötvös number [27].

Using Weber number, Moore [22] derived the following equation assuming that the flow around the bubble surface is non-viscous:

$$We = 4E^{1/3}\frac{1+E^2-2E^3\left[cos^{-1}E-E\sqrt{1-E^2}\right]^2}{(1-E^2)^3} \tag{1.20}$$

This equation is valid for $E > 0.5$ [27].

1.3.7. Added mass force

When a body moves unsteadily in a uniform flow, it accelerates a part of the surrounding liquid which rises an added-mass force. The added mass depends on the orientation of the body relative to the flow:

$$\vec{F}_A = -\rho C_m V \frac{d\vec{v}_p}{dt} \tag{1.21}$$

When the fluid moves with a uniform and time-dependent velocity, the added-mass force is:

$$\vec{F}_A = \rho C_m V \frac{d(\vec{v}_l - \vec{v}_p)}{dt} \tag{1.22}$$

As the fluid is accelerated, it experiences an inertial force, in addition to the added mass force:

$$\vec{F} = \rho V \frac{d\vec{v}_l}{dt} + \rho C_m V \frac{d(\vec{v}_l - \vec{v}_p)}{dt} \tag{1.23}$$

Added-mass coefficient increases as bubble becomes oblate because it can accelerate a larger volume of fluid.

Aybers and Tapucu showed that the minor axis of the bubble is directed along the rising path.

When an ellipsoid bubble rises in a spiraling or zigzagging motion experiences a torque $\vec{\Gamma} = \rho V \vec{v}_p \times (C_m . \vec{v}_p)$ that acts to align the minor axis with the direction of rise [15].

1.3.8. History force

When the relative velocity between particle and the surrounding fluid varies, it produces vorticity that requires a finite time to diffuse into the flow. This gives rise to the so-called history force (Basset force). The nature of the history force and the steady drag are similar as both originate in a viscous flow [54].

1.3.9. Force measurements on rising bubbles

Interphase momentum transfer terms in two-phase flow are the drag, lift, virtual mass and other forces like the Basset force. This latter neglected in most practical calculations. In most two-fluid calculations the following force formulations are used:

$$\vec{F}_D = \frac{1}{2}\rho A C_D |\vec{v}_r| \vec{v}_r \tag{1.24}$$

$$\vec{F}_L = \rho V C_L \vec{v}_r \times (\nabla \times \vec{v}_l) \tag{1.25}$$

$$\vec{F}_A = \rho V C_m (\frac{\mathrm{D}\vec{v}_l}{\mathrm{D}t} - \frac{\mathrm{D}\vec{v}_g}{\mathrm{D}t}) \tag{1.26}$$

The coefficients C_D, C_L, and C_m are usually determined empirically [34].

According to Newton's second law:

$$\vec{F} = \vec{F}_B + \vec{F}_D + \vec{F}_L + \vec{F}_A = \frac{d}{dt}(\rho_g V \vec{v}) \tag{1.27}$$

When liquid phase is still, only the added mass force, the drag, and the buoyancy are considered in the balance equation. The lift force is zero. However, the added mass force and the drag force oscillate due to the shape oscillations [55].

When the characteristic length characterizing the flow is larger than the size of the body (inhomogeneous flow field), a fixed body is subject to additional inertial and added mass forces:

$$\vec{F}_I = \rho V \vec{v} . \nabla \vec{v} \tag{1.28}$$

$$\vec{F}_A = \rho V C_m \vec{v} . \nabla \vec{v} \tag{1.29}$$

Hence, the total force acting on a sphere in an unsteady inhomogeneous irrotational flow is the

sum of the forces given by equations 1.23,1. 28 and 1.29 [15].

When the body is subjected to a weak rotational flow, the total force acting on a sphere is the sum of the inertial forces, the added-mass forces and the shear-induced lift force:

$$\vec{F} = \rho V \left[\frac{d\vec{v}}{dt} + (\vec{v}.\nabla)\vec{v}\right] + \rho C_m V \left[\frac{d\vec{v}}{dt} + (\vec{v}.\nabla)\vec{v} - \frac{d\vec{v}_p}{dt}\right] + \rho C_l V(\vec{v} - \vec{v}_p) \times \vec{\omega} \quad (1.30)$$

The forces acting on spiraling bubbles were analyzed by Aybers and Tapucu in section 1.3.1. When bubble wake becomes three-dimensional in a zigzag or a helical path, a lateral force also occurs. This force, together with the corresponding torque, initiates the bubble horizontal movements. The wake-induced forces are balanced by added-mass forces and build zigzag and helical rising paths along which the angle between the velocity and the symmetry axis of the bubble remains approximately zero.

The balance of such forces and torques can be modeled using Kirchhoff's equations which is generalized to model the motion of a buoyant rigid body in an inviscid, unbounded and incompressible fluid. Since the boundary layer on a clean bubble is confined to a thin wake region, in contrast to the flow past a rigid body at the same Reynolds number, inviscid flow theory can provide a basis for predicting the forces induced on bubbles [48]. The equations relate the angular and linear velocity of the body to the torques and forces acting on the body:

$$\overline{\overline{\mathrm{A}}}\frac{d\vec{\mathrm{U}}}{dt} + \vec{\Omega} \times \overline{\overline{\mathrm{A}}}\vec{\mathrm{U}} = \vec{F} \quad (1.31)$$

$$\overline{\overline{\mathrm{D}}}\frac{d\vec{\Omega}}{dt} + \vec{\Omega} \times \overline{\overline{\mathrm{D}}}\vec{\Omega} + \vec{\mathrm{U}} \times \overline{\overline{\mathrm{A}}}\vec{\mathrm{U}} = \vec{\Gamma} \quad (1.32)$$

$\vec{F}$ and $\vec{\Gamma}$ are forces and torques acting on the bubble. Forces consist of drag, buoyancy, and lift. The torques are divided into a rotational drag and a wake induced torque [56, 57].

1.3.10. Wall effect

The presence of wall imposes a non-uniform flow around a fluid particle and changes the boundary conditions for the equation of motion of the continuous phase. This new boundary condition changes the bubble terminal velocity and shape. Different correlations proposed to define the effect of wall on bubble terminal velocity are mainly based on the ratio of bubble diameter to the column diameter (λ). When λ is smaller than 0.125, the effect of wall on rising velocity is negligible.

Clift et al. [36] proposed the following correlation for $\lambda < 0.6$.

$$\frac{v_\infty}{v_0} = (1 - \lambda^2)^{3/2} \tag{1.33}$$

This correlation is recommended when Eötvös numbers < 40, Reynolds numbers > 200. For Eötvös numbers > 40, Wallis et al. proposed another equation for $\lambda < 0.6$.

$$\frac{v_\infty}{v_0} = 1.13 \exp(-\lambda) \tag{1.34}$$

Several experimental and numerical studies have been performed on the interaction of a single bubble with a vertical or horizontal wall. The change in the direction of the lift force is dependent on the initial distance between wall and bubble, and the bubble Reynolds number [58, 59].

For evaluating single bubble rising behavior close to wall, de Veris et al. injected different bubble sizes at a fixed distance from the wall. At high Reynolds numbers (400-1000), small bubble (< 0.86 mm diameter) slides along the wall. However, larger bubble collide to wall [58]. Bubbles move away from the wall at low Reynold numbers (< 30).

Lee et al. [60] investigated the wake structure behind an ellipsoidal bubble while rising near a wall. Using Particle Image Velocimetry technique, the spanwise and streamwise vorticity components in wake vortices were observed for bubbles with different distances between the injection nozzle and the wall. The reduced amplitude and wavelength of the bubble oscillations on the wall demonstrated that fluid energy is dissipated due to the wall interference, rather than being used to force the lateral movement of the bubble. When the bubble-wall collision occurs, the streamwise vortex tubes which are attached to the bubble are pushed away from the wall. However, it is not the main reason for the lateral movement of the bubble, and surface energy is produced mainly due to the deformation of the surface during the collision.

Jeong and Park [61] studied the effect of wall surface properties on bubble-wall interaction at high Reynolds numbers (1100). In the absence of wall, the bubble rising trajectory was zigzag. In the case of no-slip and porous surfaces, periodic and non-periodic bouncing was observed, while the zigzag motion remained. Due to the wall effect, the amplitude and wavelength of the lateral movement of the bubble changed. The boundary condition of the wall surface is crucial in energy dissipation during the bubble-wall collision. The bouncing motion of the bubble near the wall is determined by the balance between this energy dissipation and the additional energy resulting from bubble deformation. Pelletier et al. (2015) [62] studied on the bubble rising

dynamics in water after impact with a horizontal wall. The main conclusion of their study was that the bubble deformation before impact acts as a potential energy reservoir, which is drained during the impact. Additionally, they showed that the state of the bubble after rebounding can be predicted from its aspect ratio before the rebound.

1.4. Experimental studies on non-vertical/non-static column

There are few studies on bubble rising dynamics in different static and dynamic geometries.

Table 1.3. Review of bubble rising characteristics in different static and dynamic geometries.

No.	Author	Measurement system	Important observations/results
1	Masliyah et al. [63, 64]	High speed video camera	1) A modified drag coefficient was proposed for small bubbles (Reynolds number < 300, and Weber number < 1.6) rising in an inclined column based on bubble Reynolds number and Eötvös number. 2) For large bubbles, due to bubble oscillations, there are more complex relations between drag coefficient and dimensionless numbers.
2	Drechsler et al. [65]	High speed video camera	They studied the effect of a statically and dynamically inclined column on bubble rising trajectory and velocity. 1) Bubbles' density distribution and flow pattern changed due to vessel motions. 2) The velocity variation was not significant.
3	Assima et al. [7]	Axial gas velocity and local void fraction were measured by dual capacitancewire-meshh sensor inserted in different heights of the bubble column.	A hexapod able to impose various translational and rotational motions on the column of liquid was used for evaluating the effect of externally imposed movements on the hydrodynamics of bubble column reactor, while it was operating in homogenous flow. 1) The emulated oscillations had significant effects on the gas distribution in the column.
4	Yamaguchi et al. [66]	1) The authors measured vertical, radial and tangential velocities of the bubble using a high-speed video camera. 2) The authors measured tangential velocity component of water flow using particle image velocimetry.	They investigated on single bubble behavior in a rotating flow field. 1) The amplitudes and period of bubble motion hardly affected by the frequency of vessel rotation. 2) As the density of water is much greater than that of air, the centrifugal force acting on the water is stronger than that acting on the bubble. Therefore, the water is forced to move outward more strongly than the bubble, and, as a result, the bubble moves inward. 3) The amplitudes and period of bubble trajectory were non-dimensionalized by the bubble diameter and the terminal bubble velocity and correlated as functions

			of the Eötvös number.
5	Li et al. [67]	High speed video camera	1) They calculated the drag and lift forces for the bubble rising in linear shear flow in water based on the force balance. 2) The quasi-steady lift coefficient caused by shear flow decreased with the increase of shear flow magnitude and bubble diameter.
6	Legendre et al. [68]	High speed video camera	They studied bouncing of millimetric toluene drops impacting at their terminal rise velocity in water on a horizontal plate. 1) 80% of the energy dissipated during interaction with the wall.
7	Van Nierop et al. [69]	High speed video camera	They studied the motion of a single bubble in a solid-body rotational flow. 1) There is a strong shear dependence of the drag coefficient for solid-body rotation similar to the linear shear flow.
8	Rastello et al. [70]	High speed video camera	Drag and lift forces are measured for a single bubble in a solid-body rotating flow of silicon oil. 1) The drag coefficient increased as the local shear rate increased 2) The diameter at which transition from spherical to deformed shape occurs slightly differs from the uniform flow.
9	Tomiyama et al. [71]	High speed video camera	The authors evaluated the lift coefficient of a single air bubble while rising in a simple shear flow of glycerol-water solution. 1) Lift coefficient for small bubbles can be well predicted with the bubble Reynolds number 2) Lift coefficient for large bubbles is a function of Eötvös number that is based on the maximum horizontal dimension of the deformed bubble.

1.5. Simulation

1.5.1. Hierarchy of models

Three main techniques for modeling of bubble columns are the Direct Numerical Simulation, the Eulerian-Lagrangian, and the Eulerian-Eulerian approaches [72]. In the Direct Numerical Simulation, a set of transient Navier-Stokes equations are solved for both continuous and dispersed phases. As the fluid interface is tracked in this method, the selected mesh required is to be very fine [73]. More details about this method are provided in the following section.

The eulerian-lagrangian approach is the next coarser level, in which the continuous phase is

described by the Navier–Stokes equations and the dispersed phase is tracked by solving the Newtonian equation of motion [73, 74]. In this approach, bubbles are considered as points, and their size and shape are included in the equation only through the semi-empirical drag coefficient. In this approach, a single-phase turbulence model may be used, but to cover the presence of bubbles the effective transport coefficients and source terms for turbulence shall be added [75-77]

The third approach in simulating bubble column reactors is the Eulerian-Eulerian approach, which is of a lower level of computational cost, usually used for flow pattern studies. This approach solves a set of Navier Stokes equations for both the continuous phase and the dispersed phase. The terms of the equation of motion of bubbles are implemented through interphase interaction terms [78].

1.5.2. Direct numerical simulation

Direct numerical simulation methods can be classified into fixed-grid and moving-grid methods. In moving-grid methods, the interface is constructed sharply with a set of nodal points of the computational mesh. This method tracks the exact position of the interface. However, the marker particles have to be relocated, thus remeshing is needed when interface undergoes large deformations.

Two approaches for solving a moving interface in fixed grid are front tracking and front capturing [78]. In the front tracking method, marker points are assigned to the interface and track its' movement through advection of the Lagrangian markers on the fixed grid [73, 79].

The front capturing method is the Eulerian treatment of the interface. In this method, the interface is represented by an indicator function that is defined on a fixed grid. The indicator function may be a volume fraction, a level set or a phase-field [78, 79]

The Volume of fluid (VOF) method is used for simulation of two or more immiscible fluids, where the position of the interface is required to be tracked [78]. This method uses a volume fraction function known as color function to define the interface in each cell and trace it using an advection equation. Several algorithms have been proposed for the construction of the two-fluid interface in each cell. The most recent one, known as the most accurate technique, is the piece-wise linear interface construction (PLIC) method [79].

When the volume fraction is the indicator function, the convection scheme has to guarantee that the volume fraction remains within its physical bounds, so it may cause the interface to diffuse. This problem causes numerical instabilities and poor representation of capillary effects. The surface tension term in the Navier-Stokes equation creates additional difficulties. The problem was reported as the existence of spurious currents in the flow field from these numerical simulations. These currents are vortices that appear in the neighborhood of interfaces despite the absence of any external forces [34].

Recently, Lattice-Boltzmann methods (LBM) have become popular for their capabilities in simulating finite Reynolds-number multiphase flows [73]. This method uses a particle-based discretization method to solve the Boltzmann equation and is especially attractive for treating multiple moving objects (particles, bubbles or droplets) as it avoids dynamic remeshing which can be prohibitive for a large number of moving particles [79]. One of the advantages of the Lattice Boltzmann method is that gas-liquid interface is modeled with solid boundaries implemented at the particle boundary without the need for solving an additional equations akin to the interface capturing methods [80].

LBM simulations of two-phase flow systems with low Morton numbers and large Eövtös numbers are challenging. As low viscosities are tantamount to low relaxation times, decreasing too much the relaxation time causes the explicit LBM scheme to be numerically unstable. Recently, Sankaranarayanan et al. applied an implicit LBM scheme to study the dynamics of isolated gas bubbles rising in quiescent liquids. This method is immune against numerical instability, in addition to be able to simulate bubble dynamics over a very broad range of Morton and Eövtös numbers [73, 81].

Table 1.4. Different simulation techniques for multi-fluid flows with sharp interfaces [73].

Method	Advantages	Disadvantages
Level Set	Conceptually simple	Limited Accuracy Volume Loss
Marker Particle	Extremely accurate Robust Accounts for substantial topology changes in the interface	Computationally expensive Redistribution of marker particles required
VOF	Accurate Accounts for substantial topology changes in the interface	Artificial coalescence and break-up
Lattice Boltzmann	Accurate Accounts for substantial topology changes in the interface	Difficult to implement Artificial coalescence and break-up
Front Tracking	Extremely accurate Robust Accounts for substantial topology changes in the interface No automatic coalescence and break-up	Mapping between interface and Euler grid required Dynamic meshing required Volume loss

1.5.3. Previous studies on single bubble simulation

Delnoij et al. [82] and Krishna et al. [83] applied the VOF method for two-dimensional modeling of a single bubble rising in a quiescent liquid. Simulation results well agreed with the experimentally observed rise velocities and bubble shape. Hassan et al. [84] simulated bubble rising in different liquids using the VOF approach. The authors investigated the effect of Reynolds number, Weber number, and bubble aspect ratio on bubble rising path in both Newtonian and non-Newtonian fluids. A transition from zigzag trajectory to the spiral one was reported as path instability observed for bubbles with 15.63 and 21.21mm diameters. Based on the resulting velocity vectors, the authors suggested the repeating pattern of swirling vortices as the cause of bubble zigzag behavior for a 5.76 mm diameter bubble. However, two counter-rotating trailing vortices at the back of the larger bubbles (15.63 and 21.21mm) generate a spiral rising path. Zahedi et al. [72] investigated the bubble formation and rising trajectory using the VOF method. The authors studied the impact of different physical properties of liquid phase, injection nozzle and operating conditions on bubble size, rising path and detachment frequency. Bubble size and detachment time is found to be a linear function of surface tension. Single bubble formation and bubble column dynamics have been simulated by Ma et al. [85], using the

VOF approach. For tracking the gas-liquid interface, the piecewise linear interface construction (PLIC) algorithm was used. Also, the pressure implicit splitting operator (PISO) algorithm was applied for solving the transient conservation equations of mass and momentum, while the gravitational forces and surface tension effects were considered. Surface tension effects in addition to the impact of liquid phase viscosity and density, orifice size, and operating conditions on single bubble characteristics in terms of rising path and bubble coalescence were analyzed. Zheng et al. [86] modeled the motion of a single air bubble in the aluminum smelting process using VOF method to capture details of the gas-liquid interface. The authors applied adaptive mesh refinement which reduced the computational time significantly. Tomiyama et al. [87] analyzed the single bubble rising in a stagnant liquid and a linear shear flow using VOF method, and suggested that this method predicts the effect of liquid properties on bubble motion properly. Simulated bubbles in linear shear flow, migrated towards a lateral direction which was compatible with the experimental data. The magnitude and direction of the lateral movement of the bubble due to shear flow in the liquid are dependent on the liquid properties (Eötvös and Morton numbers). Also, interactions between wake and internal flow of the bubble and external shear flow in the liquid, are essential in bubbles' lateral movement. Xu et al. [88] studied argon bubble dynamics in liquid metal in terms of bubbles' trajectory, shape, and terminal velocity. It is shown that bubbles with 3-10 mm diameter, rise in a spiral way and their shape changes rapidly. Whereas, for bubbles with 10-20 mm diameter, the rising path was rectilinear while their shape did not change considerably.

van Sint Annaland [79], developed a model for a single rising bubble using the VOF approach by implementing the Gerris solver and claimed that the model is appropriate for high density and viscosity ratios (typically one hundred). Pourtousi et al. [89] studied the formation and hydrodynamics (i.e., bubble size, shape, velocity and interaction of two bubbles) of single methane bubble in a bubble column filled with water for application in biomass production. The authors employed the VOF method and compared the simulation results with the study performed by Ma et al. for both methane and air. The effects of inlet gas velocity, gas orifice diameter, and sparger configuration were examined on bubble dynamics, detachment from the sparger, and bubble coalescence. The authors suggested that the existence of a specific distance between orifices will be useful in producing small and uniform bubbles, which improves the gas

and liquid interfacial area and bubble column efficiency.

Wang et al. [90] performed a three-dimensional simulation for an air bubble rising in water and argon bubble in liquid steel. The authors used Ansys Fluent and investigated on bubble rising path, coalescence and bouncing using VOF approach. The results of velocity and pressure distributions showed that velocity of the first bubble is less than the trailing bubble, so the two coaxial bubbles coalesced after rising for a while. Li et al. [91] simulated the single bubble rising and calculated the lift coefficient in shear liquid flow considering the effect of bubble size, liquid velocity, and liquid viscosity. The oscillation amplitude increased as the viscosity of the fluid decreased. In high viscous liquid, the bubble migrated towards the moving wall in a line, and the lift coefficient was rather constant. Whereas the trajectory of the bubble towards the moving wall was oscillatory and the lift coefficient was not constant in low viscosity fluid. The magnitude of shear stress influenced the start of the bubble lateral movement but was not effective in later movements.

Wang et al. [92] used the Gerris solver, for the simulation of a single oil-coated bubble rising in still liquid. Oil-coated bubbles are more spherical compared with non-coated bubbles. Also, they have a lower rise velocity and a more stable shape. The authors implemented the VOF approach with dynamic adaptive mesh refinement, in Gerris solver to evaluate the terminal rise velocity, bubble shape, and trajectory.

To assess the impact of considering the third dimension in single bubble rising simulation, van Sint Annaland et al. [93] compared the results of a three dimensional Front Tracking model with the results of a two-dimensional VOF simulation. Calculated terminal velocity and mean aspect ratio of the bubble agreed well with the experimental data provided by Tomiyama et al. [87] for both cases. Although for bubbles with equivalent diameters less than 3 mm, the surface tension force is dominant, parasitic currents were not observed in both simulations. The small difference between simulation results and available experimental data on bubble terminal velocity, and drag coefficient were attributed to water contamination. The sharp reduction in drag coefficient in small bubbles achieved by three-dimensional Front Tracking model could not be calculated by two-dimensional VOF simulation. Cano Lozano et al. [94] performed bubble rising simulation using Gerris solver and applied adaptive mesh refinement. The resulting plot of terminal velocities versus bubble diameter demonstrated the onset of zigzag bubble motion and

oscillation reduction towards a rectilinear path with an increase in bubble diameter. The authors used velocity distribution profiles to describe the transition in bubble rising path and attributed the rectilinear bubble path to the axisymmetric wake behind the bubble and the zigzag trajectory to the two-counter rotating vortices with a plane of symmetry in the wake behind the oscillating bubble.

The Rothman-Keller model, the Shan-Chen model, and the free-energy approach are three different types of LBM-based multiphase flow models [95]. Traditional LBM approaches in multiphase flows suffer two limitations: (i) local instabilities near the interface in the case of high-density ratios, (ii) most of the schemes cannot simulate high Reynolds number flows. Comparing the stability and performance of the three methods for simulating multiphase flow, Huang et al. [96] recommended the free-energy approach for immiscible fluids with large density and viscosity ratios. Zheng et al. [97] proposed the Galilean invariant free-energy Lattice Boltzmann model for high-density ratios. Anwar et al. [95] used the Rothman-Keller color model. However, this latter model was found to be unstable for high density or viscosity ratios. Table 1.5 shows different methods developed to overcome the limitations in bubble dynamics simulation using LBM models.

Table 1.5. Model development methods [98].

Base LB model	Model development method to simulate low Morton number systems
Free Energy	Projection method
Free Energy	Galilean invariance
Free Energy	Multiple-relaxation-time (MRT)
Shan-Chen	Multiple-relaxation-time (MRT)
Shan-Chen	Multiple-relaxation-time and adaptive mesh refinement

1.5.4. Selection of the solver

Dominant effect of surface tension forces, large density and viscosity ratios, and complex interface geometries are the specification of each multiphase system shall be considered for solver selection [94]. To determine the CFD package tool that presents the best results, Cano

Lozano et al. [94] evaluated two different solvers for VOF approach for the one which requires lower computational cost and avoids the appearance of numerical problems such as the parasitic currents. Simulations were performed using the Interfoam and the Gerris solver to model single bubble rising in a two-dimensional axisymmetric domain. Based on mesh resolution and computation time, parasitic currents were observed in the simulation results obtained by Interfoam. Since Gerris solver allows a dynamic adaptive mesh refinement along the interface or based on the vorticity magnitude, the necessary resolution for accurate solutions at the key regions can be achieved without a significant increase in the computation time. The authors concluded that the adaptive mesh refinement technique and the surface tension treatment in Gerris made this solver more suitable for the case of air bubble rising in water, as parasitic currents were not observed when the Gerris solver was used. Inzoli et al. [98] applied the Ansys Fluent and Gerris solver to find the best solver for interface reconstruction. The CLSVOF (i.e., coupled Level Set and VOF method) and VOF approaches available in Ansys Fluent were compared with the VOF approach in the original and modified (Ghost Fluid Method, GFM) versions available in Gerris solver. The interface curvature calculation in the Gerris solver resulted in more stable results as compared to Ansys Fluent. In the case of large bubbles (2.5 cm diameter), similar results were obtained using all three methods, while limitations observed in reproducing the correct bubble shape using CLSVOF in Ansys Fluent. In the case of small (300 μm diameter) and medium-size (0.9 mm diameter) bubbles, large errors was observed in rising velocity, which was due to the curvature calculation in Ansys Fluent code. The spurious currents were significant, and rising speed was affected strongly for smaller bubbles. However, using the Gerris solver, such problems were not observed, and this solver was able to reproduce bubble with physical shape, terminal velocity and velocity field around and inside. Using Gerris solver and grid refinement based on the velocity magnitude, Gumulya et al. [99] simulated single bubble rising dynamics. The resulted trajectory and rising velocity well compared with the observations of Veldhuis et al.. In another study on the simulation of two inline bubbles in stagnant liquid, Gumulya et al. [100] implemented an adaptive mesh refinement in Gerris solver. The grid was refined as the interface was resolved with a cell size of R/110 (R is the initial radius of the bubbles) while the size of other cells was R/3.44. Nichita et al. [101] performed single bubble rising simulation using Ansys Fluent. The authors applied three methods of Level Set,

VOF and CLSVOF. Using VOF, the simulated trajectory did not show any oscillation, which is not physically correct. Whereas, using CLSVOF, the oscillation in the rising path appeared, which demonstrates more accuracy in the CLSVOF method, for simulating vortex shedding behind the rising bubble. The bubble rise velocity in both cases was evaluated with the available experimental data, and it was 7.8% higher than the observations using CLSVOF, and 12.4% higher using VOF. Also, CLSVOF predicted the frequency of bubble helical motion within 9% of accuracy while the VOF failed, due to the aforementioned non-oscillatory path.

1.5.5. Volume of Fluid method

1.5.5.1. Governing equations

The governing equations in terms of continuity and momentum conservation equations for an incompressible, unsteady and multi-fluid flow are given by the following expressions [82, 83]:

$$\nabla.\vec{v} = 0 \tag{1.35}$$

$$\frac{d(\rho\vec{v})}{dt} + \nabla.(\rho\vec{v}\vec{v}) = -\nabla P + \nabla.\bar{\bar{\tau}} + \vec{F}_s + \rho\vec{g} \tag{1.36}$$

The surface tension force, $\vec{F}_s$, is added to the momentum equation as a source term.

1.5.5.2. Surface tension force

In interface-capturing methods, the interface is not tracked explicitly and, consequently, its exact shape and location are unknown. Therefore, the source of momentum due to surface tension, cannot be evaluated directly. Brackbill et al. [102] proposed the continuum surface force (CSF) model, which represents the surface tension effects as a continuous volumetric force acting within the interface region:

$$\vec{F}_s = \sigma k \nabla\gamma \tag{1.37}$$

where κ is the curvature of the interface:

$$k = \nabla.\left(\frac{\nabla\gamma}{|\nabla\gamma|}\right) \tag{1.38}$$

Based on the curvature calculation technique, CSF methods belong to two categories: the Classic Continuum Surface Force (CCSF) and the Height Function Continuum Surface Force (HFCSF).

While in CCSF, the curvature is calculated by means of the divergence of normal vectors, the HFCSF allows better approximation of the curvature, which is calculated for the plane curve $y=f(x)$ via [103]:

$$k = \frac{y''}{(1+y'^2)^{3/2}} \tag{1.39}$$

Using the Height Function technique, a numerical balance between the pressure gradient and the surface tension force is to be reached with the elimination of spurious currents in the case of a static interface [104].

The smoothed CSF model applies a smoothed volume fraction to compute the curvature. Using this method, the spurious currents are reduced by one order of magnitude. In this method, a smoother correction proposed by Lafaurie et al. [105] is applied:

$$\widetilde{\alpha_P} = \frac{\sum_{f=1}^{N} \alpha_{Lf} S_f}{\sum_{f=1}^{N} S_f} \tag{1.40}$$

Where $\mathcal{S}_f$ is the magnitude of the face area, *P* denotes the cell index and the subscript *f* represents the face index. α_{Lf} is calculated using the linear interpolation from cell to face center [106]. The smoothed volume fraction is then used for calculating the unit normal to the interface, with the curvature and surface tension force being the same as in the non-smoothed method [107].

Raeini et al. [108]] introduced a sharp surface force (SSF) formulation to calculate the capillary force, based on CSF to reduce the parasitic currents. SSF has been reported to reduce the spurious currents by two to three orders of magnitude in comparison to CSF [109]. This reduction is achieved by smoothing the indicator function for calculating the curvature and sharpening it for calculating the Dirac delta function in the surface tension force calculation [103].

1.5.5.3. Interface reconstruction

The VOF method employs the volume fraction as an indicator function to track the interface.

The fractional volume function α is defined as:

0: for a cell with pure gas,

1: for a cell with pure liquid,

0 – 1: for a cell with a mixture of gas and liquid, in which the interface exists.

Motion of the gas-liquid interface is tracked through solution of fractional volume or 'color' function transport equation [82, 83]:

$$\frac{d}{dt} + (\vec{v}.\nabla) = 0 \tag{1.41}$$

Mixture density and viscosity are calculated based on linear averaging of densities and viscosities of the continuous and dispersed phases using the volume fraction function,

$$\rho = \rho_l \alpha + \rho_g (1 - \alpha),\ \mu = \mu_l \alpha + \mu_g (1 - \alpha) \tag{1.42}$$

The volume fraction function or the color function which is used for interface indication is not associated with a particular front grid. Algorithms known for interface construction in the cells containing mixture of phases are donor-acceptor method, simple line interface calculation (SLIC) method and piecewise linear interface calculation (PLIC) method. The most precise interface reconstruction method is the PLIC method [79].

Another volume fraction transport scheme, in which the location and thickness of the interface are both controlled by an accurate algorithm based on Flux-Corrected Transport (FCT) scheme [103, 110] has been developed in the JADIM code [111]. In this method the transport equation is written as:

$$\frac{d\alpha}{dt} + \nabla.(\alpha\vec{v}) = \alpha\nabla.\vec{v} \tag{1.43}$$

The drawback in the methods without interface reconstruction concerns the spreading of the interface over numerous cells.

1.5.5.4. Time advancement algorithm

For temporal discretization of the governing equations, when using explicit time integration, the time step is restricted to the stability limit, i.e., the Courant Friedrichs Lewy (CFL) condition. CFL is defined as the relation between the size of the computational cell, the transient time step size, and the local fluid velocity within the cell [112],

$$CFL = \frac{\Delta t}{\Delta x_{cell}/v} \tag{1.44}$$

Where Δt is the time step during the simulation, Δx_{cell} is the size of one side of the cell, and v is

the velocity in the cell. The time step for integration of the bubble motion equation is required to be small enough with respect to the time needed for a bubble to pass a control volume of a continuous phase.

1.5.5.5. Mesh resolution

For detailed capturing of the interface between gas and liquid, mesh size shall be substantially smaller than the bubble size ($\Delta x_{cell} \ll d$) [73]. In addition to the high grid resolution required for interface capturing methods, for a system with high viscosity ratio the resolution of the computational domain becomes more crucial [113].

There is a strong dependency of the terminal rise velocity on the grid size in air-water systems. For water-glycerol mixtures with a viscosity of 0.019 Pa.s, the satisfactory grid independency of horizontal bubble diameter obtained by 9.23 CPD (cells per bubble diameter) [114]. Whereas, in another study, the authors did not achieve the grid independent results for lift coefficient with grid resolution up to 16 CPD. The authors selected 16 CPD as this resolution was the best selection based on the physical correctness of the results and limitations in computational capacities. To reduce computational time, the adaptive mesh refinement feature of Ansys Fluent allows to refine or coarsen meshes based on geometric and numerical solution data [115]. The mesh is dynamically refined at the interface or for cells with high velocity and coarsened back when the interface moves out of that region, or the velocity reduces in the cell.

Three-dimensional simulations are necessary to capture the regime transitions for bubble rising path (rectilinear, zigzag and helical). The inter-regime boundaries are controlled by the interaction of shape deformation, and the associated vorticity generation and wake formation. To minimize the spurious vorticity, accurate modeling of surface tension is necessary. To maintain the numerical convergence, Cano Lozano et al. [94] used a resolution of 128 grid points per bubble diameter. The authors used a very large tank of 8×8×128 bubble diameter to follow a bubble over a long time. This leads to the 17 billion grid points in a regular grid which reduced down to around 10 million grid points using an adaptive mesh refinement [94, 104].

1.5.5.6. Sources of spurious currents

As mentioned in Section 1.5.4, the Eulerian methods produce additional vorticity close to the

interface that leads to non-physical spurious currents. The sources of vorticity due to curvature gradients can be identified using the vorticity equation:

$$\frac{d\vec{\omega}}{dt} + (\vec{v}.\nabla)\vec{\omega} + (\vec{\omega}.\nabla)\vec{v} = \frac{\mu}{\rho}\nabla^2\vec{\omega} - \frac{\sigma}{\rho}\nabla k \times \nabla\alpha \tag{1.45}$$

When the curvature is constant during the simulation, no spurious currents develop, as the source term is zero. Otherwise, if the balance between the pressure gradient and the surface tension force is not achieved, the surface tension force can contribute as a source term to vorticity production [104].

The spurious currents grow linearly with surface tension at the initial stage of simulation and the intensity of spurious currents is:

$$v_\sigma \sim \frac{\sigma \Delta t}{\rho d^2} \tag{1.46}$$

Considering long-time simulations, provided the viscous effects are dominant, the spurious currents become balanced by the viscous term:

$$v_\sigma \sim \frac{\sigma}{\mu} \tag{1.47}$$

When inertia is dominating, the spurious currents are controlled by the inertia term:

$$v_\sigma \sim \sqrt{\frac{\sigma}{\rho d}} \tag{1.48}$$

Legendre et al. [103] investigated the capability of the VOF method to calculate the curvature and evaluate the magnitude of spurious currents due to errors in the curvature calculation stemming from advection in translating and rotating flows. It was shown that when the bubble is translated by a uniform flow, similar intensities of spurious currents are obtained using the Height Function for different transport schemes and the spurious currents were enhanced as compared to the static case [103, 104]. However, the spurious currents obtained with CCSF and SSF methods were in good agreement with those obtained in the static case [103].

When the bubble is placed in a rotating flow, the effects of the transport scheme on the spurious currents are enhanced as compared to the translating case. With both curvature calculations (i.e., the height function and the divergence of the unit normal to the interface) the use of the VOF-PLIC scheme leads to decreased spurious currents in comparison with the VOF-FCT scheme, especially when compared with the translating case.

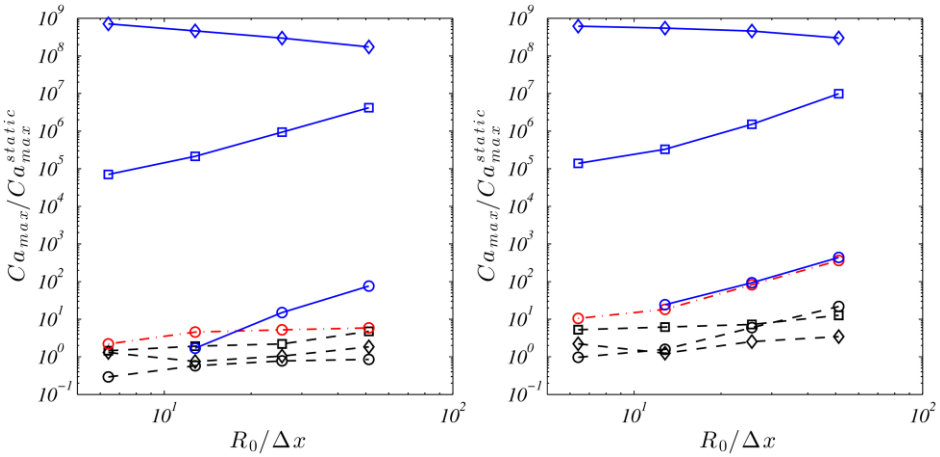

Figure 1.12. Ratio of maximum spurious current intensity in the translating (a) and rotating (b) cases over spurious current intensity in the static case. ( ) VOF-FCT-CCSF; ( ) VOF-FCT-HFCSF; ( ) VOF-PLIC-CCSF; ( ) VOF-PLIC-HFCSF [104]

As shown in Figure 1.12, the ratio of maximum spurious current intensity in dynamic cases over that obtained in the static case is close to one for CCSF and SSF methods. This indicates that when using these methods, the errors in curvature calculation after advection are of the same order of magnitude with those obtained in the static bubble case. Consequently, the main spurious-current magnifiers are the curvature calculation rather than the advection scheme.

In contrast, using the Height Function method, the spurious currents are magnified by the advection errors.

It can be deduced that the curvature errors are dominated by the advection errors rather than by inaccurate curvature calculation. Hence, despite the fact that the Height Function curvature calculation is very accurate and is particularly suitable for the case of static bubbles, the errors are generate during the advection step [103, 104].

1.5.5.7. Non-inertial frame of reference

Recently, numerical simulations have been performed for analyzing the hydrodynamic behavior of gas-liquid flow in packed beds in inclined and rolling conditions. Transient three-dimensional Euler–Euler CFD models for porous media have been developed for inclined packed beds under different operating conditions [116] and also for packed beds subjected to roll motions [117]. The model was shown to be able to predict the liquid holdup and pressure drop as well as the morphological characteristics of the traveling waves inside the bed.

Motamed-Dashliborun et al. [117] applied moving reference frame and sliding mesh techniques to simulate the dynamic behavior of gas-liquid flows in packed beds subjected to tilts and oscillations. To incorporate acceleration/deceleration force terms resulting from the transformation of the inertial reference frame to the non-inertial frame, the authors reformulated the governing equations of the gas and liquid phases to account for the influence of roll motion on the fluid dynamics in the porous medium.

In general, when the external boundary to a fluid is in motion, it is possible to choose a frame of reference relative to which the space domain is at rest. As a result, the acceleration of an element of fluid relative to the moving frame is different from the acceleration in the inertial frame. So, the equation of motion shall be modified accordingly [16]:

When a moving reference frame is translated, the velocity and acceleration of the moving reference frame relative to the inertial frame are:

$$\vec{v}_t = \frac{d\vec{x}}{dt} \tag{1.49}$$

$$\vec{a}_t = \frac{d\vec{v}_t}{dt} \tag{1.50}$$

Where x, v and a are position, velocity, and acceleration of the moving frame, respectively. The linear acceleration term will be added to the LHS of the momentum equation [16]:

$$\frac{d(\rho\vec{v})}{dt} + \rho\vec{a}_t + \nabla.(\rho\vec{v}\vec{v}) = \cdots \tag{1.51}$$

Note that the momentum equation is now expressed in terms of the velocity relative to the moving reference frame $\vec{v}$ and that the same transformation has to be applied to the transport equation for the indicator function (equation 1.41).

In order to include the translational and rotational movements of the non-inertial reference frame relative to the inertial one, four acceleration terms will be added to the momentum conservation equations, i.e. Coriolis acceleration, the centripetal acceleration, and the accelerations due to unsteady variation of the rotational and translational velocities.

When the frame is rotating with angular velocity $\vec{\omega}$, about a point O, the acceleration of an element of the fluid relative to that point will be related to the acceleration of the element relative to the rotating frame as follows:

$$\vec{v}_s = \left(\frac{d\vec{y}}{dt}\right) + \vec{\omega} \times \vec{y} \tag{1.52}$$

$$\vec{a} = \left(\frac{d\vec{v}_t}{dt}\right) + \vec{\omega} \times \vec{v}_s \tag{1.53}$$

$$\vec{a} = \left(\frac{d^2\vec{y}}{dt^2}\right) + 2\vec{\omega} \times \left(\frac{d\vec{y}}{dt}\right) + \left(\frac{d\vec{\omega}}{dt}\right) \times \vec{y} + \vec{\omega} \times (\vec{\omega} \times \vec{y}) \tag{1.54}$$

$\vec{y}$ represents the position of an element of fluid relative to the point O, $\left(\frac{d^2\vec{y}}{dt^2}\right)$ is the acceleration of the element relative to the rotating frame of reference, and $\frac{d\vec{y}}{dt}$ is the velocity of the element in this frame.

The absolute acceleration of the element will be:

$$2\vec{\omega} \times \vec{v} + \frac{d\vec{\omega}}{dt} \times \vec{y} + \vec{\omega} \times (\vec{\omega} \times \vec{y}) \tag{1.55}$$

Steady rotating motion results in Coriolis and centrifugal forces. $2\vec{\omega} \times \vec{v}$ is the deflecting or Coriolis force, which is perpendicular to both $\vec{v}$ and $\vec{\omega}$, and $\vec{\omega} \times (\vec{\omega} \times \vec{y})$ is the centrifugal force. As v is the velocity of the element in the non-inertial frame. The transformation of fluid velocities from the inertial frame to the non-inertial frame is made through:

$$\vec{v}_q = \vec{v}_s - \vec{v}_{'} \tag{1.56}$$

$$\vec{u}_{'} = \vec{v}_t - \vec{\omega} \times \vec{y} \tag{1.57}$$

The conservation equations for a moving reference will be then:

$$\frac{d\alpha}{dt} + \nabla.(\alpha\vec{v}_q) = 0 \tag{1.58}$$

$$\frac{d(\rho\vec{v}_q)}{dt} + \nabla.\left(\rho\vec{v}_q\vec{v}_q\right) + \rho\left(2\vec{\omega} \times \vec{v}_q + \vec{\omega} \times (\vec{\omega} \times \vec{r}) + \frac{d\vec{\omega}}{dt} \times \vec{r} + \frac{d\vec{v}_t}{dt}\right) = \tag{1.59}$$

$$-\nabla P + \nabla.\bar{\bar{\tau}} + \rho\vec{g} + \vec{F}_s$$

Where α is the volume fraction.

1.5.5.8. Sliding mesh

In this method, the computational domain slides (i.e., rotate or translate) by defining the mesh velocity, such that the velocity of an element of the fluid is maintained in a stationary reference frame while the boundaries and the cells move in a rigid-body motion [115, 117].

The velocity of mesh for the roll motion case is defined as the product of angular velocity and position vector:

$$\frac{d\alpha}{dt} + \nabla.(\alpha(\vec{v}_s - \vec{v}_{mesh})) = 0 \quad (1.60)$$

$$\frac{d(\rho\vec{v}_s)}{dt} + \nabla.(\rho(\vec{v}_s - \vec{v}_{mesh})\vec{v}_s) = -\nabla P + \nabla.\bar{\bar{\tau}} + \rho\vec{g} + \vec{F}_s \quad (1.61)$$

$$\vec{v}_{mesh} = \vec{\omega} \times \vec{r} \quad (1.62)$$

1.6. Conclusion and research opportunities

Despite the intensive research performed on the hydrodynamics of bubble column reactors (including studies on gas holdup, bubble characteristics, and regime transition) and single bubble rising dynamics (including studies on shape, trajectory, and terminal velocity of bubble) in vertical static liquid columns, a few studies have thus far been considered in the literature and dedicated to bubble columns under dynamic movements. The reviews, addressed in Section 1.4, on the effect of inclination angle and motion frequency on bubble rising dynamics, highlight the need to more detailed studies on bubble rising characteristics and the surrounding liquid flow field in floating condition, and even more new studies on the effect of any additional motion of the column on bubble rising hydrodynamics.

To the authors' best knowledge, currently, there is not any literature on the effect of a moving column on bubble formation and detachment characteristics, i.e. the frequency of detachment, bubble size, and bubble rising behavior after detachment, which are the key parameters in hydrodynamic characteristics prevailing in the column.

As stated in Section 1.5.3, there are several numerical studies on single bubble or a few bubbles rising in a still liquid, aiming to more deep understanding of rising dynamics, liquid flow field around the bubble and transformations in forces involved in bubble rising. Similarly, such information is critical for the cases whereby the column experiences rotational and translational movements.

1.7. Objectives

Bubble column reactors have a broad application in chemical and petrochemical industries. Several studies have been performed on their hydrodynamics and mass transfer characteristics.

Despite their growing application in offshore oil and gas industry, and especially on FPSO units [2], little attention has been devoted to analyzing their performance under harsh environmental condition due to the wind and marine currents. To the best of authors' knowledge, studies on performance deviation of bubble column reactors whereby it experiences rotational and translational movements, is limited to two works on bubble flow behavior in liquid column, both highlighted the need for more studies on the detailed hydrodynamics and mass transfer characteristics in this type of reactors [7, 65].

To generate a basis for understanding the complex behavior of multi-bubble flow in reactors operating in floating condition, experimental studies will be performed to analyze single bubble hydrodynamics in an inclined column. As the bubble-wall interaction has a major impact on the hydrodynamics of bubble column reactor under floating conditions, the modifications in bubble trajectory, velocity, and aspect ratio imposed by the bubble-wall interactions will be studied.

1.8. Nomenclature

a	Acceleration
$\overline{\overline{\mathrm{A}}}$	Added mass tensor
A_{s}	Bubble surface area
C_{D}	Drag coefficient
C_L	Lift coefficient
C_m	Virtual mass coefficient
d	Bubble diameter
$\overline{\overline{\mathrm{D}}}$	Added rotational inertia tensor
d_{e}	Equivalent bubble diameter
E	Aspect ratio
Eo	Eötvös number
F	Force
f	Frequency
g	Gravitational acceleration

k Local surface curvature

Mo Morton number

P Pressure

$\vec{r}$ Position vector

r Bubble radius

r_e Equivalent bubble radius

R Universal gas constant

Re Reynolds number

S_f Magnitude of the face area

t Time

Ta Tadaki number

U Particle velocity

v Velocity

V Volume

v_σ Intensity of spurious current

$\acute{v}$ Velocity of the moving frame

v_r Relative velocity

v_s Phase velocity viewed from the stationary frame

v_t Translational frame velocity

v_q Phase velocity viewed from the moving frame

v_∞ Terminal velocity

v_0 Terminal velocity of bubble in an infinite container

We Weber number

x Bubble deformation

Greek letters

ρ Density

μ Viscosity

$\bar{\bar{\tau}}$ Stress tensor

σ Surface tension

ϕ Phase lag

λ Ratio of bubble diameter to vessel diameter

$\vec{\Omega}$ Fluid particle angular velocity

$\vec{\Gamma}$ Torque

$\vec{\omega}$ Angular velocity

α Volume fraction

Subscripts

A Added mass

B Buoyancy

c Continuous phase

f Face index

g Gas

I Inertia

D Drag

h Horizontal

L Lift

l Liquid

P Cell index

s Surface tension

v Vertical

1.9. References

1. Cullinane, J.T., Yeh, N., Grave, E. *Effects of tower motion on packing efficiency*. 143766 SPE Conference Paper. 2011. Brazil.

2. Reay, D., Ramshaw, C., Harvey, A. *Process Intensification: Engineering for efficiency, sustainability and flexibility*. 2013. Butterworth-Heinemann.
3. Motamed Dashliborun, A. *Performance of multiphase packed-bed reactors and scrubbers on offshore floating platforms: hydrodynamics, chemical reaction, CFD modeling and simulation*. 2018, PhD Thesis, Universite Laval.
4. Markus Duss, M.R. *Columns subject to motion: Maldistribution sensitivity and susceptibility*, in *10th International Conference on DISTILLATION & ABSORPTION*. 2014: Friedrichshafen · Germany.
5. Horoun, Y., Raynal, L., Alix, P. *Distributor tray for offshore gas/liquid contact column*. 2015: US Patent US9120064B2.
6. Kantarci, N., Borak, F., Ulgen, K.O. *Bubble column reactors.* Process biochemistry, 2005. 40(7): p. 2263-2283.
7. Assima, G.P. et al. *Capacitance wire mesh imaging of bubbly flows for offshore treatment applications.* Flow Measurement and Instrumentation, 2015. 45: p. 298-307.
8. Deen, N.G. et al. *Bubble Columns*, in *Ullmann's Encyclopedia of Industrial Chemistry. Weinheim* 2010, Wiley-VCH Verlag.
9. Besagni, G., Inzoli, F., Ziegenhein, T. *Two-Phase Bubble Columns: A Comprehensive Review.* ChemEngineering, 2018. 2(2): p. 13.
10. Shu, S. et al. *Multiscale Multiphase Phenomena in Bubble Column Reactors: A Review.* Renewable Energy, 2019.
11. Syed, A.H. *Modeling of Two & Three Phases Bubble Column Modélisation dΓune Colonne à bulles Biphasique et Triphasique*. 2017, PhD Thesis, Université de Sherbrooke.
12. Deckwer, W.D., Burckhart, R., Zoll, G. *Mixing and mass transfer in tall bubble columns.* Chemical Engineering Science, 1974. 29(11): p. 2177-2188.
13. Krishna, R. et al. *Influence of increased gas density on hydrodynamics of bubble-column reactors.* AIChE journal, 1994. 40(1): p. 112-119.
14. Liu, L. et al. *Experimental studies on the terminal velocity of air bubbles in water and glycerol aqueous solution.* Experimental Thermal and Fluid Science, 2016. 78: p. 254-265.
15. Magnaudet, J., Eames, I. *The motion of high-Reynolds-number bubbles in inhomogeneous flows.* Annual Review of Fluid Mechanics, 2000. 32(1): p. 659-708.
16. Batchelor, G. *An introduction to fluid dynamics. 1967.* Cambridge,: UP xviii, 1967. 615.
17. N. M. Aybers, A.T. *The motion of gas bubbles rising through stagnant liquid.* Heat and Substance Transfer, 1969. 2: p. 118-128.
18. Levich, V.G. *Physicochemical Hydrodynamics Prentice-Hall.* Englewood Cliffs, NJ, 1962. 115.
19. Kang, I., Leal, L. *The drag coefficient for a spherical bubble in a uniform streaming flow.* The Physics of fluids, 1988. 31(2): p. 233-237.
20. Moore, D. *The rise of a gas bubble in a viscous liquid.* Journal of Fluid Mechanics, 1959. 6(1): p. 113-130.
21. Moore, D. *The boundary layer on a spherical gas bubble.* Journal of Fluid Mechanics, 1963. 16(2): p. 161-176.
22. Moore, D. *The velocity of rise of distorted gas bubbles in a liquid of small viscosity.* Journal of Fluid Mechanics, 1965. 23(4): p. 749-766.
23. Duineveld, P. *The rise velocity and shape of bubbles in pure water at high Reynolds number.* Journal of Fluid Mechanics, 1995. 292: p. 325-332.
24. Maxworthy, T. et al. *Experiments on the rise of air bubbles in clean viscous liquids.* Journal of fluid mechanics, 1996. 321: p. 421-441.
25. Dijkhuizen, W. et al. *DNS of gas bubbles behaviour using an improved 3D front tracking model—Drag force on isolated bubbles and comparison with experiments.* Chemical Engineering Science, 2010. 65(4): p. 1415-1426.
26. Hartunian, R.A., Sears, W. *On the instability of small gas bubbles moving uniformly in various*

liquids. Journal of Fluid Mechanics, 1957. 3(1): p. 27-47.
27. Liu, L., Yan, H., Zhao, G. *Experimental studies on the shape and motion of air bubbles in viscous liquids.* Experimental Thermal and Fluid Science, 2015. 62: p. 109-121.
28. Ford, B., Loth, E. *Forces on ellipsoidal bubbles in a turbulent shear layer.* Physics of Fluids, 1998. 10(1): p. 178-188.
29. Hadamard, J. *Mouvement permanent lent d'une sphère liquid et visqueuse dans un liquide visqueux.* CR Hebd. Seances Acad. Sci. Paris, 1911. 152: p. 1735-1738.
30. Tomiyama, A. et al. *Terminal velocity of single bubbles in surface tension force dominant regime.* International journal of multiphase flow, 2002. 28(9): p. 1497-1519.
31. Zhang, Y., Finch, J. *A note on single bubble motion in surfactant solutions.* Journal of Fluid Mechanics, 2001. 429: p. 63-66.
32. Celata, G.P. et al. *Effect of gas injection mode and purity of liquid on bubble rising in two-component systems.* Experimental Thermal and Fluid Science, 2006. 31(1): p. 37-53.
33. Sakamoto, H., Haniu, H. *The formation mechanism and shedding frequency of vortices from a sphere in uniform shear flow.* Journal of Fluid Mechanics, 1995. 287: p. 151-171.
34. Rusche, H. *Computational fluid dynamics of dispersed two-phase flows at high phase fractions*. 2003, Imperial College London (University of London).
35. Lindt, J.T. *On the periodic nature of the drag on a rising bubble.* Chemical Engineering Science, 1972. 27(10): p. 1775-1781.
36. R. Clift, J.R.G., and M. E. Weber. *Bubbles, drops, and particles*. 1978. New York ; London. Academic Press.
37. Ngachin, M. *Simulation of rising bubbles dynamics using the lattice Boltzmann method*, in *Geosciences*. 2011, Florida International University.
38. Xu, X. et al. *Rising behavior of single bubble in infinite stagnant non-Newtonian liquids.* International Journal of Multiphase Flow, 2017. 95: p. 84-90.
39. Joshi, J.B. et al. *Bubble generated turbulence and direct numerical simulations.* Chemical Engineering Science, 2017. 157: p. 26-75.
40. Tripathi, M.K., Sahu, K.C., Govindarajan, R. *Dynamics of an initially spherical bubble rising in quiescent liquid.* Nature Communications, 2015. 6: p. 6268.
41. Joshi, J.B. et al. *Bubble generated turbulence and direct numerical simulations.* Chemical Engineering Science, 2017. 157: p. 26-75.
42. Brücker, C. *Structure and dynamics of the wake of bubbles and its relevance for bubble interaction.* Physics of Fluids, 1999. 11(7): p. 1781-1796.
43. Mougin, G., Magnaudet, J. *The generalized Kirchhoff equations and their application to the interaction between a rigid body and an arbitrary time-dependent viscous flow.* International Journal of Multiphase Flow, 2002. 28(11): p. 1837-1851.
44. Mikaelian, D. et al. *A new experimental method to analyze the dynamics and the morphology of bubbles in liquids: Application to single ellipsoidal bubbles.* Chemical Engineering Science, 2013. 100: p. 529-538.
45. Batchelor, G.K. *The stability of a large gas bubble rising through liquid.* Journal of Fluid Mechanics, 1987. 184: p. 399-422.
46. Veldhuis, C. *Leonardo's paradox: Path and shape instabilities of particles and bubbles.* 2007.
47. De Vries, J., Luther, S., Lohse, D. *Induced bubble shape oscillations and their impact on the rise velocity.* The European Physical Journal B-Condensed Matter and Complex Systems, 2002. 29(3): p. 503-509.
48. Mougin, G., Magnaudet, J.J.J.o.F.M. *Wake-induced forces and torques on a zigzagging/spiralling bubble.* Journal of Fluid Mechanics, 2006. 567: p. 185.
49. Cano-Lozano, J.C., Bohorquez, P., Martínez-Bazán, C. *Wake instability of a fixed axisymmetric bubble of realistic shape.* International Journal of Multiphase Flow, 2013. 51: p. 11-21.
50. Lain, S., Bröder, D., Sommerfeld, M. *Experimental and numerical studies of the hydrodynamics in*

a bubble column. Chemical Engineering Science, 1999. 54(21): p. 4913-4920.
51. Ellingsen, K., Risso, F. *On the rise of an ellipsoidal bubble in water: oscillatory paths and liquid-induced velocity.* Journal of Fluid Mechanics, 2001. 440: p. 235-268.
52. Babadagli, T., Boluk, Y. *Oil recovery performances of surfactant solutions by capillary imbibition.* Journal of colloid and interface science, 2005. 282(1): p. 162-175.
53. Wellek, R., Agrawal, A., Skelland, A. *Shape of liquid drops moving in liquid media.* AIChE Journal, 1966. 12(5): p. 854-862.
54. Magnaudet, J.J. *The forces acting on bubbles and rigid particles*. ASME Fluids Engineering Division Summer Meeting, FEDSM. 1997.
55. Lohse, D., Prosperetti, A. *Controlling bubbles.* Journal of physics: Condensed matter, 2002. 15(1): p. S415.
56. Shew, W.L., Poncet, S., Pinton, J.-F. *Force measurements on rising bubbles.* Journal of Fluid Mechanics, 2006. 569: p. 51-60.
57. Shew, W.L., Pinton, J.-F. *Dynamical model of bubble path instability.* Physical review letters, 2006. 97(14): p. 144508.
58. de Vries, A.W.G., Biesheuvel, A., van Wijngaarden, L. *Notes on the path and wake of a gas bubble rising in pure water.* International Journal of Multiphase Flow, 2002. 28(11): p. 1823-1835.
59. Sugioka, K.-i., Tsukada, T. *Direct numerical simulations of drag and lift forces acting on a spherical bubble near a plane wall.* International Journal of Multiphase Flow, 2015. 71: p. 32-37.
60. Lee, J., Park, H. *Wake structures behind an oscillating bubble rising close to a vertical wall.* International Journal of Multiphase Flow, 2017. 91: p. 225-242.
61. Jeong, H., Park, H. *Near-wall rising behaviour of a deformable bubble at high Reynolds number.* Journal of Fluid Mechanics, 2015. 771: p. 564.
62. Pelletier, E., Béguin, C., Étienne, S. *Experiments of air bubbles impacting a rigid wall in tap water.* Physics of Fluids, 2015. 27(12): p. 123302.
63. Masliyah, J., Jauhari, R., Gray, M. *Drag coefficients for air bubbles rising along an inclined surface.* Chemical engineering science, 1994. 49(12): p. 1905-1911.
64. Masliyah J. H., J., R., Gray M. R. *Rise velocities of air bubbles along an inclined surface*, in *Mixed-Flow Hydrodynamics*, N.P. Cheremisinoff, Editor. 1996, Gulf Publishing: Houston, Texas.
65. Drechsler, C. et al. *Bubble Behavior in Marine Applications of Bubble Columns: Case of Ellipsoidal Bubbles in Slanted and Rolling Columns.* Industrial & Engineering Chemistry Research, 2019. 58(6): p. 2343-2355.
66. Yamaguchi, T., Iguchi, M., Uemura, T. *Behavior of a small single bubble rising in a rotating flow field.* Experimental mechanics, 2004. 44(5): p. 533-540.
67. Li, Z. et al. *Experimental investigation of single small bubble motion in linear shear flow in water.* Nuclear Engineering and Design, 2016. 305: p. 334-346.
68. Legendre, D., Daniel, C., Guiraud, P. *Experimental study of a drop bouncing on a wall in a liquid.* Physics of Fluids, 2005. 17(9): p. 097105.
69. Van Nierop, E.A. et al. *Drag and lift forces on bubbles in a rotating flow.* Journal of fluid mechanics, 2007. 571: p. 439-454.
70. Rastello, M., Marié, J.-L., Lance, M. *Drag and lift forces on clean spherical and ellipsoidal bubbles in a solid-body rotating flow.* Journal of Fluid Mechanics, 2011. 682: p. 434-459.
71. Tomiyama, A. et al. *Transverse migration of single bubbles in simple shear flows.* Chemical Engineering Science, 2002. 57(11): p. 1849-1858.
72. Zahedi, P. et al. *Influence of fluid properties on bubble formation, detachment, rising and collapse; Investigation using volume of fluid method.* Korean Journal of Chemical Engineering, 2014. 31(8): p. 1349-1361.
73. Michaelides, E.E., Crowe, C. (Ed.), Schwarzkopf, J. (Ed.). *Multiphase Flow Handbook*. 2016. Boca Raton. CRC Press.
74. Laín, S. et al. *Modelling hydrodynamics and turbulence in a bubble column using the Euler–*

Lagrange procedure. International Journal of Multiphase Flow, 2002. 28(8): p. 1381-1407.
75. Delnoij, E. et al. *Dynamic simulation of dispersed gas-liquid two-phase flow using a discrete bubble model.* Chemical engineering science, 1997. 52(9): p. 1429-1458.
76. Delnoij, E., Kuipers, J.A.M., van Swaaij, W.P.M. *Dynamic simulation of gas-liquid two-phase flow: effect of column aspect ratio on the flow structure.* Chemical Engineering Science, 1997. 52(21): p. 3759-3772.
77. Lapin, A., Lübbert, A. *Numerical simulation of the dynamics of two-phase gas—liquid flows in bubble columns.* Chemical Engineering Science, 1994. 49(21): p. 3661-3674.
78. Sokolichin, A., Eigenberger, G. *Gas—liquid flow in bubble columns and loop reactors: Part I. Detailed modelling and numerical simulation.* Chemical Engineering Science, 1994. 49(24, Part 2): p. 5735-5746.
79. van Sint Annaland, M., Deen, N.G., Kuipers, J.A.M. *Numerical simulation of gas bubbles behaviour using a three-dimensional volume of fluid method.* Chemical Engineering Science, 2005. 60(11): p. 2999-3011.
80. Albadawi, A. *On the assessment of numerical interface capturing methods for two fluid flow applications*. 2014, Dublin City University.
81. Sankaranarayanan, K. et al. *Analysis of drag and virtual mass forces in bubbly suspensions using an implicit formulation of the lattice Boltzmann method.* Journal of Fluid Mechanics, 2002. 452: p. 61-96.
82. Delnoij, E., Kuipers, J.A.M., van Swaaij, W.P.M. *A three-dimensional CFD model for gas–liquid bubble columns.* Chemical Engineering Science, 1999. 54(13): p. 2217-2226.
83. Krishna, R. et al. *Rise velocity of a swarm of large gas bubbles in liquids.* Chemical Engineering Science, 1999. 54(2): p. 171-183.
84. Hassan, N.M.S., Khan, M.M.K., Rasul, M.G. *A modelling and experimental study of the bubble trajectory in a non-Newtonian crystal suspension.* Fluid Dynamics Research, 2010. 42(6): p. 065502.
85. Ma, D. et al. *Two-dimensional volume of fluid simulation studies on single bubble formation and dynamics in bubble columns.* Chemical Engineering Science, 2012. 72: p. 61-77.
86. Zhang, K. et al. *Computational Fluid Dynamics (CFD) Modeling of Bubble Dynamics in the Aluminum Smelting Process.* Industrial & Engineering Chemistry Research, 2013. 52(33): p. 11378-11390.
87. Tomiyama, A. et al. *Numerical analysis of bubble motion with the VOF method.* Nuclear Engineering and Design, 1993. 141(1): p. 69-82.
88. Xu, Y., Ersson, M., Jönsson, P. *Numerical Simulation of Single Argon Bubble Rising in Molten Metal Under a Laminar Flow.* steel research international, 2015. 86(11): p. 1289-1297.
89. Pourtousi, M. et al. *Methane bubble formation and dynamics in a rectangular bubble column: A CFD study.* Chemometrics and Intelligent Laboratory Systems, 2015. 147: p. 111-120.
90. Wang, G. et al. *The Motion of Single Bubble and Interactions between Two Bubbles in Liquid Steel.* ISIJ International, 2017. 57(5): p. 805-813.
91. Zhongchun, L. et al. *Numerical investigation on lateral migration and lift force of single bubble in simple shear flow in low viscosity fluid using volume of fluid method.* Nuclear Engineering and Design, 2014. 274: p. 154-163.
92. Wang, S. et al. *The dynamics of rising oil-coated bubbles: experiments and simulations.* Soft Matter, 2018. 14(14): p. 2724-2734.
93. Dijkhuizen, W. et al. *Numerical investigation of closures for interface forces acting on single air-bubbles in water using Volume of Fluid and Front Tracking models.* Chemical Engineering Science, 2005. 60(22): p. 6169-6175.
94. Cano-Lozano, J.C. et al. *The use of Volume of Fluid technique to analyze multiphase flows: Specific case of bubble rising in still liquids.* Applied Mathematical Modelling, 2015. 39(12): p. 3290-3305.
95. Anwar, S. *Lattice Boltzmann modeling of buoyant rise of single and multiple bubbles.* Computers

& Fluids, 2013. 88: p. 430-439.
96. Huang, H., Wang, L., Lu, X.-y. *Evaluation of three lattice Boltzmann models for multiphase flows in porous media.* Computers & Mathematics with Applications, 2011. 61(12): p. 3606-3617.
97. Zheng, H.W., Shu, C., Chew, Y.T. *A lattice Boltzmann model for multiphase flows with large density ratio.* Journal of Computational Physics, 2006. 218(1): p. 353-371.
98. morning, R.M.G.G.F.I.E.C.J.G. *Validation of a ghost fluid method in a tree-based adaptive volume of fluid for two-phase heat and mass transfer*, in *8th International Conference of Boiling and Condensation Heat Transfer*. 2012: Lausanne, Switzerland. p. 1-11.
99. Gumulya, M. et al. *Characteristics of energy production and dissipation around a bubble rising in water.* Chemical Engineering Science, 2019. 193: p. 38-52.
100. Gumulya, M. et al. *Interaction of bubbles rising inline in quiescent liquid.* Chemical Engineering Science, 2017. 166: p. 1-10.
101. Nichita, B.A., Zun, I., Thome, J.R. *A Level Set Method Coupled With a Volume of Fluid Method for Modeling of Gas-Liquid Interface in Bubbly Flow.* Journal of Fluids Engineering, 2010. 132(8): p. 081302-081302-15.
102. Brackbill, J.U., Kothe, D.B., Zemach, C. *A continuum method for modeling surface tension.* Journal of computational physics, 1992. 100(2): p. 335-354.
103. Abadie, T., Aubin, J., Legendre, D. *On the combined effects of surface tension force calculation and interface advection on spurious currents within Volume of Fluid and Level Set frameworks.* Journal of Computational Physics, 2015. 297: p. 611-636.
104. Popinet, S. *Numerical models of surface tension.* Annual Review of Fluid Mechanics, 2018. 50: p. 49-75.
105. Lafaurie, B. et al. *Modelling merging and fragmentation in multiphase flows with SURFER.* Journal of Computational Physics, 1994. 113(1): p. 134-147.
106. Samkhaniani, N., Ansari, M. *Numerical simulation of bubble condensation using CF-VOF*. Progress in Nuclear Energy, 2016. 89: p. 120-131.
107. Vachaparambil, K.J., Einarsrud, K.E. *Comparison of Surface Tension Models for the Volume of Fluid Method.* Processes, 2019. 7(8): p. 542.
108. Raeini, A.Q., Blunt, M.J., Bijeljic, B. *Modelling two-phase flow in porous media at the pore scale using the volume-of-fluid method.* Journal of Computational Physics, 2012. 231(17): p. 5653-5668.
109. Pavuluri, S., Maes, J., Doster, F. *Spontaneous imbibition in a microchannel: Analytical solution and assessment of volume of fluid formulations.* Microfluidics and Nanofluidics, 2018. 22(8): p. 90.
110. Abadie, T. *Hydrodynamics of gas-liquid Taylor flow in microchannels*. 2013, PhD Thesis, Universite de Toulouse.
111. Zalesak, S.T. *Fully multidimensional flux-corrected transport algorithms for fluids.* Journal of computational physics, 1979. 31(3): p. 335-362.
112. Ruen-ngam, D. et al. *Influence of salinity on bubble size distribution and gas–liquid mass transfer in airlift contactors.* Chemical Engineering Journal, 2008. 141(1): p. 222-232.
113. Koebe, D.-I.M. *Numerische Simulation aufsteigender Blasen mit und ohne Stoffaustausch mittels der Volume of Fluid (VOF) Methode.* 2004.
114. Rabha, S.S., Buwa, V.V. *Volume-of-fluid (VOF) simulations of rise of single/multiple bubbles in sheared liquids.* Chemical Engineering Science, 2010. 65(1): p. 527-537.
115. Inc., A.F. *ANSYS Fluent 12.0 User's Guide*. 2009.
116. Atta, A. et al. *Co-current descending two-phase flows in inclined packed beds: experiments versus simulations.* The Canadian Journal of Chemical Engineering, 2010. 88(5): p. 742-750.
117. Motamed Dashliborun, A., Larachi, F. *CFD study and experimental validation of multiphase packed bed hydrodynamics in the context of Rolling Sea conditions.* AIChE Journal, 2019. 65(1): p. 385-397.

2. Chapter 2:

Three-dimensional analysis of the rising dynamics of individual ellipsoidal bubbles in an inclined column

Nasim Heydari, Faical Larachi, Seyed Mohammad Taghavi, Francois Bertrand
Published in Chemical Engineering Science, v258 (20220831), 2022.

2.1. Résumé

Dans cette étude, la dynamique d'une seule bulle d'air ellipsoïdale s'élevant dans un récipient cylindrique incliné est étudiée expérimentalement. La reconstruction tridimensionnelle de la trajectoire de la bulle montre que la bulle montante en spirale maintient deux modes d'oscillations déphasés, tandis que la bulle en zigzag maintient un mouvement bidimensionnel malgré les rebonds irréguliers de faible amplitude. L'évaluation des rebonds paroi-bulle pour la bulle ascendante hélicoïdale montre que le coefficient de restitution normal est corrélé à un nombre de Stokes normal modifié de la même manière que les collisions paroi normale des gouttelettes de liquide [Legendre et al., 2005, Physics of Fluids 17, 097105]. La contribution similaire des composantes normale à la paroi et tangente à la paroi de l'énergie cinétique dans la montée hélicoïdale de la bulle est maintenue jusqu'à l'angle d'inclinaison le plus élevé, c'est-à-dire 15º. Cependant, pour la bulle montante en zigzag, malgré les rebonds de la bulle sur la paroi, la contribution normale à la paroi de l'énergie cinétique est bien inférieure à sa composante tangente à la paroi.

2.2. Abstract

In this study, the dynamics of a single ellipsoidal air bubble rising in an inclined cylindrical vessel is experimentally investigated. The three-dimensional bubble trajectory reconstruction shows that the spirally rising bubble maintains two out-of-phase modes of oscillations, while the zigzagging bubble maintains a two-dimensional motion despite the irregular rebounds with small amplitude. Assessing the bubble-wall rebounds for the helicoidal rising bubble shows that the normal restitution coefficient correlates with a modified normal Stokes number in the same manner as the normal wall collisions of liquid droplets [Legendre et al., 2005, Physics of Fluids 17, 097105]. A similar contribution of normal-to-wall and tangent-to-wall components of the kinetic energy in helicoidal bubble rise is maintained up to the highest inclination angle, i.e. 15º. However, for the zigzag rising bubble, despite the bubble rebounds on the wall, the wall-normal contribution of the kinetic energy is much less than its tangent-to-wall component.

2.3. Introduction

Bubble columns are a category of multiphase reactors, in which a gas phase is sparged dispersedly into a continuous liquid phase. Although wholistic approaches to understand these multi-bubble systems pervade in the literature [1], pleas for reductionist approaches focusing on the study of single rising bubbles have also been privileged to probe the space- and time-resolved fundamental phenomena of gas-liquid flows [1, 2]. It is indeed conjectured that since changes in the behavior of individual bubbles influence multiple-bubble systems, knowledge of the dynamics of a single rising bubble is prerequisite to understanding bubble columns [3]. The phenomena occurring in the single-bubble case are nevertheless no less complex, as a result of a large number of parameters, non-linearity, highly contrasted physical properties of the two fluids [4], and often three-dimensional (transient) dynamics [5].

Two dimensionless numbers, namely, the Reynolds ($Re = \frac{\rho_l d_e v}{\mu_l}$) and Weber numbers ($We = \frac{\rho_l d_e v^2}{\sigma}$), are customarily defined, aided with related auxiliary (Morton, Eötvös and Galilei) numbers, to characterize the rise of a bubble in fluids [6]. In typical conditions, small bubbles (d_{eq} < 1.3 mm) are approximately spherical as interfacial tension and viscous forces dominate inertia, and their trajectory is rectilinear. Bubbles with diameters ranging from 1.3 to 50 mm change to an ellipsoidal shape and commonly exhibit oscillatory trajectories [4, 7, 8]. A taxonomy of air bubble trajectories in still water by Aybers and Tapucu [8] recognizes five types of motion, including rectilinear, helical, plane zigzag then helical, plane zigzag, and rectilinear with rocking motion. It is well established that the onset of *path* instability coincides with *wake* instability [9-14]. However, the existence of standing eddy at the bubble rear is not a necessary condition for the onset of path instability [15]. Although the bubble rising characteristics mainly depend on the bubble diameter, aspect ratio and relative dominance among inertia, viscosity, and surface tension [6, 16, 17], they also depend on other mechanisms, e.g., the presence of liquid contaminants, coupling between path and shape oscillations, and initial conditions of bubble release [4, 17-19], not to also mention the influence of geometrical disturbances generated by bubble-wall interactions.

The effect of the gas injection method on the bubble rising characteristics is not to be underestimated [17-19]. Tomiyama et al. [17] suggested that the motion regime proposed by

Aybers and Tapucu [8] is mainly the outcome of their bubble injection method. For instance, if a small initial shape deformation delays the transition from primary (zigzag) to secondary (helical) unstable mode, large initial shape deformation increases, on the contrary, the growth rate of the secondary unstable mode [4, 17, 18]. When a released bubble undergoes large initial shape deformation, it starts its motion with a larger surface free energy contrary to small initial shape deformation. Hence, the latter embodies a zigzag motion reminiscent of a low rise velocity, while, in contrast, the former prompts a helical motion caused by a high axial velocity [17, 19].

This study focuses on the rising dynamics of bubbles in an inclined column due to the importance of bubble-wall interactions on the bubble flow characteristics, such as void fraction and bubble size distribution. Most of the previous investigations on bubble-wall interactions were limited to vertical [20-26] or horizontal [27-31] walls. In contrast, studies on bubble rising beneath an inclined wall were limited to a few ones [32-38]. Several works were devoted to the determination of the hydrodynamic forces acting on a solid [39, 40] or a fluid particle (including spherical or deformed shape) [22-25], moving near a solid wall in the low [23, 41], moderate [22, 25] and high [24] Reynolds-number regimes. Most of the studies used the technique of asymptotic expansions of different forces acting on the particle, with respect to the distance between the wall and the particle center of mass. It has been well established that, for a spherical particle rising parallel to a wall at finite Reynolds numbers, the velocity field induced by the vorticity distribution around the bubble results in a wall-repulsive transverse force. On the other hand, a wall-attractive transverse force is induced by the acceleration of the flow in the gap between wall and the particle (inviscid irrotational theory) [42]. As the Reynolds number increases, the irrotational mechanism dominates; thus, the force between the bubble and the vertical wall changes from repulsive to attractive [22].

For horizontal walls, Zenit and Legendre [28] analyzed the conditions for rebound and arrest of air bubbles, for which they proposed an empirical criterion using a modified Stokes number and the Capillary number. For vertical walls, Jeong and Park [21] performed a study on the effect of wall surface properties on the bubble rising behavior close to the wall at high Reynolds numbers ($Re \approx O(1000)$). Various rising behaviors were analyzed for different wall surfaces and initial wall distances. They showed that the boundary condition of the wall surface is crucial in energy

dissipation during the bubble-wall collision. The wall effect (or energy loss) decreases as the initial bubble-wall distance increases. In the case of a bubble interacting with an inclined wall, the bubble motion can be either of repeating bouncing or sliding, depending on the inclination angle [32, 35]. Barbosa et al. [35] explained that, depending on the strength of inertial forces, a wall-induced lift force emerges and pushes the bubble away from the inclined wall. Recently, Barbosa et al. [38] experimentally analyzed both bubble shape and drag coefficient for bubbles rising beneath inclined walls. However, their experiments were limited to the sliding regime that occurs below the transition to steady bouncing.

To characterize the collision-rebound process of particles, the concept of restitution coefficient has been followed in several studies. This coefficient characterizes the energy dissipation during the contact of a particle with a surface. For a solid particle colliding against a vertical wall immersed in a viscous liquid, Joseph et al. [43] demonstrated that the restitution coefficient depends on the particle Stokes number, which compares the particle inertia to viscous effects. This concept was extended to droplets [27, 44] by introducing into a modified Stokes number, both fluid and particle inertia, to account for the added-mass contribution in bubble deformations. For ellipsoidal bubbles colliding with a horizontal wall, Zenit and Legendre [28] developed a different scaling of the restitution coefficient using the Capillary and modified Stokes numbers.

To investigate the wall effect on droplet dynamics, Klaseboer et al. [31] proposed a model for the rebound of a drop impacting on a horizontal plate. The model is based on the force balance over the droplet, where the force exerted by the wall was computed using the lubrication theory. The model provided correct amplitudes and periods for the bounces of drops at high Reynolds and moderate Weber numbers. Manica et al. [30] and Podvin et al. [34] then employed the same approach to model the bubble-wall interactions with, respectively, horizontal and inclined walls. While the model developed by [30] considered bubble deformations, the other approach [34] was able to reproduce the bubble trajectory for wall inclinations up to 55º-60º (from horizontal), including the rebound amplitude of the bubble and its time scale.

The great majority of studies on bubble-wall interactions were devoted to bubbles with rectilinear rising trajectories. Only a very limited number of studies considered bubbles with path and shape instabilities, i.e. with reference to wall-free rising zigzag or spiral paths. Pelletier

et al. [29] investigated the air bubble collision with a horizontal wall in tap water for fast and slow bubbles, exhibiting both zigzag and helical trajectories. They showed that the normal restitution coefficient for the fast bubbles with oscillatory motion follows the same functional dependence based on a modified Stokes number, as proposed by Zenit and Legendre [28] for rectilinear bubble motions. Jeong and Park [21] studied bubble-wall interactions for large deformable bubbles ($Re \approx O(1000)$), for which the free-rising bubble trajectory was zigzag. Different bubble path variations (i.e. sliding, periodic rebounding, migrating away, and non-periodic oscillation without collisions) were shown to depend on the initial bubble-wall distance and wall properties. Lee and Park [26] investigated the wall-induced wake modifications for an oscillating two-dimensional motion of an air bubble rising in close vicinity of a vertical wall. They showed that the streamwise vortex tubes attached to the bubble rear tended to move away from the wall as the bubble collides with the wall.

Despite intensive investigations on the bubble-wall interactions, knowledge of the wall induced alternations in the rising dynamics is limited to the case of rectilinearly rising bubble. For the majority of studies, the bubble was spherical, and the Reynolds and Weber numbers were small to moderate. The few studies in the case of bubbles with path instabilities, i.e., the reference (wall-free) rising path is two-dimensional zigzag or three-dimensional spiral, have focused on the bubble-wall interaction with a horizontal or vertical wall. Thus, whether variations of the dynamics and kinematics occur for a rising bubble in an inclined column at high Reynolds and moderate to high Weber numbers remain to be addressed. We specially consider the rise of bubbles with shape and path instabilities. In addition, previous studies considering the wall impact for the case of bubbles with path instabilities were limited to two-dimensional motions. Hence, the three-dimensional analysis of the wall-induced path variation for a helically rising bubble can provide new insights to describe the gas-void fraction distribution, in inclined vessels and near-wall gas-liquid flows. The result of this study can be extended to a wide range of applications, especially in gas-liquid contactors/reactors, as the range of inclination angles are selected close to the vertical. Accordingly, the present study is intended to experimentally measure the shape and path variations of bubbles rising in a cylindrical column, tilted down to 15° from vertical, while analyzing the deviations with respect to wall-unobstructed rectilinear, zigzag and helicoidal free rising bubbles. The liquid phase (Morton numbers,

Mo: $10^{-7}, 10^{-9}, 10^{-11}$), and the bubble size ($d_{\mathrm{eq}} = 2.8 - 3.34$ mm) are selected to correspond to different path instability regimes. Additionally, the rebound characteristics of the bubbles while rising along the wall of the column is investigated in terms of the restitution coefficient and surface, and three-dimensional kinetic energy variations.

2.4. Experimental Setup

The experimental setup is schematically shown in Figure 2.1a, b. The experiments were performed in a vertical transparent Plexiglas cylindrical column of 800 mm height with an internal diameter of 57 mm. A stainless-steel capillary tube (internal diameter = 1 mm) was placed on the column centreline. The experiments were performed using three different glycerol-water mixtures/water the properties of which are listed in Table 2.2. The column was filled with water/glycerol solutions to a height of 600 mm above the orifice tip where the bubbles were generated using a pinch-off method [18]. Sufficient time intervals were allowed to prevent interaction between two successive bubbles (minimum 2^{+} s). For all experiments, the trajectory analysis was made after bubbles had reached their terminal conditions. The experiments were performed for different inclination angles from 0° to 15° form vertical.

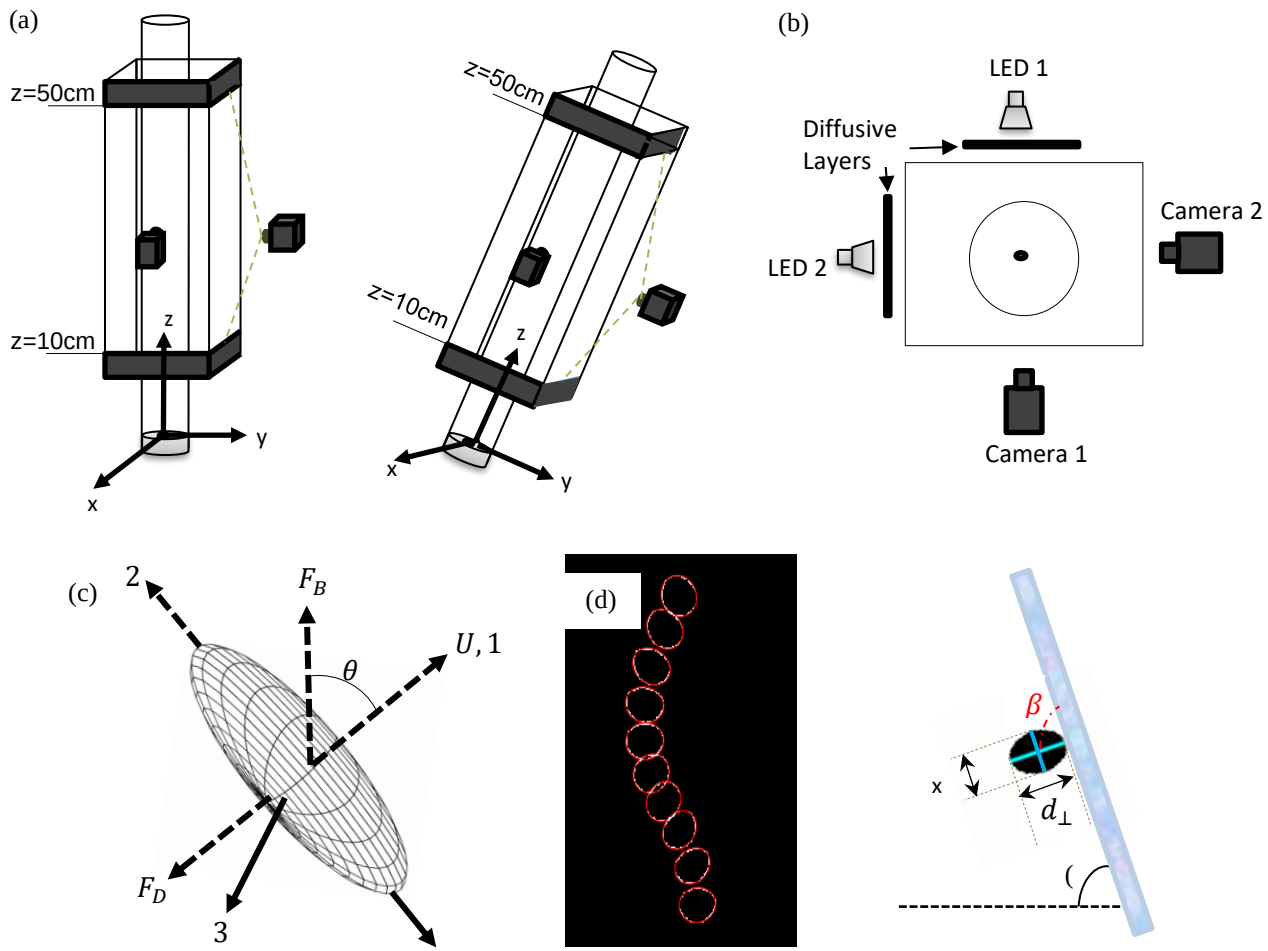

Figure 2.1. Experimental setup, (a) side view, (b) top view, (c) diagram of the coordinate system arrangement (1,2,3) which rotates with the bubble (1 is in the direction of the bubble velocity vector), (d) detected contour and fitted ellipsoid for ten subsequent frames, (e) sketch of sliding bubble and wall aspect ratio ($x_{wall} = \frac{d_\parallel}{d_\perp}$).

Images of bubbles were captured and recorded by means of two BASLER acA2040-180um high-speed video cameras able to work at a rate of 90 frames per second. Diffusive layers were installed around the column for scattering of light beams from LED (light-emitting diode) sources. The column was immersed in a Plexiglas rectangular box filled with distilled water to reduce optical distortions by the curved column wall and differences between the refractive indices of the fluids and column material. Two different resolutions were used for providing accurate descriptions of the bubble shape and bubble rising trajectory. For the bubble shape investigation, a high resolution (pixel size of 0.085 mm) was achieved using a small window. For the trajectory investigation, a

larger window provided a resolution with a pixel size of 0.23 mm. As illustrated in Figure 2.1a, the original images were captured by the camera rotated in such a way that the coordinate system *z* axis is along the wall, while the column is inclined in the *y* direction.

Table 2.1. Resolution details.

Set of experiment	Window size (mm^2)	Pixel size (mm)
Shape tests	100*57	0.085
Trajectory tests	300*57	0.23

To construct the three-dimensional trajectory of bubbles, images were captured and recorded simultaneously using two cameras, working at a frame rate of 90 frames per second. Images of the bubble onto the planes (*x, z*) and (*y, z*) were captured while using the two cameras installed perpendicularly (Figure 2.1a, b). LED sources were installed on the opposite side, facing each camera. The projection error was reduced to less than 0.1%, by calibrating the captured images. The algorithm for calculating the three-dimensional data was developed in MATLAB, in which the intersection of the two projection lines reaching the two image planes from the camera's focal points were extracted.

High resolution images were used to track the bubble interface detected using image-processing algorithms developed in MATLAB. Figure 2.1d shows the detected interface compared with an exact ellipsoid for one image and for ten subsequent images. For each frame, the bubble aspect ratio is measured. For the bubble with rectilinear path, one camera was used to capture the bubble shape. However, for two and three-dimensional bubble motions, two cameras were used to provide images from the two sides (Figure 2.1b).

2.5. Experimental Uncertainties

The uncertainty associated with measuring bubble diameter is due to two contributions. The first error contribution arises in detecting the bubble edge. Based on the images captured, the maximum error in determining the bubble edge is ±1 pixel. Hence, for a bubble with an equivalent diameter larger than 2.5 mm, and a spatial resolution of 0.085 mm/pixel, the maximum error is ± 3.4 %. The

second error contribution arises in the calculation of the equivalent diameter by assuming that the bubble shape is symmetric. For this latter source, it is for water that the maximum error occurs because the bubble evolves close to the wobbling regime, unlike the rigid ellipsoidal shape in the glycerol solutions. The uncertainty of the bubble shape is evaluated by considering for each bubble, the root mean square of the aspect ratio along the observed bubble path. Hence, bubble oscillations and non-axisymmetric characteristics due to the zigzagging, helical motion or surface wobbling, as well as the error in detecting the bubble edge are all considered in this study. The maximum error is estimated to be less than 3 % according to our analyses.

Furthermore, the uncertainty associated with velocity measurements was checked using a video camera with a recording frame rate of 180 fps. The maximum speed of bubbles, nearly 330 $mm \cdot s^{-1}$, is close to other experimental measurements [8, 18]. The bubble position is extracted from images using MATLAB image processing routines. The accuracy of position measurements is about 6.8 % or ± 0.23 mm with 11 ms time resolution. The vertical position data are differentiated to obtain axial velocities within ± 10 $mm \cdot s^{-1}$ error.

2.6. Results and Discussions

Using water and water-glycerol solutions, different types of bubble motions in a quiescent liquid phase are analyzed, for reaching a full description of bubble behavior in the inclined column. The corresponding dimensionless numbers of the bubbles in the three tested liquids are listed in Table 2.2. Based on their Mo, Eo, and Re, the classification provided by the Grace diagram [45] predicts that all three instances correspond to ellipsoidal bubbles (Figure 2.2a). The bubble rise in water ($Eo = 1.5, Mo = 10^{-11}$) falls in the wobbling regime. A first increase of liquid viscosity (40 wt.% glycerol, $Eo = 1.67, Mo = 10^{-9}$) led to an ellipsoidal regime in which the rising bubble experiences shape oscillations due to wake instabilities. Shape oscillations ceased with a further viscosity increase (60 wt.% glycerol, $Eo = 1.4, Mo = 10^{-7}$) leading to a stable ellipsoidal shape. Bubble aspect ratio for the three sets of experiments is shown in Table 2.2. Comparing the aspect ratio with the model proposed by Moore [46] shows similar evolution of the aspect ratio with the Weber number with 5.5 %, 6.9 % and 1.4 % deviations for the rising bubble in 60 wt.% glycerol solution, 40 wt.% glycerol solution and water, respectively.

Table 2.2. Dimensionless numbers of bubbles.

Dimensionless numbers	Definition	60 wt.% glycerol $d_e = 2.87$ mm	40 wt.% glycerol $d_e = 3.22$ mm	Water $d_e = 3.34$ mm
Re	$Re = \frac{\rho_l d_e v}{\mu_l}$	69	250	843
We	$We = \frac{\rho_l d_e v^2}{\sigma}$	1.7	2.6	2.9
Log (Mo)	$Mo = \frac{g\mu_l^4}{\rho_l \sigma^3}$	-6.7	-8.5	-10.6
Eo	$Bo, Eo = \frac{\rho_l g d_e^2}{\sigma}$	1.4	1.67	1.5
Ga	$Ga = \frac{\rho_l \sqrt{g d_e} d_e}{\mu_l}$	63	201	603
x	$x = \frac{d_{major}}{d_{minor}}$	1.17	1.27	1.4

Considering the range of experimental conditions of Table 2.2, three regimes of free-rising bubble trajectories were observed, i.e., rectilinear, zigzag and helical. It is well established that the onset of path instability coincides with the wake instability [9-13]., and the maximum vorticity generated at the body surface, is the factor which determines the instability [12-14]. On the other hand, taking into account that bubbles with the same aspect ratio can exhibit different fore-and aft asymmetries, Cano-Lozano et al. [15] suggested that the existence of wakes past rising bubbles is not a necessary condition for the onset of path instability.

Figure 2.2b is the $Ga - Bo$ map proposed by Cano-Lozano et al. [47], which delineates the onset of standing eddy formations behind the real-shaped bubbles. Three symbols in the map shows the three sets of experiments provided in Table 2.2.

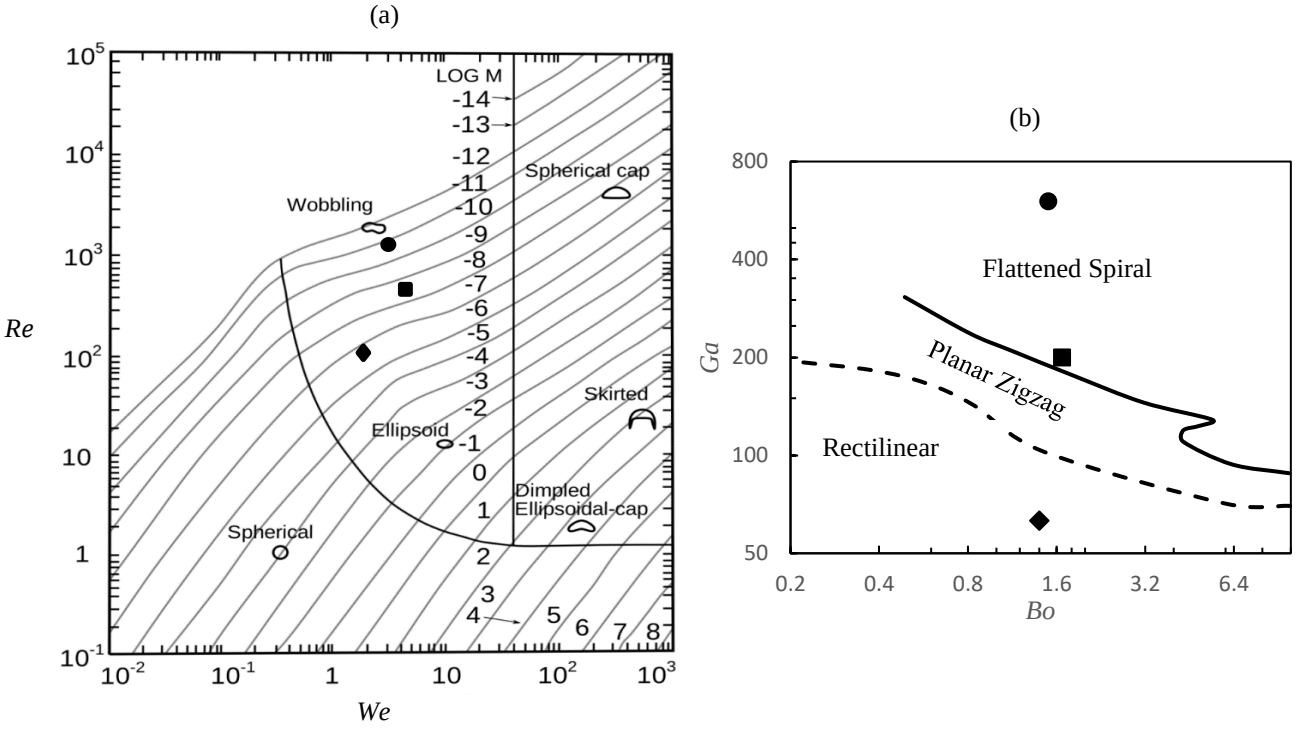

Figure 2.2. (a) Grace classification [45], (b) phase diagram proposed by Cano Lozano et al. [47] for different styles of bubble trajectory. The symbols correspond to different liquid phase as circle: water, square: 40 wt.% glycerol, diamond: 60 wt.% glycerol (sets of experiments provided in Table 2.2).

This section analyzes the rise of a single bubble, after it has reached its terminal state, inside a liquid-filled inclined cylindrical column. Notwithstanding that early works have focused on the bubble hydrodynamics in inclined vessels, the fact remains that wall effects combined with path instability leads to more complexities that deserve a detailed description of the bubble trajectory, velocity, shape and energy.

For the bubble rising along the inclined wall, the buoyancy force, which pushes the bubble to remain in contact with the wall, balances the lift force induced by the interaction of the bubble wake with the wall and acting normal to the wall [11]. The strength of the lift force depends on the strength of the circulation of the vortices and is proportional to $\rho\, v_{\text{wall}}^2\, d_{\text{eq}}^2$ [11], where v_{wall} is the bubble velocity parallel to wall. While the viscous and/or inertial drag and buoyancy forces are parallel to the wall direction, the motion normal to the wall can be achieved from balancing buoyancy with the wake-induced lift force. When the bubble migrates towards the wall, various rising behaviors including bouncing and sliding are possible, which are affected by the wake

behind the bubble [11], and the bubble-wall contact duration [21]. The three sets of experiments in this investigation fitted well with the sliding/bouncing criteria proposed by Barbosa et al. [35] for small and large values of We_{wall} (where We_{wall} is the Weber number calculated based on the bubble velocity parallel to wall). Figure 2.3 shows the results in terms of Re_{wall} as a function of $\cot\theta$ comparing the transition conditions (where Re_{wall} is the Reynolds number calculated based on the bubble velocity parallel to wall).

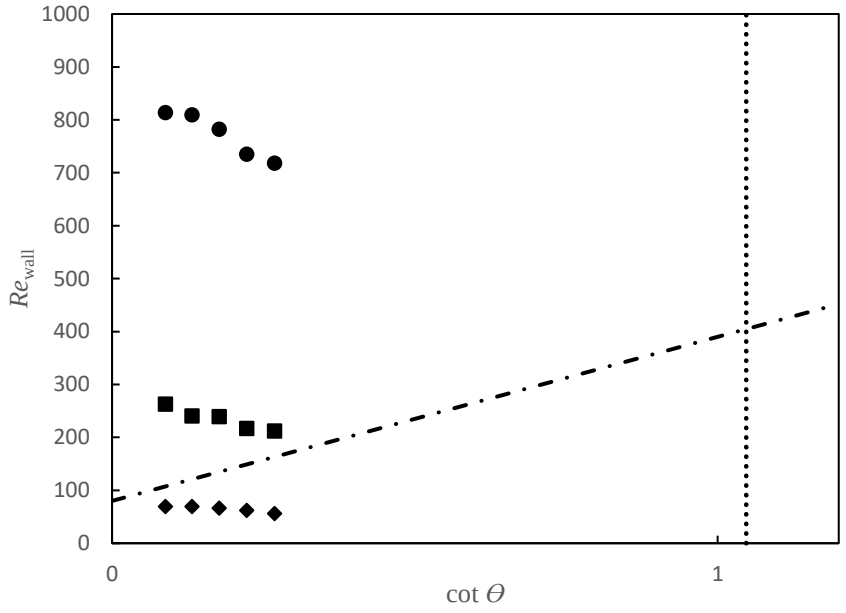

Figure 2.3. The three cases of experiments are shown comparing the two lines correspond to the transition criteria proposed by Barbosa et al. [35] for $We_{\text{wall}} < 1.2$: dashed dotted, and for $We_{\text{wall}} > 1.5$: dotted, respectively. Circle symbols correspond to the experiments using water, square symbols correspond to 40 wt.% glycerol and diamond symbols correspond to 60 wt.% glycerol.

Among the above experiments, for the case of a bubble rising in 40 wt.% glycerol and the 15º inclined column, the amplitude of the rebounds is very small. This resulted in high uncertainties for calculating the bouncing amplitude and the lateral velocity in this case.

2.6.1. Sliding Bubbles

For the free bubble with equivalent diameter of $d_{\text{eq}} = 2.87$ mm (Table 2.2) rising in the 60 wt.% glycerol solution ($Bo = 1.4$ and $Ga = 63$, diamond symbol Figure 2.2b), there is no standing eddy at the bubble rear [47], resulting in the rectilinear bubble trajectory. Terminal velocity conditions

in the vertical column are reached after a lapse of time, highlighting the balance of buoyancy and drag forces for a bubble subdued to a stable ellipsoidal shape. When the bubble rises in the inclined column, it ends up coming into contact with the wall before it starts sliding beneath it. In this case, not only is the upward buoyancy force counteracted by the drag force, but also, while the bubble is sliding along the wall, the flattening of its interface generates an additional resistance to the bubble rising motion. The bubble aspect ratio ($x = \frac{d_{\text{major}}}{d_{\text{minor}}}$) decreases as a result of bubble interface deformation in the vicinity of the wall, which commands the bubble to retain a more spherical shape. Bubbles with $Bo < We$ are stretched perpendicularly to the wall [36], as hydrodynamic pressure is overpassing buoyancy. The deformation of a bubble interacting with the wall is compared with the model proposed by Barbosa et al. [38]:

$$x_{\text{wall}} = \frac{(1-\beta\, We_{\text{wall}})}{(1-\alpha\, Bo\cos\theta)\left(1+\frac{\beta}{2}We_{\text{wall}}\right)} \tag{2.1}$$

X_w is the wall aspect ratio defined as $x_{\text{wall}} = \frac{d_{\parallel}}{d_{\perp}}$ (Figure 2.1e). The experimentally observed wall aspect ratios, 0.87 and 0.89 for the 10° and 15° inclined columns were well predicted using Eq.1 ($\alpha = 0.1$ and $\beta = 3/32$) with 4.23 % and 1.30 % deviations, respectively. The parameter value $\alpha = 0.1$, has been determined from a minimum least-squares fit scheme of the data *vs.* prediction, and the parameter value $\beta = 3/32$, according to [38], has been obtained by balancing the pressure distribution (from the irrotational flow around the bubble) with the surface tension force. When the bubble is deformed due to the inertia of the flow, the wall aspect ratio is smaller than one ($x_{\text{wall}} < 1$) and the bubble shape is rather similar to a freely rising bubble. However, according to a study by Dubois et al. [36] on the comparative dominance of inertia and viscous effects over the $Re = 0.01 - 400$ range, the viscous force is also relevant even at high Reynolds numbers. Using Newton's second law of motion for the bubble, the buoyancy force is balanced by the sum of the dynamic meniscus and inertial drag forces:

$$\rho g V \sin\theta \sim a\sigma L\, Ca_{\text{wall}}^{\frac{2}{3}} + \frac{1}{2}\, C_{\text{D}}\, \rho v^2 \pi R_0^2 \tag{2.2}$$

For the bubble sliding regime in 10° and 15° tilted columns, the drag coefficient for the inertial drag force, F_{Inertial}, is expressed as $C_{\text{D}} = \frac{\alpha}{Re} + \beta$ employing similar constants ($\alpha = 9$ and $\beta =$

0.65) as [36], whereas the characteristic capillary length, $l_c = \sqrt{\frac{\sigma}{\rho g}}$, and the contact length $L = \sqrt{\frac{2}{3}}\frac{R_0^{3/2}}{l_c^{1/2}}$ are needed in the dynamics meniscus force, F_{Meniscus}, in Eq. 2.

For small column tilt angles, the bubble-wall contact area is very small, as is equally negligible the contribution of the film drag [38]. Therefore, in the inertia dominated regime, the drag coefficient boils down to a constant. Conversely, in the viscous-dominated regime, the additional vorticity produced on the bubble surface because of the wall presence, and the film frictional viscous force, induce an increased drag force [38]. While based on the classification proposed by Barbosa et al. [38], the drag coefficient is influenced by the shape that the bubble adopts as it slides over the wall, and the inertia effects expected to be dominant but, as discussed above, the viscous effects play an important role in the drag experienced by the bubble as well. Barbosa et al. [38] considered the effect of one wall and superposed the mirror effect, using the model suggested by Figueroa-Espinoza et al. [48] for the additional drag due to vorticity production for a bubble moving between two walls, and proposed Eq. 3 for the drag coefficient of bubbles rising in a regime dominated by viscous effects for which the wall aspect ratio was $x_{\text{wall}} > 1$:

$$C_{\text{dwall}} = \frac{48}{Re_{\text{Wall}}}(1 + 4s^3 + F(Re_{\text{Wall}})) \tag{2.3}$$

where,

$$F(Re) = -\frac{2.211Re^{1/2}+32/3}{Re+3.315Re^{1/2}+16} \tag{2.4}$$

In Eq.3, s^3 accounts for the mirror effect and the additional vorticity production. The deviations between the model (considering a value of s = 0.53, where $s = \frac{d_{\text{eq}}}{l}$, l being the distance between the bubble center and the wall) and experimental data are 22 % and 28 % for the bubbles rising in the 10° and 15° tilted columns, respectively. Correspondingly, experimental data of drag coefficients (1.33 and 1.59) are larger than the model-predicted values, namely, 1.04, 1.13, respectively. Hence, the effect of the film between the bubble and the wall was added to the total drag in Eq. 5 [38]:

$$C_{\text{dwall}} = \frac{48}{Re_{\text{Wall}}}\left(1 + s^3 + F(Re_{\text{Wall}}) + K_0\frac{(Bo\ \cos(\theta)^n)}{Ca_{\text{wall}}^{1/3}}\right) \tag{2.5}$$

Considering $K_0 = 0.15$ and $n = 0.5$, which agrees well with the experimental data, the prediction gives a good estimate of the wall drag, although for the bubble studied here $x_{\text{wall}} < 1$. A value of the fitting coefficient K_0 equal to 0.15 agrees well with the experimental measurements, i.e., 1.33, 1.59 for the air bubbles rising in the 10° and 15° inclined columns, respectively. Note that this parameter shows the relative importance of the viscous film term [38]. The deviations between the model (Eq. 5) and experimental data are 2.4 % and 5.9 % for the 10° and 15° tilted columns, respectively. This confirms the above-mentioned contribution of both viscous and inertia effects in the drag experienced by the bubble as it was concluded by following the model proposed by Dubois et al. [36]. A worth-reminding fact is that the classification suggested by Barbosa et al. [38] for the prediction of drag coefficient based on x_{wall} was reported for the range of Reynolds number between 138 to 955. As shown in Table 2.2, the Reynolds number for the bubble rising in 60 wt.% glycerol is 69. This clarifies the reason for the different experimental drag coefficient with the model presented in Eq. 3 for the range of aspect ratio $x_{\text{wall}} < 1$.

2.6.2. Bouncing Bubbles

2.6.2.1. Reconstructed Trajectories

In this section, two cases of bubbles rising in 40 wt.% glycerol and water (Table 2.2) are investigated. The three-dimensional bubble paths, constructed using the algorithm developed in MATLAB, are illustrated in Figures 2.4 and 2.6 (black solid lines) together with their two-dimensional projected traces (gray solid lines) on the $x - z$, $y - z$, and $x - y$ planes for selected inclined columns filled with 40 wt.% glycerol and water, respectively.

Based on Figure 2.2 regime map, a 3.22 mm air bubble rising in the 40 wt.% glycerol ($Re = 250, Mo = 10^{-7}$) features both path and shape oscillations. For the 3.22 mm bubble ($Bo = 1.67$, $Ga = 201$, square symbol Figure 2.2b), rising in 40 wt.% glycerol, standing eddies form behind the bubble changing the bubble trajectory into a planar zigzag path. During each period of the zigzag movement, two counter-rotating vortices form, fade and reverse twice in direction [9, 47].

The reference rising path (bubble trajectory in vertical column) is zigzag and whereby path oscillations have angular frequency equal to 39 rd·s^{-1}. The effect of column tilt on bubble

trajectory is analyzed over the 0º to 15º range. Figures 2.4a shows the bubble trajectory in 40 wt.% glycerol for three selected inclination angles. The plane carrying the bubble trajectory is clearly different when it comes to compare the bubble trajectories at 0° (vertical or reference case, see Figure 2.4a/left) and at 7° (see Figure 2.4a/middle) or 10° (see Figure 2.4a/right) inclinations. The 0° *planar* trajectory, being offset with respect to the (*x*,*y*,*z*) coordinate system, showcases oscillating traces −continuous gray line projections− both on the *yz* and *xz* planes (Figure 2.4a/left). On the contrary, while the bubble approaches the wall in the tilted column, the plane of oscillations is in line with the direction of inclination (*y* direction). Matter-of-factly, one can see that the (continuous gray line projection) oscillating trace on the *yz* plane at 7° (see Figure 2.4a/middle) or 10° (see Figure 2.4a/right) is severely damped. Such damping originates when the bubble meets the wall. When it contacts the wall, the plane of path oscillation is modified by the wall. Close examination of the *yz* projection at 7° (see Figure 2.4a/middle) or 10° (see Figure 2.4a/right) shows slight indentations reminiscent of secondary oscillations. Apart from the main bubble path oscillation as exemplified in the oscillating traces within the *xz* planes, one can stipulate that the damping due to the wall is accompanied by the appearance of a very weak secondary oscillation. Hence, in addition to the in-plane zigzag oscillations of bubble, the bubble experiences steady out-of-plane bouncing motion. However, the rebound amplitude is small as compared to the amplitude of path oscillations.

By increasing the column inclination angle up to 15º, the bubble bouncing against the wall still persists, albeit becoming close to the sliding regime (as confirmed by the trend of the square symbols in Figure 2.3). The bubble-wall collisions did not promote the instability of the bubble path to evolve into a three-dimensional one. Similar observations were reported by [21] for bubble collisions with a vertical wall.

For the bubble rise in 40 wt.% glycerol (Table 2.2), the path instability is the result of wake instability or fore and aft asymmetry shape oscillations. Since the bubble shape is far from the wobbling regime, it is conceivable that wake instability, with formation of two standing eddies past the bubble, is the likely cause for path instability. Jeong and Park [21] suggested that the wall has a stabilizing effect on the bubble wake to maintain a two-dimensional bouncing motion. As the bubble bounces against an inclined wall, the buoyancy force component orthogonal to the wall pulls the bubble towards the wall while opposing the wake-induced lift force [35].

However, since the bubble bounces and oscillates in two different directions, it suggests that the wall-normal movement of the bubble is governed not only by the vortex-induced lateral forces, but also by the surface energy during the bubble-wall collision to maintain the bouncing motion against the wall. Similar conclusion was reached by Jeong and Park [21] and later by Lee and Park [26] who investigated the bubble-wall collision for bubbles injected in very close vicinity of a vertical wall. Both studies reported that the wall-normal bubble migration is mostly driven by the transport between the excess surface energy and the kinetic energy. Despite the energy dissipation during bubble-wall collision, the accumulation of kinetic energy in the shape deformation and then transport back to the wall-normal kinetic energy across the collision maintains the rebounding motion with large amplitude.

As the bubble migrates away from the wall, the bubble wake is prematurely detached, unlike a free zigzagging bubble, due to the wall impact. This results in smaller vortex-induced lateral oscillation of bubble motion. Hence, the effect on the lateral oscillation in x-direction of the wall and its inclination deserves some attention. For this purpose, the amplitudes of the in-plane oscillations for vertical and 10º and 12º tilted columns were measured. The plane in which in-plane zigzag oscillations occur was located by using a new coordinate system (x', y'). To compare the effect of the wall interference on the amplitude of in-plane oscillations, instantaneous amplitudes of the velocity oscillations of $v_{x'}$ were computed using a Hilbert transform [49]. Figure 2.4b shows the instantaneous amplitudes of the lateral velocity oscillations $(v_{x'})$, for the vertical, and 10º and 12º tilted columns. For each of the three angles of the column axis from the vertical axis, three tests have been selected to be shown in the Figure. Comparison of the amplitudes of the in-plane zigzag oscillations $(v_{x'})$ in the wall-free bubble lateral velocity (vertical column) and the lateral velocity for the bubble rising beneath the wall of the inclined columns (10º and 12º tilted from vertical) shows that the impact of the wall on the in-plane zigzag oscillations caused by the wake-induced lift force, is negligible. Despite the small difference between the amplitudes of oscillations for the three cases shown in Figure 2.4b, reduction of the amplitude from 0 to 10 and 12 is obvious (~12 mm/s). The bubble motion beneath a 15º tilted wall and 40 wt.% glycerol solution is close to the sliding region resulting in large uncertainties in measuring trajectory amplitude and normal velocity. Therefore, the largest inclination angle of 15º in this study was not shown in Figure 2.4b.

We computed the drag and lift coefficients of the bubbles by applying the Kirchhoff equations to the motion of a zigzag and helicoidal rising bubbles in a stagnant liquid [10, 50, 51]:

$$\rho V\left(\mathbb{A}.\frac{dU}{dt}+\Omega\times\mathbb{A}.U\right)=F \tag{2.6}$$

To calculate forces, the quantities in Eq. 6 are evaluated in the lab frame and projected onto an orthogonal coordinate system (1, 2, 3) which rotates with the bubble (Figure 2.1c).

Where $\Omega_1=\frac{\mathrm{d}\phi}{\mathrm{d}t}\cos\theta$, $\Omega_2=\frac{\mathrm{d}\phi}{\mathrm{d}t}\sin\theta$, $\Omega_3=-\frac{\mathrm{d}\theta}{\mathrm{d}t}$. $\mathbb{A}$ is the added mass tensor ($\equiv c_m\rho V$), where c_m is calculated using the aspect ratio of the bubble (Lamb, 1945):

$$c_m=\alpha/(2-\alpha) \tag{2.7}$$

$$\alpha=2/(1-x^{-2})\left(1-\frac{x^{-2}}{\sqrt{1-x^{-2}}}\arcsin\left(\sqrt{1-x^{-2}}\right)\right) \tag{2.8}$$

Figure 2.5 shows the hydrodynamic forces for zigzag and helicoidal rising bubbles in the vertical column. For a zigzag rising bubble, the frequency of drag oscillations is twice the path oscillation frequency, while the lift force has the same frequency as the path oscillations. For a flattened spiral bubble, the lift force, F_{L2}, becomes steady, in spite of decreased, although still persisting, oscillations of drag and buoyancy. This is attributed to the relatively similar wake flow structure for the zigzagging and flattened spiral bubbles investigated in this study, unlike the spiral rising bubble studied by Shew et al. [51].

(a)

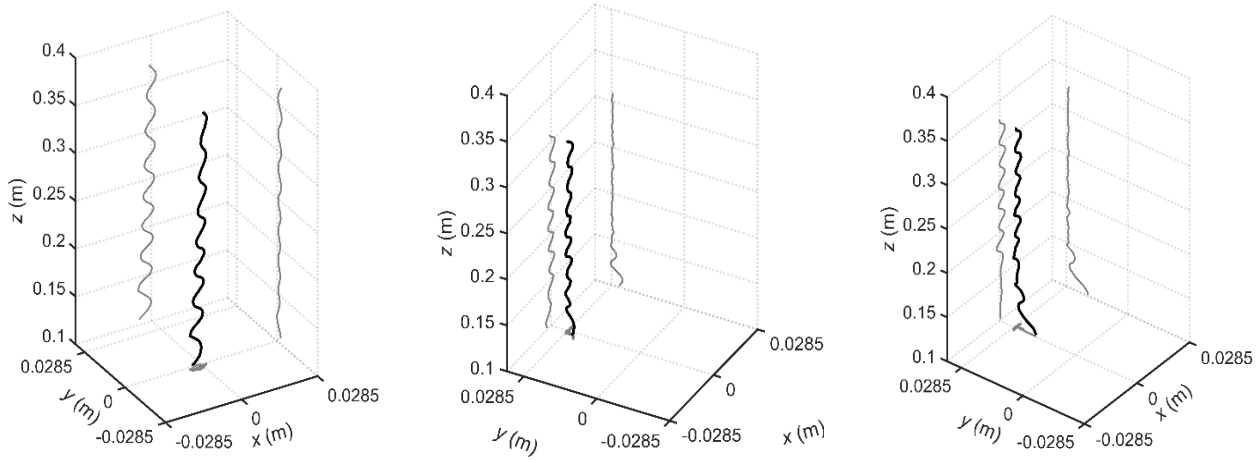

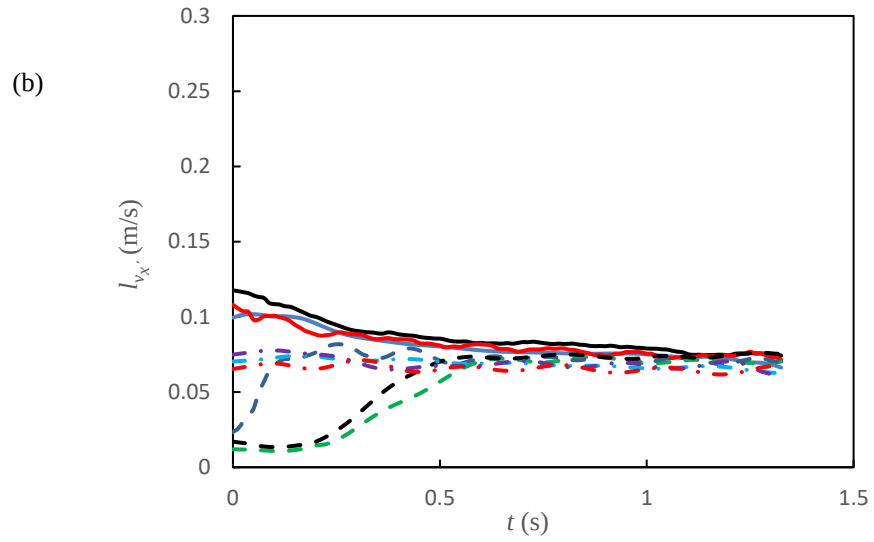

Figure 2.4. (a) Bubble trajectory for vertical column and inclined column filled with 40 wt.% glycerol. Left to right: inclination angle is 0º, 7º, and 10° from vertical, continuous black line: three-dimensional bubble path, continuous gray line: projections of the bubble path onto the sides and bottom. (b) Velocity amplitude of zigzag lateral oscillations for vertical column and inclined column (10º, and 12°) filled with 40 wt.% glycerol. continuous line: vertical column, dashed line: 10º tilted column, dotted-dashed line: 12º tilted column.

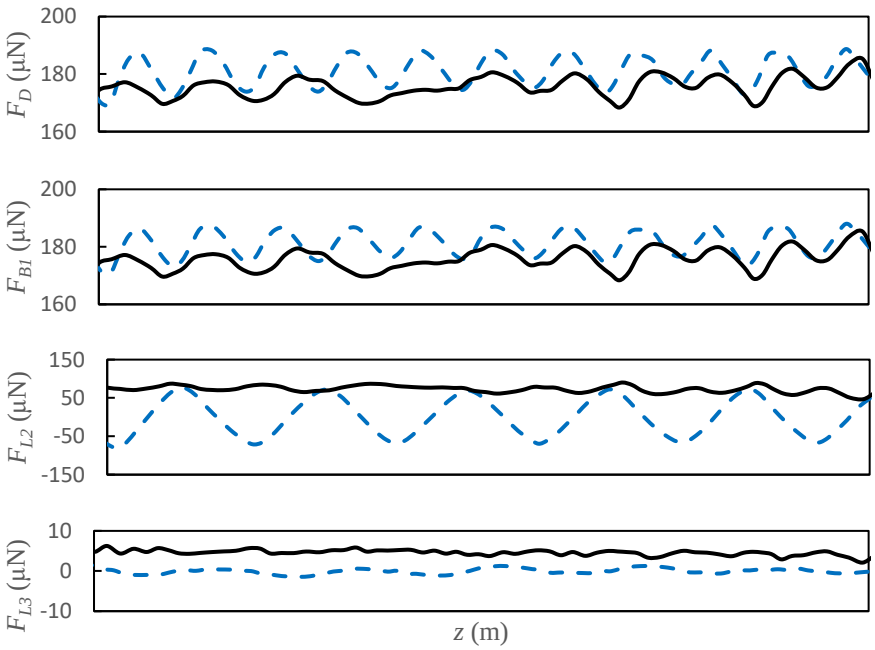

Figure 2.5. Magnitudes of drag, buoyancy, and lift forces measured for a zigzagging (blue dashed line) and a helicoidal rising (black line) bubble in 40 wt.% glycerol and water, respectively.

For We = 2.9, the bubble shape lies in the wobbling regime (Figure 2.2a) exhibiting an aspect ratio $X \geq 1.4$. Figures 2.6a,b show the bubble trajectory in water for the vertical (reference rising path) and for three selected inclination angles of the column. The helical rising trajectory of the bubble is the result of unequal vortex pairs past the bubble and responsible for an angular velocity around an invariant vorticity center [52]. The bubble dynamics involves two modes of horizontal oscillations with the same frequency of 39 rd·s^{-1}. The phase shift between the two modes of instability is equal to $\pi/2$ which makes the horizontal projection of the trajectory (on $x - y$ plane) looks like a circle/an ellipse (Figure 2.6b).

When the bubble approaches the wall, the angular frequencies of the two lateral bubble path oscillations were computed from fitting the bubble trajectories with sinusoidal functions. The angular frequencies of bubble oscillations in both planes ($x - z$ and $y - z$) are equal to 39 rd·s^{-1} as far as the bubble has not contacted the wall. Similar frequency was reported by [4] for a helicoidally rising bubble ($d = 2.49$ mm).

For the range of inclination angles analyzed in this study (0º-15º), the bubble experiences steady bouncing. After an initial amplitude damping of the horizontal oscillations the bubble rebounds continuously and irregularly over time. A similar interpretation as for the two-dimensional bubble rising trajectory can be invoked here regarding competition between the wake-induced lift force and the normal-to-wall buoyancy force to pull the bubble toward the wall. An interesting observation of the bubble rising behavior along the inclined column, is that the two out-of-mode oscillations are maintained during the bubble-wall collisions preserving the bubble three-dimensional motion whereby collisions against the wall do not change the flow structure. Hence, addition to the observation made for the zigzag bubble path for which a wall stabilizing effect was found, the helicoidal bubble path tends to maintain the three-dimensional motion induced by for-and-aft asymmetry of the bubble shape.

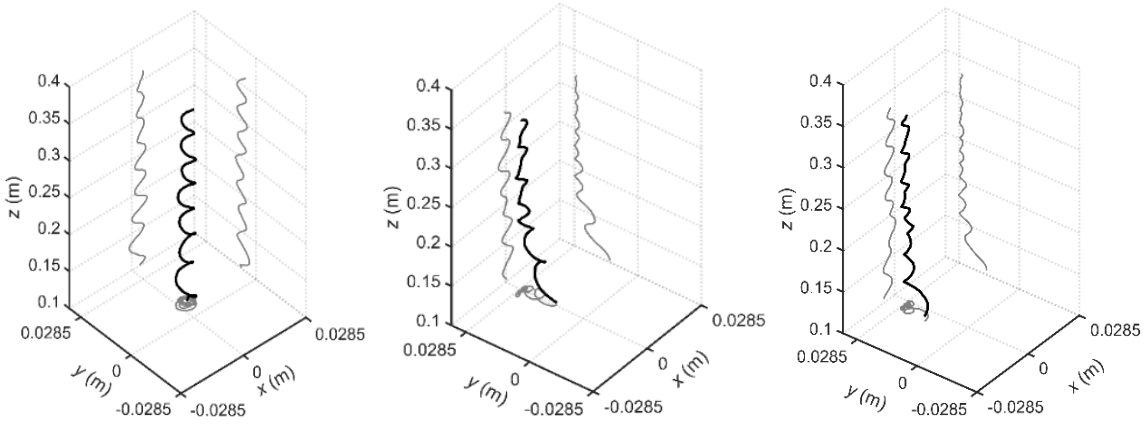

Figure 2.6. Bubble trajectory for vertical column and inclined column filled with water. Left to right: inclination angle is 0º, 7º, and 10° from vertical, continuous black line: three-dimensional bubble path, continuous gray line: projections of the bubble path onto the sides and bottom.

2.6.2.2. Instantaneous Bubble Velocities

In this section, the instantaneous three-dimensional bubble velocity components are obtained after successive subtractions of the positions of the bubble center of mass divided by the imaging sampling period. The three components of bubble velocity are shown in the Figure 2.7 and 2.8, for the bubbles rising in the inclined columns between 0º-15º and filled with 40 wt.% glycerol and water, respectively. The history of the instantaneous bubble velocities exhibits oscillations in both axial and lateral velocities for the vertical column. For the bubble rising in 40 wt.% glycerol, the oscillations of v_x and v_y are π phase-shifted whereas the frequency of bubble axial velocity, v_z, is twice that of the lateral velocities in agreement with previous investigations [4]. The instantaneous axial rise velocity of the bubble reaches a maximum (minimum) at a peak (inflection) point of its oscillating trajectory, while the bubble lateral velocities turn to maximum/minimum at the trajectory inflection points. In the inclined column, although bubble bouncing on the wall increases the frequency of v_y, the fact remains that the frequency of v_z is still twice v_x. Akin to the trajectory data of Figures 2.4,2.6, once a bubble hits the wall, the plane of oscillation is modified when column tilt angles exceed 7º. As shown for zigzagging bubbles, once a bubble starts to bounce along the wall the plane of zigzag oscillations is parallel to the wall ($x - z$ plane). However, according to Barbosa et al. [35] criterion, the bubble bounces

against the wall (y direction), as well. This out-of-plane motion of the bubble is negligibly small comparing to the in-plane zigzag motion. The wall-normal velocity is $v_y \leq 0.015$ m/s.

At its approach to the wall, the wall-normal bubble velocity (v_y) decreases. Collision reflects in a sign change of the velocity followed by an accelerating bubble, as it migrates away from the wall. Upon reaching the maximum distance from the wall, v_y reduces to zero again and resumes the next bouncing. To better exemplify the alterations of velocity oscillations, the instantaneous phase of the three components of bubble velocities is calculated. This latter is obtained by decomposing the de-trended signal of the three velocity components over time using Hilbert and Fourier transforms [49]:

$$\mathrm{HF}\,[v'(t)] = \mathrm{FT}^{-1}[-i\,\mathrm{sgn}(f)\mathrm{FT}\,[v'(t)]\,(f)] \tag{2.9}$$

where $v'(t)$ is the de-trended instantaneous velocity, the instantaneous phase of the oscillations is obtained as:

$$\varphi\,(t) = \mathrm{Arg}\{v'(t) + i\,\mathrm{HF}\,[v'(t)]\} \tag{2.10}$$

As shown in Figure 2.7b, before a bubble-wall contact, the oscillation phases of v_x and v_y are two straight lines with same gradient, so the oscillation frequencies of v_x and v_y are equal and constant. However, when the bubble starts bouncing against the wall, the phase of v_y exhibits a rapid change, as is obvious for inclination angles above 7°. The phase of v_x maintains the straight line with same gradient during the total rising time. Figure 2.10c shows that the oscillations of v_z is still twice the in-plane oscillations, i.e., zigzag motion. This shows the negligibly small wall effect on the oscillations of the axial velocity.

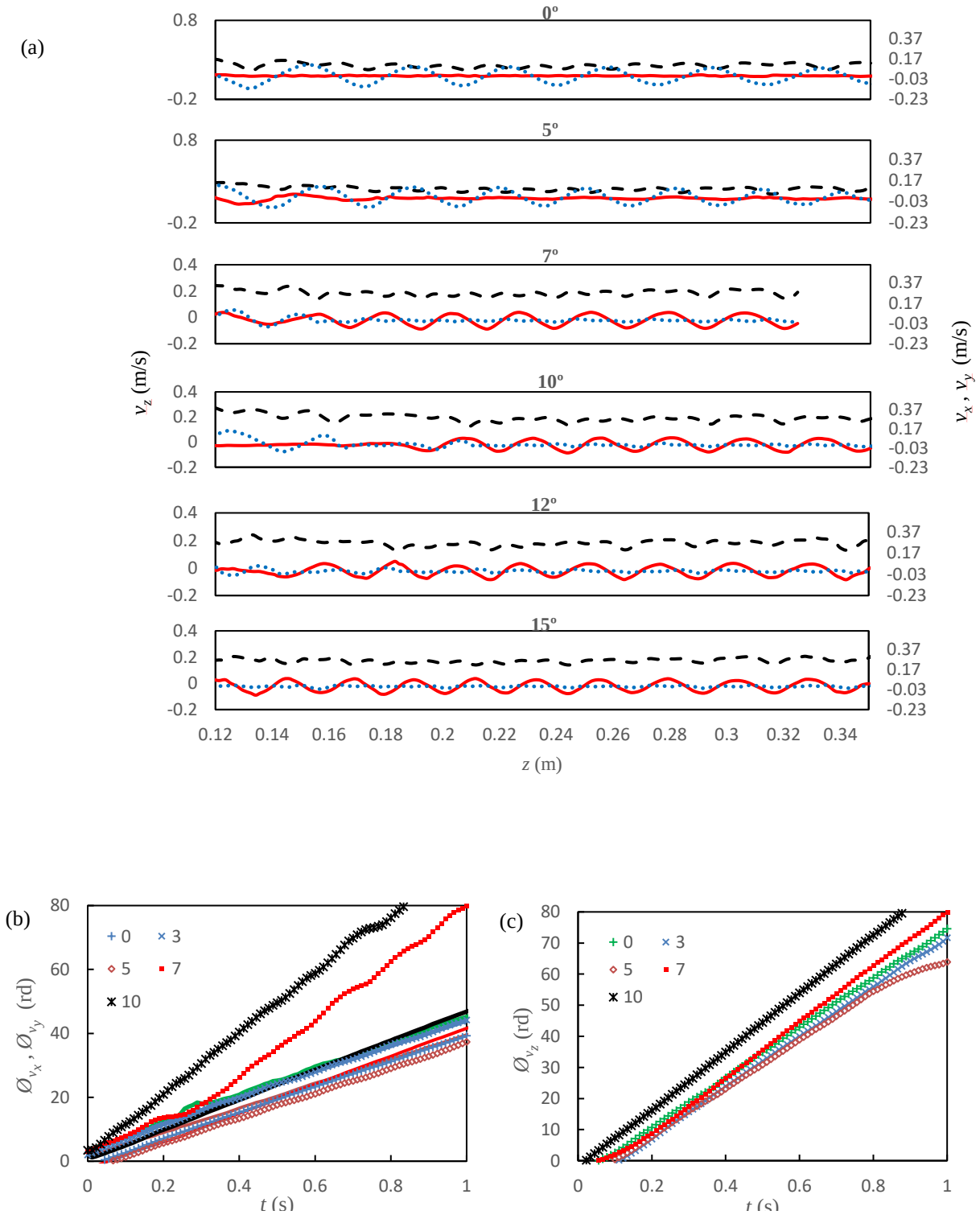

Figure 2.7. (a) Instantaneous bubble horizontal and axial velocities in the inclined column. Dashed line: axial velocity (vz), continuous line: lateral velocity (vx), dotted line: lateral velocity (vy), (b) Instantaneous phase of vx and vy, continuous lines: φ_{v_x}, symbols as shown in the legend: φ_{v_y}, (c) Instantaneous phase of vz (φ_{v_z}). (for zigzag rising bubble in 40 wt.% glycerol).

The instantaneous velocity components of bubbles rising in water-filled tilted columns are likewise shown in Figure 2.8a. The same phase shift between the two horizontal velocity components is preserved as for the trajectory data. As long as a bubble-wall contact has not occurred, a constant phase shift equal to $\pi/2$ prevails. However, bubble-wall collisions make the oscillations in the direction of inclination (y) irregular. Despite a loss in oscillation regularity, the phase difference between the lateral velocities can still be recognized. On the one hand, the oscillation frequency of v_y increases because of the bubble bouncing against wall. On the other hand, the oscillations of v_x remain similar to the case of a bubble rising in the reference (vertical) column. Figures 2.8b,c show the instantaneous phase for the three bubble velocity components. For the reference case, the v_x and v_y phases are two straight lines with the same gradient, and the oscillation frequencies of both transverse velocity components are equal and constant. This holds true as long as a bubble stays away from the wall. Once the bubble contacts the wall, the slope of the phase curve changes significantly demonstrating the increases of the frequency in *y* direction, in spite of φ_{v_x} still following an equal-gradient trend.

(a)

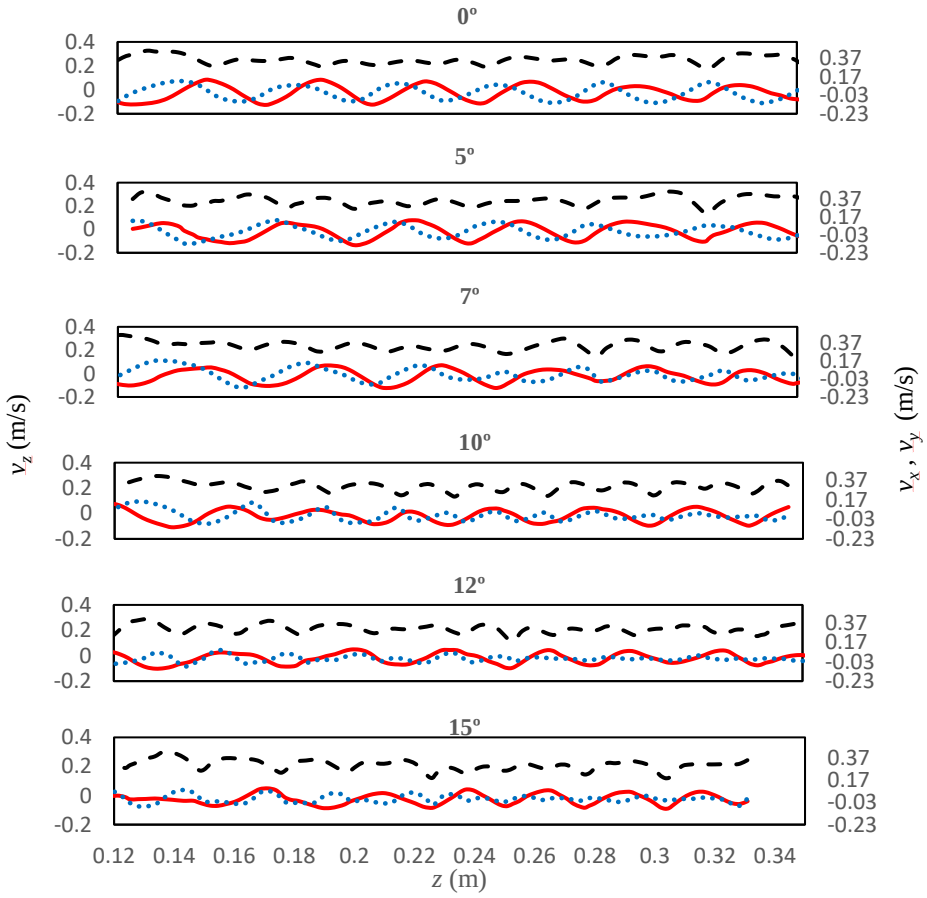

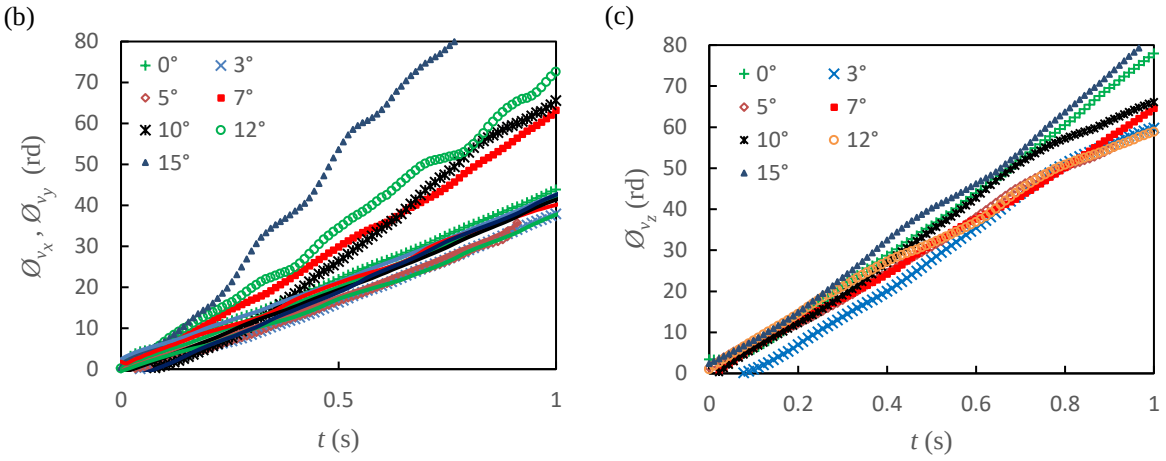

Figure 2.8. (a) Instantaneous bubble horizontal and axial velocities in the inclined column. Dashed line: axial velocity (v_z), continuous line: lateral velocity (v_x), dotted line: lateral velocity (v_y), (b) Instantaneous phase of v_x and v_y , continuous lines: φ_{v_x}, symbols as shown in the legend: φ_{v_y}, (c) Instantaneous phase of v_z (φ_{v_z}). (for helicoidal rising bubble in water).

2.6.2.3. Mean Bubble Velocities

Contraction into time-averaged (or mean) components of the bubble velocity rising in inclined column is carried out next for both helical (in water) and zigzag (in 40 wt.% glycerol solution) paths. Figure 2.9 shows the effect of inclination angle on the mean axial and lateral velocities of bubbles rising in water and 40 wt.% glycerol. The global effect of wall on the mean velocities is similar for both regimes. Steepened vessel inclination prompted stronger wall effects resulting in reduced bubble axial velocity. The mean lateral velocities in both x and y directions are compared in Figure 2.10b. It shows that the mean of bubble velocity in the direction of inclination (y direction) has an initial increase, due to the increasing role of buoyancy in that direction while the bubble is approaching the wall. Unlike v_y, v_x is rather uniform and the effect of inclination angle on v_x is negligible. For axial velocity, Masliyah et al. [33] also showed that, as the wall was tilted more from the vertical, the rise velocity decreases monotonically. Due to the bubble deformation, they found that the drag coefficient can be well correlated with the bubble Reynolds number and the Eotvos number modified to account for the angle of wall inclination as, $Eo_m = Eo \cos\theta$.

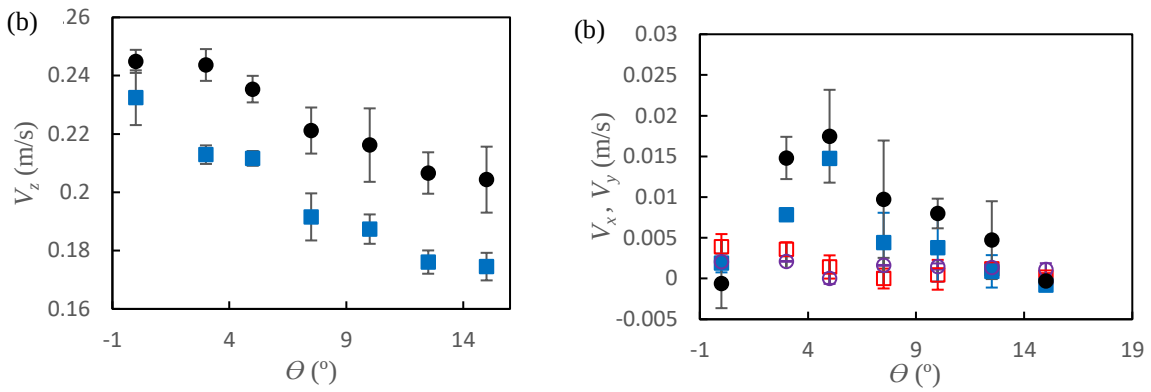

Figure 2.9. Average bubble velocities vs. column inclination angle. (a) axial velocity, circle symbols: helicoidal rising bubble, square symbols: zigzag rising bubble, (b) lateral velocities, filled symbols correspond to v_y, and empty symbols correspond to v_x, circle symbols: helicoidal rising bubble in water, square circle symbols: zigzag rising bubble in 40 wt.% glycerol solution.

2.6.2.4. Bubble Aspect Ratio and Orientation

The variation of the bubble aspect ratio and orientation is discussed in the case of zigzag ($Mo = 10^{-11}$, $Eo = 1.5$) and spiral ($Mo = 10^{-9}$, $Eo = 1.67$) trajectories. Before delving into the discussion of the instantaneous (Figure 2.10) and averaged bubble aspect ratios (Figure 2.11), and instantaneous bubble orientations (Figures 2.12, 2.13), the findings regarding the vertical reference column are worth summarizing. According to the bubble shape regime map, the bubble shape is reminiscent of an oblate ellipsoid with its symmetry semi-minor axis parallel to the bubble-center velocity. The bubble shape oscillates during its zigzag and helical ascensions in the reference column, which results in oscillating aspect ratios of the rising bubble. At each oscillation, while the bubble reaches the center of its horizontal path, the horizontal velocity and aspect ratio increase and the axial velocity decreases then the opposite trends occur when the bubble reaches the trajectory peak. The frequency of oscillations in axial velocity and aspect ratio is twice the bubble path oscillations (minimum and maximum occurs at peak and inflection points of trajectory, respectively). Apart from the oscillations of bubble aspect ratio in the reference column, the bubble-wall collisions also impact the bubble shape.

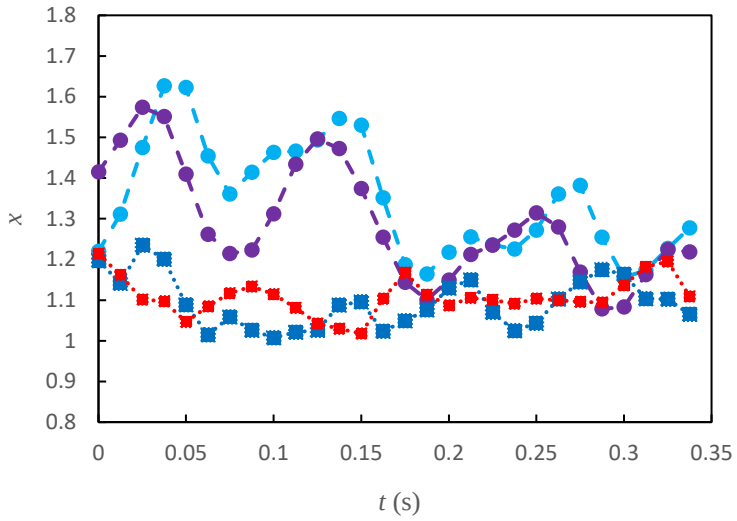

Figure 2.10. Instantaneous bubble aspect ratio for the bubble rising in 10º tilted column. Dashed lines: liquid phase is water (helicoidal bubble rise in the reference column), dotted lines: liquid phase is 40 wt.% glycerol (zigzag bubble rise in the reference column).

The bubble aspect ratio for both cases of the two and three-dimensional rising motion is shown in Figure 2.10. As expected, the helicoidal rising bubbles have higher aspect ratio than the zigzag rising bubble [14]. The bubble aspect ratio increases as the bubble approaches towards the wall, then decreases once the bubble collides with the wall before increasing again while the bubble migrates away from the wall. Due to bubble deformations in the wobbling regime, the aspect ratio of the helicoidally rising bubble fluctuated greatly during rebounds, as opposed to the gentler fluctuations for the zigzag bubble path. The mean of aspect ratio and fluctuations (expressed as standard-deviation bars) of the bubbles rising in the vertical and inclined columns as measured from the images captured from the front and side views are shown in Figure 2.11. The tendency of the aspect ratio is to decrease due to wall impact as column inclination increases for both bubble path types.

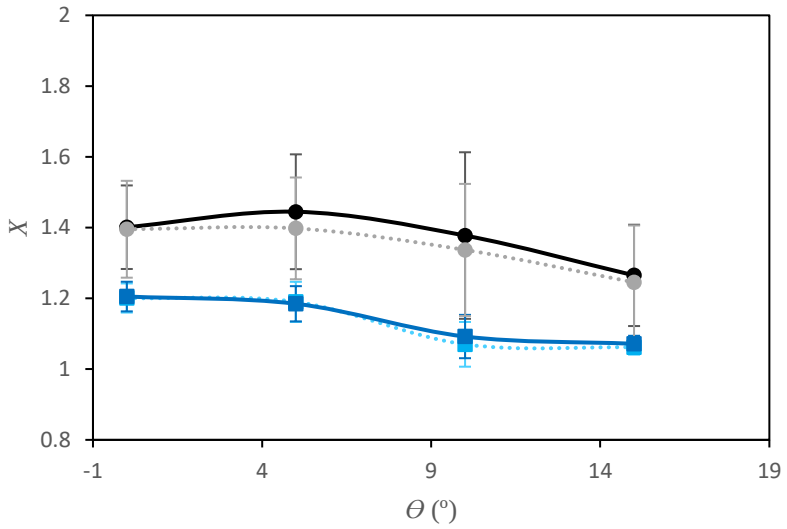

Figure 2.11. Mean of bubble aspect ratio vs. inclination angle of the column for helicoidal rising bubble (circle symbols) and for zigzag rising bubble (square symbols). Continuous lines: aspect ratio calculated from front view images. Dotted line: aspect ratio calculated from side view images.

As the bubble approaches and then moves away from the wall, it also changes orientation. As a typical trend, the bubble rises with its symmetry axis (minor axis) aligned to its trajectory. Since, the bubble has an oblate ellipsoidal shape, the angle between the major axis of the bubble and the wall (β) is measured, which is shown in Figure 2.4a. For the helicoidal bubble rising in water, bubble approaches the wall with one head of the ellipse and rolls over such that bubble orientation changes $\beta = 160° - 180°$ during the collision. Then, the bubble leaves the wall following the other head (tail) of the ellipse (Figure 2.12c). To quantify the effect of the column inclination on the bubble orientation, the variation of β during the bubble rise for 10º and 15º tilt angles is shown in Figure 2.12. When the bubble bounces against the wall, β increases as the bubble approaches the wall and drops down suddenly at the instant of collision. After impact, β recovers back as the bubble moves away from the wall. The steeper the inclination angle, the steeper (and the briefer) the β changes over one period: 0.15 s and 0.2 s, respectively, for the 15º and 10º tilted column.

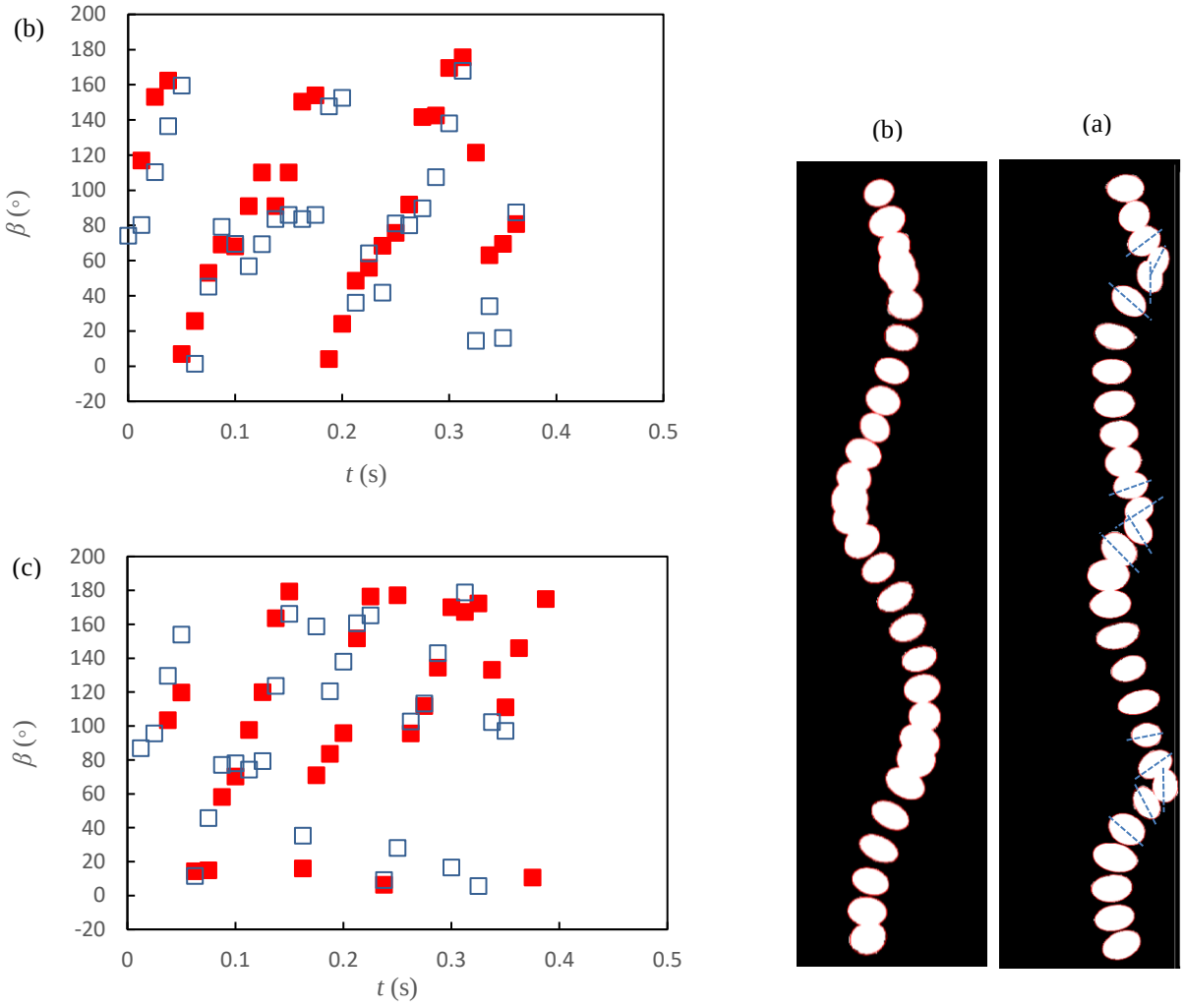

Figure 2.12. Instantaneous bubble orientation for the helicoidal bubble rising in (a) 10º, (b) 15º tilted column for two bubbles shown using different symbols, (c) bubble image during collision in 10º tilted column $x-z$ plane, (d) same bubble in $y-z$ plane.

Figure 2.13 presents the variation of bubble orientation versus dimensionless time $\left(t^* = tv_y/d_{\mathrm{eq}}\right)$, where v_y is the normal velocity, for three bubble-wall collisions against a 10º-tilted wall for the spiral and zigzag rising paths. The origin ($t^* = 0$) is the collision instant when the distance of bubble center of mass from the wall is less than the free bubble equivalent radius ($h < R_0$) and when the normal velocity changes its sign. For the bubble rises in water, the orientation changes 170º±10º during the collision, while for the bubble rises in 40 wt.% glycerol, bubble orientation changes 20º-70º in different rebounds.

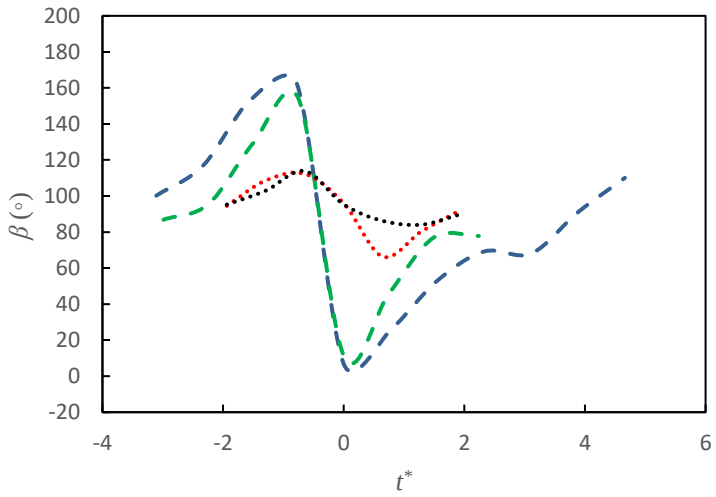

Figure 2.13. Instantaneous bubble orientation during wall-collision for the helicoidal rising bubble (dashed lines) and zigzagging bubble (dotted lines) in 10° tilted columns for two different bubbles.

2.6.2.5. Coefficient of Restitution

The coefficient of restitution, $\epsilon = \left|\frac{v_{\text{depart}}}{v_{\text{approach}}}\right|$, in which v_{approach} and v_{depart} correspond to the pre- and post-collision particle velocities is an indirect measure of energy dissipation resulting from a collision. This descriptor has been used by several researchers to model particle-wall interactions for horizontally oriented walls [21, 27-29]. For wall collisions of a solid particle, Joseph et al. [43] showed that the restitution coefficient correlates well with the particle Stokes number as $\epsilon_n = f(St)$. For liquid droplets, Legendre et al. [27] introduced a modified Stokes number to account for the effect of added mass ($St^* = (\rho_{\text{P}} + c_{\text{m}}\rho)d_{\text{eq}}v_{\text{approach}}/9\mu$) and suggested a correlation of the $\epsilon = f(St^*)$ type. In the case of rectilinearly rising bubbles colliding against a horizontal wall, Zenit and Legendre [28] further amended the correlation as $-\log\epsilon_n \sim \left(\frac{Ca}{St^*}\right)^{\frac{1}{2}}$, where $Ca = \mu U/\sigma$. For the collision against a horizontal wall of zigzag and helical rising bubbles, Pelletier et al. [29] showed that the normal coefficient of restitution was estimated well with the correlation of Zenit and Legendre [28] for rectilinearly rising bubbles. For large deformable bubbles zigzagging next to a vertical wall, Jeong and Park [21] correlated their lateral bouncing in terms of St^*, and their data were fitted well by $\epsilon_n = \frac{\exp(5St^*)}{30}$. Studies on bubble-wall collisions were limited, to our knowledge, only to vertical and horizontal walls, and two-dimensional bubble motion.

For the three-dimensional motion of the bubbles considered in our study, Figure 2.14 shows the evolution of ϵ with the modified Stokes number, St^*, for several rebounds. Prior to finding v_{depart} and v_{approach}, the distance to wall, h, of the bubble centre of mass was measured for each frame. The bubble was considered in contact with the wall, as long as $h < R_0$, and before the bubble tail was completely detached form the wall. This has been followed for computing the approaching and departing velocities before and after bubble-wall collision. Since the frame rate in this study did not always allow full-timescale image capture of the collisions, an uncertainty was calculated for each collision as shown for each data point (Figure 2.14). For each data point, the uncertainty is calculated considering the instant of collision as once the distance between the bubble centre of mass and the wall is less than the initial bubble equivalent radius ($h < R_0$). Then we calculate uncertainties for v_{approach} and v_{depart} using the average of the two consecutive velocities before and after the collision, respectively.

One notices that the wall-normal bouncing of a helically rising bubble shows relatively similar dependence with the modified normal Stokes number proposed by Legendre et al. [27] for bubbles and can be fitted to $\epsilon_n = \exp\left(\frac{-\beta_1}{\sqrt{St^*}}\right)$, where $\beta_1 = 3.5$. Another functional dependence, suggested by Legendre et al. [27] for solid spheres and liquid drops. i.e. $\epsilon_n = \exp\left(\frac{-\beta_2}{St^*}\right)$, where $\beta_2 = 35$, has been also shown in Figure 2.14. However, there are some collisions for which the restitution coefficient is much higher than the predicted value. Such excursions are believed to be caused by differences in bubble positions in the trajectory during collisions. In the present study, it was found that ϵ does not show a clear dependence to Ca/St^* as suggested by Zenit and Legendre [28] for gas bubbles colliding on a horizontal wall. This lack of correlation was also reported for the case of a vertical wall by Jeong and Park [21] and was attributed to bubble sizes larger than the capillary length for air-water system (i.e. 2.7 mm). Another reason was ascribed to the difference between the normal/lateral bouncing achieved by collisions against horizontal and vertical wall.

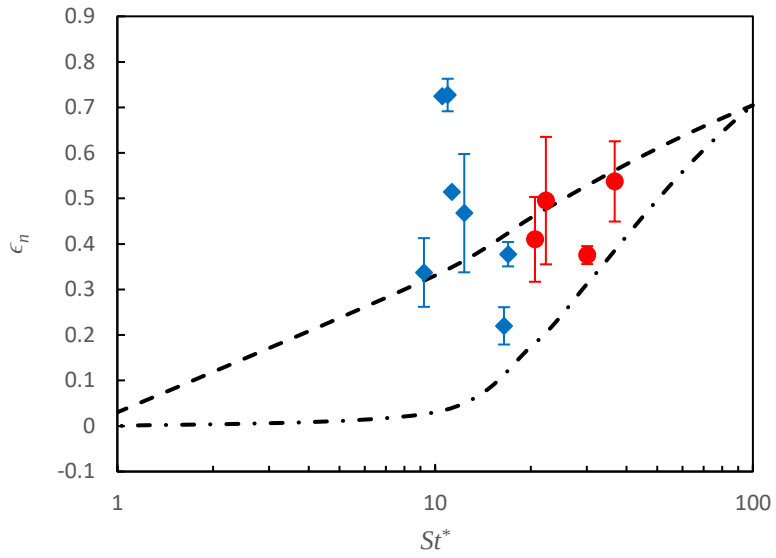

Figure 2.14. Normal coefficient of restitution vs. modified Stokes number for bubble with helicoidal motion. Circle symbols: for the bubble rises in the 10° tilted column, diamond symbols: for the bubble rises in the 15° tilted column. Dashed line: corresponds to $\epsilon = \exp\left(\frac{-\beta_1}{\sqrt{St^*}}\right)$ with $\beta_1 = 3.5$, dashed-dotted line: corresponds to $\epsilon = \exp\left(\frac{-\beta_2}{St^*}\right)$ with $\beta_2 = 35$.

2.6.2.6. Energy Balance

The kinetic and surface energies and the amount of energy dissipation are estimated for bubbles rising spirally and in zigzag against the wall of the inclined column. The kinetic energy is calculated as:

$$E_k = \frac{\pi}{12} d_{eq}^3 \left(\rho_g + c_m \rho_l\right)\left(v_x^2 + v_y^2 + v_z^2\right) \tag{2.11}$$

The effect of bubble-wall collisions on the directional kinetic energy components is scrutinized in terms of vertical, E_{kv_z}, wall-normal, E_{kv_y}, and tangent, E_{kv_x}, terms in Eq. 11. In all cases, the added-mass coefficient, c_m, was estimated according to Eq. 7.

The surface energy is straightforwardly obtained from knowledge of surface tension and bubble surface area:

$$E_{\text{sur}} = \sigma A \tag{2.12}$$

in which surface area for an oblate ellipsoid is computed as:

$$A = \frac{\pi d_e^2}{2}\left(1 + \frac{1-e^2}{e}\tanh^{-1} e\right) \tag{2.13}$$

where $e^2 = 1 - \frac{1}{x^2}$

The variations of energy components typical of spiral bubble path are shown in Figure 2.15 for two column tilt angles. Each subplot traces path history during three subsequent bubble bounces against the wall. The corresponding *y*-component of the bubble trajectory is plotted in red. E_{sur} decreases as the bubble approaches the wall and reaches a local minimum at the instant of collision. For bubbles rising in the wobbling regime, the contribution of E_{sur}, as compared to the total kinetic energy, is a dominant source for maintaining the rebounding bubble motion. As the inclination angle increases in this regime, the contribution of E_{sur} increases at the expense of a decreasing contribution of E_k. Both the normal-to-wall (E_{kv_y}) and tangent-to-wall (E_{kv_x}) components of the kinetic energy contribute the least to the total kinetic energy, whereby E_{kv_z} is the dominant term. E_{kv_x} and E_{kv_y} plots show maximum peaks just before the bubble-wall collision. Similar behavior for the normal-to-wall component of kinetic energy was reported by Jeong and Park [21] in their two-dimensional study of zigzagging bubbles rising along a vertical wall. E_{kv_z} decreases when the bubble migrates toward the wall resuming an increase after collision in agreement with observations reported by Moctezuma et al. [24], Figueroa-Espinoza et al. [48] and Jeong and Park [21].

Unlike spiraling bubbles undergoing large deformations in the wobbling regime, the lower contribution of E_{sur}, as compared to the total kinetic energy, is considered to be the characteristic of two-dimensional zigzagging bubble trajectories. This is illustrated in Figure 2.16 for a zigzagging bubble rising in 40 wt.% glycerol solution against the wall of a cylindrical column. Furthermore, as discussed previously in the section of reconstructed trajectories, the (zigzag) plane of bubble oscillations is parallel to the wall with small-amplitude bubble rebounds against the column wall. Hence, the major contribution to the kinetic energy budget for zigzagging bubble rises is E_{kv_z} followed next by E_{kv_x} ($\ll E_{kv_y}$) in contrast with the comparable contributions of E_{kv_x} and E_{kv_y} for bubbles spiraling in water-filled 10º inclined column (Figure 2.15).

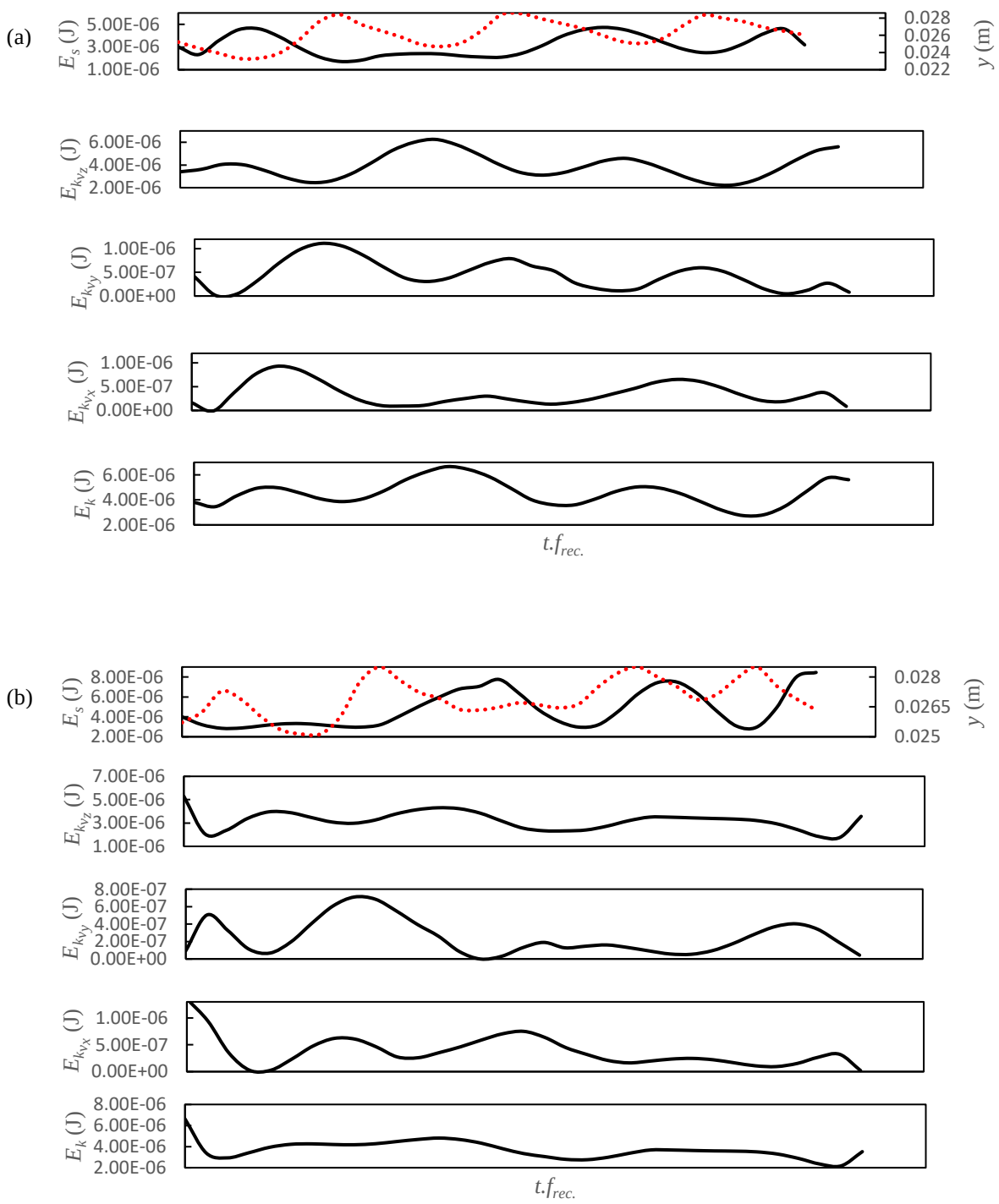

Figure 2.15. Bubble energy contributions vs. dimensionless time (normalized by recording frequency, f_{rec}) for spiral rising bubble in (a) 10º and (b) 15º tilted column, red dotted line: bubble trajectory projection in $y-z$ plane.

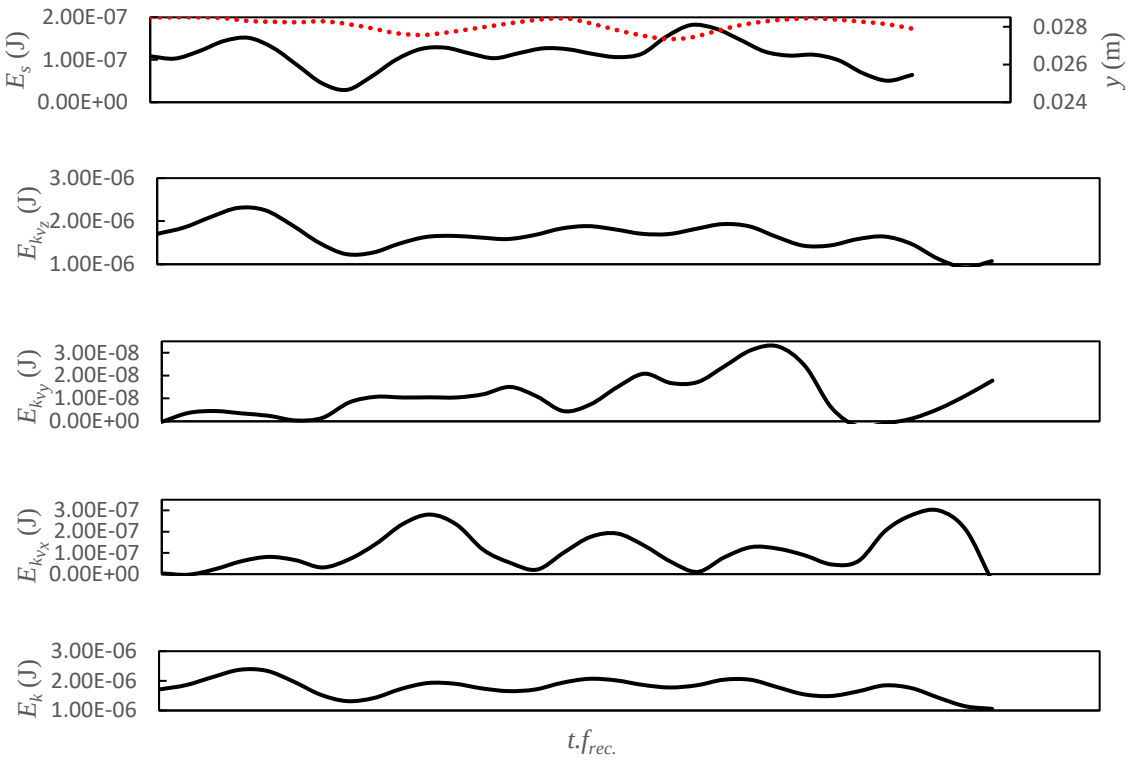

Figure 2.16. Bubble energy contributions vs. dimensionless time (normalized by recording frequency, f_{rec}) for zigzag rising bubble in 10º tilted column, red dotted line: bubble trajectory projection in $y - z$ plane.

2.7. Conclusion

The behavior of single air bubbles experiencing bubble-wall collisions in an inclined column (0-15º tilts), filled with different liquids, was analyzed for three bubble rise motions, namely, rectilinear, zigzag, and spiral paths. The three-dimensional trajectory data, reconstructed using two synchronized high-speed video cameras, provided a full description of the bubble rise at high Reynolds numbers, and moderate Weber numbers. The spiral paths of single bubbles rising along the inclined wall of the column showed that the bubble maintains two out-of-phase modes of oscillations, with π/2 phase lag. For the zigzag paths, the bubble plane of motion changed when the bubble reached the wall resuming zigzag motion with small amplitude rebounds. The bubble-wall contact increased the frequency of bubble oscillations in the direction of inclination of the column. However, the frequency of oscillations tangent to the wall (x direction) remained the same as for the (wall-) free rising bubbles, i.e., 39 rd/s for both zigzag and spiral bubble paths. For the zigzagging bubble, the impact of bubble-wall collision was marginal on the amplitude of the wake-induced in-plane oscillations of the bubble rising beneath the wall. Evaluating the wall impact on

bubble rebounds, in terms of coefficient of restitution, credited some predictive confidence for a correlation established on the basis of liquid droplets impacting horizontal walls. The trend of variations in restitution coefficient tested for two inclination angles agreed well with the variations in wall-normal component of the kinetic energy. The three-dimensional data gathered in this study also provided insightful information on the three kinetic energy components for bubbles rising in helical and zigzag motions. The two lateral components of the kinetic energy (normal and tangent to wall) have similar contributions within the total kinetic energy budget of spirally rising bubbles which is maintained up to the highest inclination angle, i.e. 15º. However, the kinetic energy contribution of the normal component of zigzagging bubbles is negligible. This agrees well with the two-dimensional bubble rising upheld beneath the wall. The measured normal restitution coefficient for a helically rising bubble showed relatively similar dependence with the modified normal Stokes number proposed by [27] and could be fitted to $\epsilon = \exp\left(\frac{-\beta_1}{\sqrt{St^*}}\right)$, where $\beta_1 = 3.5.$ in the same manner as the normal wall collisions of liquid droplets. The contribution of surface energy in the total energy during bubble rebounds against the wall is higher for the helicoidal bubble rise, due to the more surface deformations of the bubble in the wobbling regime, contrary to the zigzagging bubble. In this study, we highlighted the alterations in bubble trajectory and shape due to the impact of the wall of a cylindrical column. Thus, it would be important to obtain information about the helicoidal bubble wake structure modified by interaction with wall of the tilted column. The results presented in this study can be extended to applications in bubble column reactors, scrubbers, and separators in which the bubble-wall interactions and the dynamics modifications imposed by the wall are important in their performance and mass transfer characteristics.

2.8. Nomenclature

A	Surface area, m^2
$\mathbb{A}$	Added mass tensor
A_{11}	Added mass
Bo	Bond number
C_D	Drag coefficient

C_l Lift coefficient

c_m Added mass coefficient

Ca Capillary number

d Bubble diameter, m

d_{e} Equivalent bubble diameter, m

d_{major} Major axis, m

d_{minor} Minor axis, m

$d_{\parallel}$ Parallel to wall axis, m

$d_{\perp}$ Perpendicular to wall axis, m

E_k Kinetic energy, J

E_{sur} Surface energy, J

Eo Eotvos number

ϵ Coefficient of restitution

F Force, N

f Frequency, Hz

f_{rec} Frequency of recording, frames s^{-1}

FT Fourier transform

g Gravitational acceleration, m s^{-2}

h Distance of bubble center of mass from the wall, m

HF Hilbert transform

L Contact length, m

l Amplitude

l_c Capillary length, m

Mo Morton number

R_0 Initial bubble radius, m

Re Reynolds number

St Stokes number

St^* Modified Stokes number

t Time, s

U Total velocity, m s^{-1}

v Velocity, m s^{-1}

V Volume, m^3

v_{approach} Pre-collision velocity of particle, m s^{-1}

v_{depart} Post- collision velocity of particle, m s^{-1}

v' detrended velocity, m s^{-1}

We Weber number

x Aspect ratio

X Mean aspect ratio

ρ Density, kg m^{-3}

μ Viscosity, Pa s

ϕ Azimuthal angle, rd

θ Pitch angle, rd

Ω Angular velocity, m s^{-1}

φ Phase, rd

σ Surface tension, N m^{-1}

β Angle between the major axis of the bubble and the wall

Subscripts

D Drag

g Gas

I Inertia

L Lift

l Liquid

n normal to wall

p Particle

wall Wall, calculated using rise velocity parallel to wall

2.9. References

1. Besagni, G., Inzoli, F., Ziegenhein, T. *Two-Phase Bubble Columns: A Comprehensive Review.* ChemEngineering, 2018. 2(2): p. 13.
2. Shu, S. et al. *Multiscale multiphase phenomena in bubble column reactors: A review.* Renewable Energy, 2019. 141: p. 613-631.
3. Zhou, W. *Path instabilities of spheres, spheroids and bubbles*. 2016, Université de Strasbourg: Strasbourg, France.
4. Ellingsen, K., Risso, F. *On the rise of an ellipsoidal bubble in water: oscillatory paths and liquid-induced velocity.* Journal of Fluid Mechanics, 2001. 440: p. 235.
5. Kong, G. et al. *Hydrodynamic interaction of bubbles rising side-by-side in viscous liquids.* Experiments in Fluids, 2019. 60(10): p. 1-15.
6. Clift, R., Grace, J.R., Weber, M.E. *Bubbles, drops, and particles.* 2005.
7. Saffman, P.G. *On the rise of small air bubbles in water.* Journal of Fluid Mechanics, 1956. 1(3): p. 249-275.
8. Aybers, N., Tapucu, A. *The motion of gas bubbles rising through stagnant liquid.* Wärme-und Stoffübertragung, 1969. 2(2): p. 118-128.
9. Brücker, C. *Structure and dynamics of the wake of bubbles and its relevance for bubble interaction.* Physics of fluids, 1999. 11(7): p. 1781-1796.
10. Mougin, G., Magnaudet, J. *Path instability of a rising bubble.* Physical review letters, 2001. 88(1): p. 014502.
11. de Vries, A.W.G., Biesheuvel, A., Van Wijngaarden, L. *Notes on the path and wake of a gas bubble rising in pure water.* International journal of multiphase flow, 2002. 28(11): p. 1823-1835.
12. Zenit, R., Magnaudet, J. *Path instability of rising spheroidal air bubbles: a shape-controlled process.* Physics of Fluids, 2008. 20(6): p. 061702.
13. Zenit, R., Magnaudet, J. *Measurements of the streamwise vorticity in the wake of an oscillating bubble.* International Journal of Multiphase Flow, 2009. 35(2): p. 195-203.
14. Magnaudet, J., Mougin, G. *Wake instability of a fixed spheroidal bubble.* Journal of Fluid Mechanics, 2007. 572: p. 311.
15. Cano-Lozano, J., Bohorquez, P., Martínez-Bazán, C. *Wake instability of a fixed axisymmetric bubble of realistic shape.* International journal of multiphase flow, 2013. 51: p. 11-21.
16. Magnaudet, J., Eames, I. *The motion of high-Reynolds-number bubbles in inhomogeneous flows.* Annual Review of Fluid Mechanics, 2000. 32(1): p. 659-708.
17. Tomiyama, A. et al. *Terminal velocity of single bubbles in surface tension force dominant regime.* International journal of multiphase flow, 2002. 28(9): p. 1497-1519.
18. Wu, M., Gharib, M. *Experimental studies on the shape and path of small air bubbles rising in clean water.* Physics of fluids, 2002. 14(7): p. L49-L52.
19. Liu, L., Yan, H., Zhao, G. *Experimental studies on the shape and motion of air bubbles in viscous liquids.* Experimental Thermal, 2015. 62: p. 109-121.
20. Zaruba, A. et al. *Bubble-wall interactions in a vertical gas–liquid flow: Bouncing, sliding and bubble deformations.* Chemical engineering science, 2007. 62(6): p. 1591-1605.
21. Jeong, H., Park, H. *Near-wall rising behaviour of a deformable bubble at high Reynolds number.* Journal of Fluid Mechanics, 2015. 771: p. 564.

22. Takemura, F., Magnaudet, J. *The transverse force on clean and contaminated bubbles rising near a vertical wall at moderate Reynolds number.* Journal of Fluid Mechanics, 2003. 495: p. 235.
23. Takemura, F. et al. *Drag and lift forces on a bubble rising near a vertical wall in a viscous liquid.* Journal of Fluid Mechanics, 2002. 461: p. 277.
24. Moctezuma, M., Lima-Ochoterena, R., Zenit, R. *Velocity fluctuations resulting from the interaction of a bubble with a vertical wall.* Physics of Fluids, 2005. 17(9): p. 098106.
25. Sugiyama, K., Takemura, F. *On the lateral migration of a slightly deformed bubble rising near a vertical plane wall.* Journal of Fluid Mechanics, 2010. 662: p. 209-231.
26. Lee, J., Park, H. *Wake structures behind an oscillating bubble rising close to a vertical wall.* International Journal of Multiphase Flow, 2017. 91: p. 225-242.
27. Legendre, D., Daniel, C., Guiraud, P. *Experimental study of a drop bouncing on a wall in a liquid.* Physics of Fluids, 2005. 17(9): p. 097105.
28. Zenit, R., Legendre, D. *The coefficient of restitution for air bubbles colliding against solid walls in viscous liquids.* Physics of Fluids, 2009. 21(8): p. 083306.
29. Pelletier, E., Béguin, C., Étienne, S. *Experiments of air bubbles impacting a rigid wall in tap water.* Physics of Fluids, 2015. 27(12): p. 123302.
30. Manica, R., Klaseboer, E., Chan, D.Y. *Force balance model for bubble rise, impact, and bounce from solid surfaces.* Langmuir, 2015. 31(24): p. 6763-6772.
31. Klaseboer, E. et al. *Model and experiments of a drop impinging on an immersed wall.* Physics of Fluids, 2001. 13(1): p. 45-57.
32. Tsao, H.K., Koch, D.L. *Observations of high Reynolds number bubbles interacting with a rigid wall.* Physics of Fluids, 1997. 9(1): p. 44-56.
33. Masliyah, J., Jauhari, R., Gray, M. *Drag coefficients for air bubbles rising along an inclined surface.* Chemical engineering science, 1994. 49(12): p. 1905-1911.
34. Podvin, B. et al. *Model and experimental visualizations of the interaction of a bubble with an inclined wall.* Chemical Engineering Science, 2008. 63(7): p. 1914-1928.
35. Barbosa, C., Legendre, D., Zenit, R. *Conditions for the sliding-bouncing transition for the interaction of a bubble with an inclined wall.* Physical Review Fluids, 2016. 1(3): p. 032201.
36. Dubois, C., Duchesne, A., Caps, H. *Between inertia and viscous effects: Sliding bubbles beneath an inclined plane.* Europhysics Letters, 2016. 115(4): p. 44001.
37. Aussillous, P., Quéré, D. *Bubbles creeping in a viscous liquid along a slightly inclined plane.* Europhysics Letters, 2002. 59(3): p. 370.
38. Barbosa, C., Legendre, D., Zenit, R. *Sliding motion of a bubble against an inclined wall from moderate to high bubble Reynolds number.* Physical Review Fluids, 2019. 4(4): p. 043602.
39. Cox, R.G., Hsu, S.K. *The lateral migration of solid particles in a laminar flow near a plane.* International Journal of Multiphase Flow, 1977. 3(3): p. 201-222.
40. Vasseur, P., Cox, R.G. *The lateral migration of spherical particles sedimenting in a stagnant bounded fluid.* Journal of Fluid Mechanics, 1977. 80(3): p. 561-591.
41. Magnaudet, J., Takagi, S., Legendre, D. *Drag, deformation and lateral migration of a buoyant drop moving near a wall.* Journal of Fluid Mechanics, 2003. 476: p. 115-157.
42. Milne-Thomson, L.M. *Theoretical hydrodynamics*. 1996. Courier Corporation.
43. Joseph, G. et al. *Particle-wall collisions in a viscous fluid.* Journal of Fluid Mechanics, 2001. 433: p. 329-346.
44. Legendre, D. et al. *A note on the modelling of the bouncing of spherical drops or solid spheres on a wall in viscous fluid.* Chemical engineering science, 2006. 61(11): p. 3543-3549.
45. GraceJ, R., Wairegi, T., NguyenT, H. *Shapes and velocities of single drops and bubbles moving freely through immiscible liquids.* Physics, 1976.
46. Moore, D.W. *The velocity of rise of distorted gas bubbles in a liquid of small viscosity.* Journal of Fluid Mechanics, 1965. 23(4): p. 749-766.
47. Cano-Lozano, J.C. et al. *Paths and wakes of deformable nearly spheroidal rising bubbles close to*

the transition to path instability. Physical Review Fluids, 2016. 1(5): p. 053604.
48. Figueroa-Espinoza, B., Zenit, R., Legendre, D. *The effect of confinement on the motion of a single clean bubble.* Journal of Fluid Mechanics, 2008. 616: p. 419-443.
49. Melville, W.K. *Wave modulation and breakdown.* Journal of Fluid Mechanics, 1983. 128: p. 489-506.
50. Lamb, H. *Hydrodynamics.* 1945. Dover, New York.
51. Shew, W.L., Poncet, S., Pinton, J.F. *Force measurements on rising bubbles.* Journal of Fluid Mechanics, 2006. 569: p. 51-60.
52. Zhang, J., Ni, M.J. *What happens to the vortex structures when the rising bubble transits from zigzag to spiral?* Journal of Fluid Mechanics, 2017. 828: p. 353-373.

General conclusion and recommendations

General conclusion

Gas-liquid as well as gas-liquid-solid bubble column reactors are extensively used in oil refineries and gas treatment plants. They are used especially in chemical processes involving reactions. In recent years, the offshore oil and gas industry has been increasingly interested in extending the application of reactors for floating platforms such as floating production storage and offloading (FPSO) units. However, the challenges of marine currents and waves influence the performance of reactors installed onboard marine units. To maintain the capacity and product specifications in such reactors, prediction of their performance deviations with respect to the static ones is essential. Particularly, investigation on single bubble flow behavior in a moving column will provide a basis to understand the more complex behavior in multi-bubble flow in a bubble column reactor operating in floating conditions.

In this study, the three-dimensional trajectory data, reconstructed using two synchronized high-speed video cameras, provided a full description of the bubble rise at high Reynolds numbers, and moderate Weber numbers.

The behavior of single air bubbles experiencing bubble-wall collisions in an inclined column (0-15^{o} tilts), filled with different liquids (Morton numbers, Mo: $10^{-7}, 10^{-9}, 10^{-11}$), was analyzed for three bubble rise motions, namely, rectilinear, zigzag, and spiral paths.

The variations in bubble trajectories were analyzed. It was shown that the helicoidal rising bubble maintains two out-of-phase modes of oscillations, with $\pi/2$ phase lag while bouncing beneath the wall. The bubble-wall contact increased the frequency of bubble oscillations in the direction of inclination of the column. However, the frequency of oscillations tangent to the wall remained the same as for the (wall-) free rising bubbles, i.e., 39 $\mathrm{rd/s}$ for both zigzag and spiral bubble paths. The amplitude of the wake-induced in-plane oscillations of the bubbles rising beneath the wall was measured for the zigzagging bubble. The effect of bubble-wall collisions on the amplitude of the wake-induced in-plane oscillations was marginal.

Restitution coefficients calculated for helicoidal rising bubble credited some predictive confidence for a correlation established on the basis of liquid droplets impacting horizontal walls.

Moreover, comparing the energy components for bubbles rising in helical and zigzag motions showed that the two lateral components of the kinetic energy (normal and tangent to wall) had rather equal contributions within the total kinetic energy budget of spirally rising bubbles. However, the kinetic energy contribution of the normal component of zigzagging bubbles was negligible.

Recommendation for future work

Bubble column reactors have a broad application in chemical and petrochemical industries. Several studies have been performed on their hydrodynamics and mass transfer characteristics. Despite their growing application in offshore oil and gas industry, and especially on FPSO units, little attention has been devoted to analyzing their performance under harsh environmental condition due to the wind and marine currents.

This study was limited to single bubble rising in static inclined column. It is recommended to use a hexapod ship motion emulator to simulate different motions to mimic FPSO movements.

Due to the strong effect of column hydrodynamics on mass transfer in bubble column reactors, mass transfer characteristics in terms of gas-liquid interfacial area and volumetric mass transfer coefficient could be investigated.

The effect of column motion on bubble coalescence, in both rectilinear and zigzag behavior of bubble, could be investigated. This provides a basis for understanding a factor of mass transfer deviations in offshore-installed bubble columns comparing with the stationary (onshore) unit.

The probable liquid secondary flow or liquid circulation resulted from the vessel rotational movements, may impose different effects on bubble detachment hydrodynamics or rising behavior in various locations of the columns' cross-section. The position of the gas orifice within the axis orthogonal or parallel to the column motion could provide a deeper understanding on the industrial reactors equipped with spargers that gas orifices are distributed at different positions in the bottom of the column.

There are extensive numerical studies on single bubble rising and bubble coalescence in still liquid. Two- phase flow dynamics and contribution of various forces have been widely analyzed to improve closures for continuum flow models in static reactors. However, there does not exist any

numerical investigation on floating bubble column reactors at the bubble-scale nor at the reactor scale. Consequently, developing a computational model to evaluate the effect of column motions on single bubble dynamics and understand the liquid flow field around the bubble, and the changes in involved forces, which govern the different rising behavior of single bubble in moving column is recommended.

General Bibliography

1. Cullinane, J.T., Yeh, N., Grave, E. *Effects of tower motion on packing efficiency*. 143766 SPE Conference Paper. 2011. Brazil.
2. Reay, D., Ramshaw, C., Harvey, A. *Process Intensification: Engineering for efficiency, sustainability and flexibility*. 2013. Butterworth-Heinemann.
3. Motamed Dashliborun, A. *Performance of multiphase packed-bed reactors and scrubbers on offshore floating platforms: hydrodynamics, chemical reaction, CFD modeling and simulation*. 2018, PhD Thesis, Universite Laval.
4. Markus Duss, M.R. *Columns subject to motion: Maldistribution sensitivity and susceptibility*, in *10th International Conference on DISTILLATION & ABSORPTION*. 2014: Friedrichshafen · Germany.
5. Horoun, Y., Raynal, L., Alix, P. *Distributor tray for offshore gas/liquid contact column*. 2015: US Patent US9120064B2.
6. Kantarci, N., Borak, F., Ulgen, K.O. *Bubble column reactors.* Process biochemistry, 2005. 40(7): p. 2263-2283.
7. Assima, G.P. et al. *Capacitance wire mesh imaging of bubbly flows for offshore treatment applications.* Flow Measurement and Instrumentation, 2015. 45: p. 298-307.
8. Deen, N.G. et al. *Bubble Columns*, in *Ullmann's Encyclopedia of Industrial Chemistry. Weinheim* 2010, Wiley-VCH Verlag.
9. Besagni, G., Inzoli, F., Ziegenhein, T. *Two-Phase Bubble Columns: A Comprehensive Review.* ChemEngineering, 2018. 2(2): p. 13.
10. Shu, S. et al. *Multiscale Multiphase Phenomena in Bubble Column Reactors: A Review*. Renewable Energy, 2019.
11. Syed, A.H. *Modeling of Two & Three Phases Bubble Column Modélisation dΓune Colonne à bulles Biphasique et Triphasique*. 2017, PhD Thesis, Université de Sherbrooke.
12. Deckwer, W.D., Burckhart, R., Zoll, G. *Mixing and mass transfer in tall bubble columns.* Chemical Engineering Science, 1974. 29(11): p. 2177-2188.
13. Krishna, R. et al. *Influence of increased gas density on hydrodynamics of bubble-column reactors.* AIChE journal, 1994. 40(1): p. 112-119.
14. Liu, L. et al. *Experimental studies on the terminal velocity of air bubbles in water and glycerol aqueous solution.* Experimental Thermal and Fluid Science, 2016. 78: p. 254-265.
15. Magnaudet, J., Eames, I. *The motion of high-Reynolds-number bubbles in inhomogeneous flows.* Annual Review of Fluid Mechanics, 2000. 32(1): p. 659-708.
16. Batchelor, G. *An introduction to fluid dynamics. 1967.* Cambridge,: UP xviii, 1967. 615.
17. N. M. Aybers, A.T. *The motion of gas bubbles rising through stagnant liquid.* Heat and Substance Transfer, 1969. 2: p. 118-128.
18. Levich, V.G. *Physicochemical Hydrodynamics Prentice-Hall.* Englewood Cliffs, NJ, 1962. 115.
19. Kang, I., Leal, L. *The drag coefficient for a spherical bubble in a uniform streaming flow.* The

Physics of fluids, 1988. 31(2): p. 233-237.
20. Moore, D. *The rise of a gas bubble in a viscous liquid.* Journal of Fluid Mechanics, 1959. 6(1): p. 113-130.
21. Moore, D. *The boundary layer on a spherical gas bubble.* Journal of Fluid Mechanics, 1963. 16(2): p. 161-176.
22. Moore, D. *The velocity of rise of distorted gas bubbles in a liquid of small viscosity.* Journal of Fluid Mechanics, 1965. 23(4): p. 749-766.
23. Duineveld, P. *The rise velocity and shape of bubbles in pure water at high Reynolds number.* Journal of Fluid Mechanics, 1995. 292: p. 325-332.
24. Maxworthy, T. et al. *Experiments on the rise of air bubbles in clean viscous liquids.* Journal of fluid mechanics, 1996. 321: p. 421-441.
25. Dijkhuizen, W. et al. *DNS of gas bubbles behaviour using an improved 3D front tracking model—Drag force on isolated bubbles and comparison with experiments.* Chemical Engineering Science, 2010. 65(4): p. 1415-1426.
26. Hartunian, R.A., Sears, W. *On the instability of small gas bubbles moving uniformly in various liquids.* Journal of Fluid Mechanics, 1957. 3(1): p. 27-47.
27. Liu, L., Yan, H., Zhao, G. *Experimental studies on the shape and motion of air bubbles in viscous liquids.* Experimental Thermal and Fluid Science, 2015. 62: p. 109-121.
28. Ford, B., Loth, E. *Forces on ellipsoidal bubbles in a turbulent shear layer.* Physics of Fluids, 1998. 10(1): p. 178-188.
29. Hadamard, J. *Mouvement permanent lent d'une sphère liquid et visqueuse dans un liquide visqueux.* CR Hebd. Seances Acad. Sci. Paris, 1911. 152: p. 1735-1738.
30. Tomiyama, A. et al. *Terminal velocity of single bubbles in surface tension force dominant regime.* International journal of multiphase flow, 2002. 28(9): p. 1497-1519.
31. Zhang, Y., Finch, J. *A note on single bubble motion in surfactant solutions.* Journal of Fluid Mechanics, 2001. 429: p. 63-66.
32. Celata, G.P. et al. *Effect of gas injection mode and purity of liquid on bubble rising in two-component systems.* Experimental Thermal and Fluid Science, 2006. 31(1): p. 37-53.
33. Sakamoto, H., Haniu, H. *The formation mechanism and shedding frequency of vortices from a sphere in uniform shear flow.* Journal of Fluid Mechanics, 1995. 287: p. 151-171.
34. Rusche, H. *Computational fluid dynamics of dispersed two-phase flows at high phase fractions*. 2003, Imperial College London (University of London).
35. Lindt, J.T. *On the periodic nature of the drag on a rising bubble.* Chemical Engineering Science, 1972. 27(10): p. 1775-1781.
36. R. Clift, J.R.G., and M. E. Weber. *Bubbles, drops, and particles*. 1978. New York ; London. Academic Press.
37. Ngachin, M. *Simulation of rising bubbles dynamics using the lattice Boltzmann method*, in *Geosciences*. 2011, Florida International University.
38. Xu, X. et al. *Rising behavior of single bubble in infinite stagnant non-Newtonian liquids.* International Journal of Multiphase Flow, 2017. 95: p. 84-90.
39. Joshi, J.B. et al. *Bubble generated turbulence and direct numerical simulations.* Chemical Engineering Science, 2017. 157: p. 26-75.
40. Tripathi, M.K., Sahu, K.C., Govindarajan, R. *Dynamics of an initially spherical bubble rising in quiescent liquid.* Nature Communications, 2015. 6: p. 6268.
41. Joshi, J.B. et al. *Bubble generated turbulence and direct numerical simulations.* Chemical Engineering Science, 2017. 157: p. 26-75.
42. Brücker, C. *Structure and dynamics of the wake of bubbles and its relevance for bubble interaction.* Physics of Fluids, 1999. 11(7): p. 1781-1796.
43. Mougin, G., Magnaudet, J. *The generalized Kirchhoff equations and their application to the interaction between a rigid body and an arbitrary time-dependent viscous flow.* International

Journal of Multiphase Flow, 2002. 28(11): p. 1837-1851.
44. Mikaelian, D. et al. *A new experimental method to analyze the dynamics and the morphology of bubbles in liquids: Application to single ellipsoidal bubbles.* Chemical Engineering Science, 2013. 100: p. 529-538.
45. Batchelor, G.K. *The stability of a large gas bubble rising through liquid.* Journal of Fluid Mechanics, 1987. 184: p. 399-422.
46. Veldhuis, C. *Leonardo's paradox: Path and shape instabilities of particles and bubbles.* 2007.
47. De Vries, J., Luther, S., Lohse, D. *Induced bubble shape oscillations and their impact on the rise velocity.* The European Physical Journal B-Condensed Matter and Complex Systems, 2002. 29(3): p. 503-509.
48. Mougin, G., Magnaudet, J.J.J.o.F.M. *Wake-induced forces and torques on a zigzagging/spiralling bubble.* Journal of Fluid Mechanics, 2006. 567: p. 185.
49. Cano-Lozano, J.C., Bohorquez, P., Martínez-Bazán, C. *Wake instability of a fixed axisymmetric bubble of realistic shape.* International Journal of Multiphase Flow, 2013. 51: p. 11-21.
50. Lain, S., Bröder, D., Sommerfeld, M. *Experimental and numerical studies of the hydrodynamics in a bubble column.* Chemical Engineering Science, 1999. 54(21): p. 4913-4920.
51. Ellingsen, K., Risso, F. *On the rise of an ellipsoidal bubble in water: oscillatory paths and liquid-induced velocity.* Journal of Fluid Mechanics, 2001. 440: p. 235-268.
52. Babadagli, T., Boluk, Y. *Oil recovery performances of surfactant solutions by capillary imbibition.* Journal of colloid and interface science, 2005. 282(1): p. 162-175.
53. Wellek, R., Agrawal, A., Skelland, A. *Shape of liquid drops moving in liquid media.* AIChE Journal, 1966. 12(5): p. 854-862.
54. Magnaudet, J.J. *The forces acting on bubbles and rigid particles*. ASME Fluids Engineering Division Summer Meeting, FEDSM. 1997.
55. Lohse, D., Prosperetti, A. *Controlling bubbles.* Journal of physics: Condensed matter, 2002. 15(1): p. S415.
56. Shew, W.L., Poncet, S., Pinton, J.-F. *Force measurements on rising bubbles.* Journal of Fluid Mechanics, 2006. 569: p. 51-60.
57. Shew, W.L., Pinton, J.-F. *Dynamical model of bubble path instability.* Physical review letters, 2006. 97(14): p. 144508.
58. de Vries, A.W.G., Biesheuvel, A., van Wijngaarden, L. *Notes on the path and wake of a gas bubble rising in pure water.* International Journal of Multiphase Flow, 2002. 28(11): p. 1823-1835.
59. Sugioka, K.-i., Tsukada, T. *Direct numerical simulations of drag and lift forces acting on a spherical bubble near a plane wall.* International Journal of Multiphase Flow, 2015. 71: p. 32-37.
60. Lee, J., Park, H. *Wake structures behind an oscillating bubble rising close to a vertical wall.* International Journal of Multiphase Flow, 2017. 91: p. 225-242.
61. Jeong, H., Park, H. *Near-wall rising behaviour of a deformable bubble at high Reynolds number.* Journal of Fluid Mechanics, 2015. 771: p. 564.
62. Pelletier, E., Béguin, C., Étienne, S. *Experiments of air bubbles impacting a rigid wall in tap water.* Physics of Fluids, 2015. 27(12): p. 123302.
63. Masliyah, J., Jauhari, R., Gray, M. *Drag coefficients for air bubbles rising along an inclined surface.* Chemical engineering science, 1994. 49(12): p. 1905-1911.
64. Masliyah J. H., J., R., Gray M. R. *Rise velocities of air bubbles along an inclined surface*, in *Mixed-Flow Hydrodynamics*, N.P. Cheremisinoff, Editor. 1996, Gulf Publishing: Houston, Texas.
65. Drechsler, C. et al. *Bubble Behavior in Marine Applications of Bubble Columns: Case of Ellipsoidal Bubbles in Slanted and Rolling Columns.* Industrial & Engineering Chemistry Research, 2019. 58(6): p. 2343-2355.
66. Yamaguchi, T., Iguchi, M., Uemura, T. *Behavior of a small single bubble rising in a rotating flow field.* Experimental mechanics, 2004. 44(5): p. 533-540.
67. Li, Z. et al. *Experimental investigation of single small bubble motion in linear shear flow in water.*

Nuclear Engineering and Design, 2016. 305: p. 334-346.
68. Legendre, D., Daniel, C., Guiraud, P. *Experimental study of a drop bouncing on a wall in a liquid.* Physics of Fluids, 2005. 17(9): p. 097105.
69. Van Nierop, E.A. et al. *Drag and lift forces on bubbles in a rotating flow.* Journal of fluid mechanics, 2007. 571: p. 439-454.
70. Rastello, M., Marié, J.-L., Lance, M. *Drag and lift forces on clean spherical and ellipsoidal bubbles in a solid-body rotating flow.* Journal of Fluid Mechanics, 2011. 682: p. 434-459.
71. Tomiyama, A. et al. *Transverse migration of single bubbles in simple shear flows.* Chemical Engineering Science, 2002. 57(11): p. 1849-1858.
72. Zahedi, P. et al. *Influence of fluid properties on bubble formation, detachment, rising and collapse; Investigation using volume of fluid method.* Korean Journal of Chemical Engineering, 2014. 31(8): p. 1349-1361.
73. Michaelides, E.E., Crowe, C. (Ed.), Schwarzkopf, J. (Ed.). *Multiphase Flow Handbook*. 2016. Boca Raton. CRC Press.
74. Laín, S. et al. *Modelling hydrodynamics and turbulence in a bubble column using the Euler–Lagrange procedure.* International Journal of Multiphase Flow, 2002. 28(8): p. 1381-1407.
75. Delnoij, E. et al. *Dynamic simulation of dispersed gas-liquid two-phase flow using a discrete bubble model.* Chemical engineering science, 1997. 52(9): p. 1429-1458.
76. Delnoij, E., Kuipers, J.A.M., van Swaaij, W.P.M. *Dynamic simulation of gas-liquid two-phase flow: effect of column aspect ratio on the flow structure.* Chemical Engineering Science, 1997. 52(21): p. 3759-3772.
77. Lapin, A., Lübbert, A. *Numerical simulation of the dynamics of two-phase gas—liquid flows in bubble columns.* Chemical Engineering Science, 1994. 49(21): p. 3661-3674.
78. Sokolichin, A., Eigenberger, G. *Gas—liquid flow in bubble columns and loop reactors: Part I. Detailed modelling and numerical simulation.* Chemical Engineering Science, 1994. 49(24, Part 2): p. 5735-5746.
79. van Sint Annaland, M., Deen, N.G., Kuipers, J.A.M. *Numerical simulation of gas bubbles behaviour using a three-dimensional volume of fluid method.* Chemical Engineering Science, 2005. 60(11): p. 2999-3011.
80. Albadawi, A. *On the assessment of numerical interface capturing methods for two fluid flow applications*. 2014, Dublin City University.
81. Sankaranarayanan, K. et al. *Analysis of drag and virtual mass forces in bubbly suspensions using an implicit formulation of the lattice Boltzmann method.* Journal of Fluid Mechanics, 2002. 452: p. 61-96.
82. Delnoij, E., Kuipers, J.A.M., van Swaaij, W.P.M. *A three-dimensional CFD model for gas–liquid bubble columns.* Chemical Engineering Science, 1999. 54(13): p. 2217-2226.
83. Krishna, R. et al. *Rise velocity of a swarm of large gas bubbles in liquids.* Chemical Engineering Science, 1999. 54(2): p. 171-183.
84. Hassan, N.M.S., Khan, M.M.K., Rasul, M.G. *A modelling and experimental study of the bubble trajectory in a non-Newtonian crystal suspension.* Fluid Dynamics Research, 2010. 42(6): p. 065502.
85. Ma, D. et al. *Two-dimensional volume of fluid simulation studies on single bubble formation and dynamics in bubble columns.* Chemical Engineering Science, 2012. 72: p. 61-77.
86. Zhang, K. et al. *Computational Fluid Dynamics (CFD) Modeling of Bubble Dynamics in the Aluminum Smelting Process.* Industrial & Engineering Chemistry Research, 2013. 52(33): p. 11378-11390.
87. Tomiyama, A. et al. *Numerical analysis of bubble motion with the VOF method.* Nuclear Engineering and Design, 1993. 141(1): p. 69-82.
88. Xu, Y., Ersson, M., Jönsson, P. *Numerical Simulation of Single Argon Bubble Rising in Molten Metal Under a Laminar Flow.* steel research international, 2015. 86(11): p. 1289-1297.

89. Pourtousi, M. et al. *Methane bubble formation and dynamics in a rectangular bubble column: A CFD study.* Chemometrics and Intelligent Laboratory Systems, 2015. 147: p. 111-120.
90. Wang, G. et al. *The Motion of Single Bubble and Interactions between Two Bubbles in Liquid Steel.* ISIJ International, 2017. 57(5): p. 805-813.
91. Zhongchun, L. et al. *Numerical investigation on lateral migration and lift force of single bubble in simple shear flow in low viscosity fluid using volume of fluid method.* Nuclear Engineering and Design, 2014. 274: p. 154-163.
92. Wang, S. et al. *The dynamics of rising oil-coated bubbles: experiments and simulations.* Soft Matter, 2018. 14(14): p. 2724-2734.
93. Dijkhuizen, W. et al. *Numerical investigation of closures for interface forces acting on single air-bubbles in water using Volume of Fluid and Front Tracking models.* Chemical Engineering Science, 2005. 60(22): p. 6169-6175.
94. Cano-Lozano, J.C. et al. *The use of Volume of Fluid technique to analyze multiphase flows: Specific case of bubble rising in still liquids.* Applied Mathematical Modelling, 2015. 39(12): p. 3290-3305.
95. Anwar, S. *Lattice Boltzmann modeling of buoyant rise of single and multiple bubbles.* Computers & Fluids, 2013. 88: p. 430-439.
96. Huang, H., Wang, L., Lu, X.-y. *Evaluation of three lattice Boltzmann models for multiphase flows in porous media.* Computers & Mathematics with Applications, 2011. 61(12): p. 3606-3617.
97. Zheng, H.W., Shu, C., Chew, Y.T. *A lattice Boltzmann model for multiphase flows with large density ratio.* Journal of Computational Physics, 2006. 218(1): p. 353-371.
98. morning, R.M.G.G.F.I.E.C.J.G. *Validation of a ghost fluid method in a tree-based adaptive volume of fluid for two-phase heat and mass transfer*, in *8th International Conference of Boiling and Condensation Heat Transfer*. 2012: Lausanne, Switzerland. p. 1-11.
99. Gumulya, M. et al. *Characteristics of energy production and dissipation around a bubble rising in water.* Chemical Engineering Science, 2019. 193: p. 38-52.
100. Gumulya, M. et al. *Interaction of bubbles rising inline in quiescent liquid.* Chemical Engineering Science, 2017. 166: p. 1-10.
101. Nichita, B.A., Zun, I., Thome, J.R. *A Level Set Method Coupled With a Volume of Fluid Method for Modeling of Gas-Liquid Interface in Bubbly Flow.* Journal of Fluids Engineering, 2010. 132(8): p. 081302-081302-15.
102. Brackbill, J.U., Kothe, D.B., Zemach, C. *A continuum method for modeling surface tension.* Journal of computational physics, 1992. 100(2): p. 335-354.
103. Abadie, T., Aubin, J., Legendre, D. *On the combined effects of surface tension force calculation and interface advection on spurious currents within Volume of Fluid and Level Set frameworks.* Journal of Computational Physics, 2015. 297: p. 611-636.
104. Popinet, S. *Numerical models of surface tension.* Annual Review of Fluid Mechanics, 2018. 50: p. 49-75.
105. Lafaurie, B. et al. *Modelling merging and fragmentation in multiphase flows with SURFER.* Journal of Computational Physics, 1994. 113(1): p. 134-147.
106. Samkhaniani, N., Ansari, M. *Numerical simulation of bubble condensation using CF-VOF.* Progress in Nuclear Energy, 2016. 89: p. 120-131.
107. Vachaparambil, K.J., Einarsrud, K.E. *Comparison of Surface Tension Models for the Volume of Fluid Method.* Processes, 2019. 7(8): p. 542.
108. Raeini, A.Q., Blunt, M.J., Bijeljic, B. *Modelling two-phase flow in porous media at the pore scale using the volume-of-fluid method.* Journal of Computational Physics, 2012. 231(17): p. 5653-5668.
109. Pavuluri, S., Maes, J., Doster, F. *Spontaneous imbibition in a microchannel: Analytical solution and assessment of volume of fluid formulations.* Microfluidics and Nanofluidics, 2018. 22(8): p. 90.
110. Abadie, T. *Hydrodynamics of gas-liquid Taylor flow in microchannels*. 2013, PhD Thesis, Universite de Toulouse.

111. Zalesak, S.T. *Fully multidimensional flux-corrected transport algorithms for fluids.* Journal of computational physics, 1979. 31(3): p. 335-362.
112. Ruen-ngam, D. et al. *Influence of salinity on bubble size distribution and gas–liquid mass transfer in airlift contactors.* Chemical Engineering Journal, 2008. 141(1): p. 222-232.
113. Koebe, D.-I.M. *Numerische Simulation aufsteigender Blasen mit und ohne Stoffaustausch mittels der Volume of Fluid (VOF) Methode.* 2004.
114. Rabha, S.S., Buwa, V.V. *Volume-of-fluid (VOF) simulations of rise of single/multiple bubbles in sheared liquids.* Chemical Engineering Science, 2010. 65(1): p. 527-537.
115. Inc., A.F. *ANSYS Fluent 12.0 User's Guide*. 2009.
116. Atta, A. et al. *Co-current descending two-phase flows in inclined packed beds: experiments versus simulations.* The Canadian Journal of Chemical Engineering, 2010. 88(5): p. 742-750.
117. Motamed Dashliborun, A., Larachi, F. *CFD study and experimental validation of multiphase packed bed hydrodynamics in the context of Rolling Sea conditions.* AIChE Journal, 2019. 65(1): p. 385-397.
118. Besagni, G., Inzoli, F., Ziegenhein, T. *Two-Phase Bubble Columns: A Comprehensive Review.* ChemEngineering, 2018. 2(2): p. 13.
119. Shu, S. et al. *Multiscale multiphase phenomena in bubble column reactors: A review.* Renewable Energy, 2019. 141: p. 613-631.
120. Zhou, W. *Path instabilities of spheres, spheroids and bubbles*. 2016, Université de Strasbourg: Strasbourg, France.
121. Ellingsen, K., Risso, F. *On the rise of an ellipsoidal bubble in water: oscillatory paths and liquid-induced velocity.* Journal of Fluid Mechanics, 2001. 440: p. 235.
122. Kong, G. et al. *Hydrodynamic interaction of bubbles rising side-by-side in viscous liquids.* Experiments in Fluids, 2019. 60(10): p. 1-15.
123. Clift, R., Grace, J.R., Weber, M.E. *Bubbles, drops, and particles.* 2005.
124. Saffman, P.G. *On the rise of small air bubbles in water.* Journal of Fluid Mechanics, 1956. 1(3): p. 249-275.
125. Aybers, N., Tapucu, A. *The motion of gas bubbles rising through stagnant liquid.* Wärme-und Stoffübertragung, 1969. 2(2): p. 118-128.
126. Brücker, C. *Structure and dynamics of the wake of bubbles and its relevance for bubble interaction.* Physics of fluids, 1999. 11(7): p. 1781-1796.
127. Mougin, G., Magnaudet, J. *Path instability of a rising bubble.* Physical review letters, 2001. 88(1): p. 014502.
128. de Vries, A.W.G., Biesheuvel, A., Van Wijngaarden, L. *Notes on the path and wake of a gas bubble rising in pure water.* International journal of multiphase flow, 2002. 28(11): p. 1823-1835.
129. Zenit, R., Magnaudet, J. *Path instability of rising spheroidal air bubbles: a shape-controlled process.* Physics of Fluids, 2008. 20(6): p. 061702.
130. Zenit, R., Magnaudet, J. *Measurements of the streamwise vorticity in the wake of an oscillating bubble.* International Journal of Multiphase Flow, 2009. 35(2): p. 195-203.
131. Magnaudet, J., Mougin, G. *Wake instability of a fixed spheroidal bubble.* Journal of Fluid Mechanics, 2007. 572: p. 311.
132. Cano-Lozano, J., Bohorquez, P., Martínez-Bazán, C. *Wake instability of a fixed axisymmetric bubble of realistic shape.* International journal of multiphase flow, 2013. 51: p. 11-21.
133. Magnaudet, J., Eames, I. *The motion of high-Reynolds-number bubbles in inhomogeneous flows.* Annual Review of Fluid Mechanics, 2000. 32(1): p. 659-708.
134. Tomiyama, A. et al. *Terminal velocity of single bubbles in surface tension force dominant regime.* International journal of multiphase flow, 2002. 28(9): p. 1497-1519.
135. Wu, M., Gharib, M. *Experimental studies on the shape and path of small air bubbles rising in clean water.* Physics of fluids, 2002. 14(7): p. L49-L52.
136. Liu, L., Yan, H., Zhao, G. *Experimental studies on the shape and motion of air bubbles in viscous*

liquids. Experimental Thermal, 2015. 62: p. 109-121.
137. Zaruba, A. et al. *Bubble-wall interactions in a vertical gas–liquid flow: Bouncing, sliding and bubble deformations.* Chemical engineering science, 2007. 62(6): p. 1591-1605.
138. Jeong, H., Park, H. *Near-wall rising behaviour of a deformable bubble at high Reynolds number.* Journal of Fluid Mechanics, 2015. 771: p. 564.
139. Takemura, F., Magnaudet, J. *The transverse force on clean and contaminated bubbles rising near a vertical wall at moderate Reynolds number.* Journal of Fluid Mechanics, 2003. 495: p. 235.
140. Takemura, F. et al. *Drag and lift forces on a bubble rising near a vertical wall in a viscous liquid.* Journal of Fluid Mechanics, 2002. 461: p. 277.
141. Moctezuma, M., Lima-Ochoterena, R., Zenit, R. *Velocity fluctuations resulting from the interaction of a bubble with a vertical wall.* Physics of Fluids, 2005. 17(9): p. 098106.
142. Sugiyama, K., Takemura, F. *On the lateral migration of a slightly deformed bubble rising near a vertical plane wall.* Journal of Fluid Mechanics, 2010. 662: p. 209-231.
143. Lee, J., Park, H. *Wake structures behind an oscillating bubble rising close to a vertical wall.* International Journal of Multiphase Flow, 2017. 91: p. 225-242.
144. Legendre, D., Daniel, C., Guiraud, P. *Experimental study of a drop bouncing on a wall in a liquid.* Physics of Fluids, 2005. 17(9): p. 097105.
145. Zenit, R., Legendre, D. *The coefficient of restitution for air bubbles colliding against solid walls in viscous liquids.* Physics of Fluids, 2009. 21(8): p. 083306.
146. Pelletier, E., Béguin, C., Étienne, S. *Experiments of air bubbles impacting a rigid wall in tap water.* Physics of Fluids, 2015. 27(12): p. 123302.
147. Manica, R., Klaseboer, E., Chan, D.Y. *Force balance model for bubble rise, impact, and bounce from solid surfaces.* Langmuir, 2015. 31(24): p. 6763-6772.
148. Klaseboer, E. et al. *Model and experiments of a drop impinging on an immersed wall.* Physics of Fluids, 2001. 13(1): p. 45-57.
149. Tsao, H.K., Koch, D.L. *Observations of high Reynolds number bubbles interacting with a rigid wall.* Physics of Fluids, 1997. 9(1): p. 44-56.
150. Masliyah, J., Jauhari, R., Gray, M. *Drag coefficients for air bubbles rising along an inclined surface.* Chemical engineering science, 1994. 49(12): p. 1905-1911.
151. Podvin, B. et al. *Model and experimental visualizations of the interaction of a bubble with an inclined wall.* Chemical Engineering Science, 2008. 63(7): p. 1914-1928.
152. Barbosa, C., Legendre, D., Zenit, R. *Conditions for the sliding-bouncing transition for the interaction of a bubble with an inclined wall.* Physical Review Fluids, 2016. 1(3): p. 032201.
153. Dubois, C., Duchesne, A., Caps, H. *Between inertia and viscous effects: Sliding bubbles beneath an inclined plane.* Europhysics Letters, 2016. 115(4): p. 44001.
154. Aussillous, P., Quéré, D. *Bubbles creeping in a viscous liquid along a slightly inclined plane.* Europhysics Letters, 2002. 59(3): p. 370.
155. Barbosa, C., Legendre, D., Zenit, R. *Sliding motion of a bubble against an inclined wall from moderate to high bubble Reynolds number.* Physical Review Fluids, 2019. 4(4): p. 043602.
156. Cox, R.G., Hsu, S.K. *The lateral migration of solid particles in a laminar flow near a plane.* International Journal of Multiphase Flow, 1977. 3(3): p. 201-222.
157. Vasseur, P., Cox, R.G. *The lateral migration of spherical particles sedimenting in a stagnant bounded fluid.* Journal of Fluid Mechanics, 1977. 80(3): p. 561-591.
158. Magnaudet, J., Takagi, S., Legendre, D. *Drag, deformation and lateral migration of a buoyant drop moving near a wall.* Journal of Fluid Mechanics, 2003. 476: p. 115-157.
159. Milne-Thomson, L.M. *Theoretical hydrodynamics*. 1996. Courier Corporation.
160. Joseph, G. et al. *Particle-wall collisions in a viscous fluid.* Journal of Fluid Mechanics, 2001. 433: p. 329-346.
161. Legendre, D. et al. *A note on the modelling of the bouncing of spherical drops or solid spheres on a wall in viscous fluid.* Chemical engineering science, 2006. 61(11): p. 3543-3549.

162. GraceJ, R., Wairegi, T., NguyenT, H. *Shapes and velocities of single drops and bubbles moving freely through immiscible liquids.* Physics, 1976.
163. Moore, D.W. *The velocity of rise of distorted gas bubbles in a liquid of small viscosity.* Journal of Fluid Mechanics, 1965. 23(4): p. 749-766.
164. Cano-Lozano, J.C. et al. *Paths and wakes of deformable nearly spheroidal rising bubbles close to the transition to path instability.* Physical Review Fluids, 2016. 1(5): p. 053604.
165. Figueroa-Espinoza, B., Zenit, R., Legendre, D. *The effect of confinement on the motion of a single clean bubble.* Journal of Fluid Mechanics, 2008. 616: p. 419-443.
166. Melville, W.K. *Wave modulation and breakdown.* Journal of Fluid Mechanics, 1983. 128: p. 489-506.
167. Lamb, H. *Hydrodynamics.* 1945. Dover, New York.
168. Shew, W.L., Poncet, S., Pinton, J.F. *Force measurements on rising bubbles.* Journal of Fluid Mechanics, 2006. 569: p. 51-60.
169. Zhang, J., Ni, M.J. *What happens to the vortex structures when the rising bubble transits from zigzag to spiral?* Journal of Fluid Mechanics, 2017. 828: p. 353-373.